Annu. Rev. Fluid Mech. 2000. 32:709–778

RECENT DEVELOPMENTS IN RAYLEIGH-BÉNARD CONVECTION

Eberhard Bodenschatz, Werner Pesch, and Guenter Ahlers

Laboratory of Atomic and Solid State Physics, Cornell University, Ithaca, New York 14853-2501; e-mail: eb22@cornell.edu

Physikalisches Institut der Universität Bayreuth, Bayreuth, Germany; 95440; e-mail: werner.pesch@uni-bayreuth.de

Department of Physics and Quantum Institute, University of California, Santa Barbara, California 93106; e-mail: guenter@stc.ucsb.edu

Key Words thermal convection, pattern formation, spatio-temporal chaos, spirals, spiral-defect chaos, domain chaos, hexagons

■ **Abstract** This review summarizes results for Rayleigh-Bénard convection that have been obtained over the past decade or so. It concentrates on convection in compressed gases and gas mixtures with Prandtl numbers near one and smaller. In addition to the classical problem of a horizontal stationary fluid layer heated from below, it also briefly covers convection in such a layer with rotation about a vertical axis, with inclination, and with modulation of the vertical acceleration.

1. INTRODUCTION

Fluid motion driven by thermal gradients (thermal convection) is a common and important phenomenon in nature. Convection is a major feature of the dynamics of the oceans, the atmosphere, and the interior of stars and planets (Busse 1978, 1989; Getling 1998). It is also important in numerous industrial processes. For many years the quest for the understanding of convective flows has motivated numerous experimental and theoretical studies.

In spatially extended systems, convection usually occurs when a sufficiently steep temperature gradient is applied across a fluid layer. The spatial variation of a convection structure often is referred to as pattern. The nature of such convection patterns is at the center of this review. Pattern formation is determined by nonlinear aspects of the system under study. For this reason the elucidation of pattern formation is a challenging problem in condensed-matter physics as well as in fluid mechanics. Pattern formation is also common in many other spatially extended nonlinear nonequilibrium systems in physics, chemistry, and biology (Manneville 1990, Cross & Hohenberg 1993). Patterns observed in diverse sys-

0066–4189/00/0115–0709$12.00

tems are often strikingly similar, and their understanding in terms of general, unifying concepts has long been a main direction of research (Cross & Hohenberg 1993, Newell et al 1993).

Many fundamental aspects of patterns and their instabilities have been studied intensively over the past three decades in the context of Rayleigh-Bénard convection (RBC). In a traditional RBC experiment, a horizontal fluid layer of height d is confined between two thermally well conducting, parallel plates. When the difference $\Delta T = T_b - T_t$ between the bottom-plate temperature T_b and the top-plate temperature T_t exceeds a critical value ΔT_c, the conductive motionless state is unstable and convection sets in. The simplest pattern which can occur is that of straight, parallel convection rolls with a horizontal wavelength $\lambda \approx 2d$ (wave number $q \approx \pi/d$). Such rolls can be found near onset; however, as the dimensionless distance $\varepsilon \equiv \Delta T/\Delta T_c - 1$ increases, the patterns often become progressively more complicated, and thus also more interesting.

Rayleigh-Bénard convection is perhaps the most thoroughly investigated and understood pattern-forming system. The experimental setup is simple in principle and the basic physical mechanism (buoyancy vs dissipation) well understood. For the standard description in terms of the Oberbeck-Boussinesq equations, Equations 1 and 2 below, only two nondimensionalized control parameters are sufficient (Busse 1978, 1989). The first is the Rayleigh number $R \equiv \alpha g \Delta T d^3/(\nu\kappa)$ with α the thermal expansion coefficient, κ the thermal diffusivity, ν the kinematic viscosity, and g the acceleration of gravity. Convection starts (under ideal conditions) at the critical value $R_c = 1708$. The second parameter is the Prandtl number $\sigma \equiv \nu/\kappa$, which can be viewed as the ratio of the vertical thermal diffusion time $t_\nu = d^2/\kappa$ to the vertical viscous relaxation time $t_\eta = d^2/\nu$. This parameter measures the relative importance of the nonlinear terms in the Boussinesq equations, namely those terms describing temperature and momentum advection.

There are several recent reviews of Rayleigh-Bénard convection.[1] In the present one we focus on new developments during the last decade or so. Let us, however, briefly outline some of the seminal earlier results that were of major importance for the later work. Quite early it was established theoretically that the stable pattern in an infinitely extended layer of a Boussinesq fluid close to onset (see Section 3 below) consists of straight, parallel rolls of wavenumber $q \approx q_c$ (Schlüter et al 1965). Further above onset, the stability regimes of these rolls in the $R - q$ space as functions of σ (the ''Busse balloon'') are well understood owing to the impressive work by Busse and coworkers (Busse 1978, 1989). The value of σ varies widely for different experimental fluids, from $\mathcal{O}(10^{-2})$ for liquid metals to values near one for gases and for liquid helium, to the range from 2 to 12 for water, and into the 1000s for silicone oil (see de Bruyn et al 1996 and references therein). Although R_c, the critical wavevector $q_c = 3.117$, and the patterns in the close vicinity of onset ($R \simeq R_c$) are independent of σ, subsequent

[1]Busse (1989), Croquette (1989a,b), Cross & Hohenberg (1993), de Bruyn et al (1996), and Getling (1991, 1998).

bifurcations that occur with increasing R are τ dependent. For example, one finds an oscillatory secondary instability at medium and small Prandtl numbers, in contrast to a stationary bimodal (knot) bifurcation at large σ (Busse 1978, 1989). Not too far from threshold, the Busse balloon was found to agree well with the experiments for large σ (water) (Busse & Whitehead 1971) and reasonably well for gases with $\sigma \simeq 1$ (Croquette 1989a, Plapp 1997).

Although ideal periodic patterns can be created in experiments, natural convective patterns, particularly when they form in the presence of lateral walls, typically are disordered and develop persistent spatio-temporal dynamics as ε increases. Snapshots of such patterns are characterized by local roll patches with grain boundaries and point defects (dislocations).[2] These spatio-temporal chaotic patterns are irregular in time and in the horizontal plane, but they maintain a relatively simple structure in the vertical direction. They should be contrasted with fully developed turbulence (Frisch 1995), at very large R, which is disordered in three spatial dimensions and not the topic of this review.

For the description of nonuniform patterns not too far from threshold, various reductions of the original hydrodynamical equations have proven to be useful (Manneville 1990, Cross & Hohenberg 1993, Newell et al 1993). One particularly important theoretical result, which motivated much of the work during the last decade, was that for a fluid of $\sigma \simeq 1$, roll curvature induces slowly varying long-range pressure gradients (Siggia & Zippelius 1981) that drive a so-called mean flow that in turn couples back to the roll curvature. In subsequent experimental work,[3] these ideas have found their convincing confirmation. Model equations that generalize the so-called Swift-Hohenberg equations (SH-equations) (Swift & Hohenberg 1977) were developed. They allow the isotropic description of the pattern-formation processes in the presence of mean flow (Manneville 1983, Greenside & Coughran 1984). Although the SH-equations can not be derived systematically from the Boussinesq equations, they capture much of the observed physical behavior and have now become a general tool used to investigate not only RBC, but also other pattern-forming systems (Cross & Hohenberg 1993).

2. RECENT DEVELOPMENTS

Over the last 10 years the major experimental progress in RBC was due to the development of experimental apparatus for the study of convection of compressed gases in samples with large aspect ratios $\Gamma = L/(2d)$. Here L is the typical lateral size of the convecting sample. Also very important was the rapid increase in computational power. The availability of large and fast storage media and of

[2]See Croquette (1989b), Manneville (1990), Newell et al (1993), Cross & Hohenberg (1994), and Busse & Clever (1998).

[3]See, for instance, Croquette et al (1986b), Croquette (1989a), Daviaud & Pocheau (1989), Hu et al (1995a), and Pocheau & Daviaud (1997).

digital imaging equipment was crucial. It is now possible to study pattern dynamics by acquiring large time sequences of images. Some recent experimental projects have involved the analysis of over 10^5 high-resolution digital images (Hu et al 1997).

At the end of the 1980s, a new era started with the work by Croquette and coworkers (Croquette 1989a,b), demonstrating that the horizontal planforms of thermal convection of compressed argon gas could be visualized by the now-well-established shadowgraph technique (de Bruyn et al 1996). Some very important mechanisms were identified and analyzed despite the use of rather small aspect-ratio cells ($\Gamma \simeq 15$). In the meantime, the aspect ratio of gas-convection cells has been pushed to much larger values ($\Gamma > 100$) (Bodenschatz et al 1992b, Morris et al 1993, Assenheimer & Steinberg 1993). Typical experimental cells are constructed with a reflective bottom plate (silver, aluminum, aluminum-coated sapphire, or silicon) and a transparent top sapphire plate. Whereas the bottom plate is usually heated with a film heater, the top plate is cooled by a circulating water bath (de Bruyn et al 1996). Two experimental designs have been used. In the first, the top plate of the convection cell acts as a pressure window. This limits the size of the diameter due to unavoidable mechanical deformations by the large pressure differential that the plate has to sustain (Croquette 1989a, Assenheimer & Steinberg 1993, Assenheimer 1994, Rogers et al 1998). In the second, the cooling water is pressurized, thus reducing the pressure differential to near zero. This allows the use of convection cells of larger diameter with little horizontal variations of R across the cell (de Bruyn et al 1996).[4]

Much of the theoretical work has been done in the Boussinesq approximation, which assumes that the fluid properties do not vary over the imposed temperature interval, except for the density, where it provides the buoyant force. Experiments can be conducted under conditions that correspond closely to the Boussinesq approximation. A quasi-Boussinesq fluid is typically achieved by designing an experiment that yields a modest critical temperature difference ΔT_c between the confining plates (typically not more than a few degrees C). This is achieved by using an appropriate cell height d. For conventional fluids like water, this implies that d must be larger than $\sim$ 3 mm. This in turn limits the maximum possible value of Γ because uniform cells of excessive lateral extent are difficult to construct and expensive to produce. Another factor that prohibits the use of large lateral dimensions is the increase with aspect ratio Γ of the horizontal diffusion time $t_h = \Gamma^2 t_v = \Gamma^2 d^2/\kappa$, which influences the time required for pattern relaxation. For example, for an experiment with water as a Boussinesq fluid, the typical vertical diffusion time $t_v \simeq 30$s. For $\Gamma \simeq 100$ this yields a horizontal diffusion time of $t_h \simeq 84h$. This would make experiments impractical, as some pattern-selection phenomena require timescales of tens of t_h (Ahlers et al 1985a).

Compressed gases have the advantage that the material parameters are such that a Boussinesq fluid can be achieved at rather small layer heights d. In typical

[4]Both ΔT and d need to be constant across the cell, as $R \propto \Delta T d^3$.

experiments the layer heights are in the range from 0.3 to 1 mm, and t_v can be one second or less. For a convection cell with $\Gamma = 100$, this gives a horizontal diffusion time of $t_h \simeq 3h$ (de Bruyn et al 1996). For pure gases away from the critical point, the value of the Prandtl number is $\sigma \approx 1$. However, it is possible to tune the Prandtl number in several ways. Assenheimer & Steinberg (1993, 1994, 1996a) conducted experiments near the critical point of SF_6. They were able to cover the Prandtl number range $2 < \sigma < 115$.[5] In their experiments the vertical thermal diffusion times ranged from $t_v = 3$s in a $d = 130$ μm cell to $t_v = 27$s in a $d = 380$ μm cell (Assenheimer 1994). In another experiment, Liu & Ahlers (1996, 1997) used gas mixtures to tune the Prandtl number from $0.17 < \sigma < 1$. For a cell of height $d = 1.46$ mm, their vertical thermal diffusion times were in the range $1.2\text{s} < t_v < 6\text{s}$. Thus in conclusion, compressed gases now allow experiments with large Γ for $0.17 < \sigma < 115$.

The substantial progress described above has allowed a whole set of new experiments and has led to many new discoveries. For horizontal RBC, Bodenschatz et al (1991, 1992a) investigated the competition between hexagons and rolls in non-Boussinesq convection (see Sect. 6.5). They also discovered giant rotating spirals, which were later analyzed in detail by Plapp & Bodenschatz (1996) and Plapp (1997) (see Sect. 6.3). In 1993, spiral-defect chaos (SDC) was discovered by Morris et al (1993) in a parameter regime where, on the basis of the theory for an infinitely extended system, parallel straight rolls (ideal straight rolls, or ISR) are stable (see Sect. 7). A great number of investigations followed that were concerned with the onset of SDC (see Liu & Ahlers 1996 and references therein). Later, in experiments by Cakmur et al (1997a), it was demonstrated that both SDC and ISR are, in fact, stable attractors in the same parameter regime. These developments were accompanied by increased theoretical activities. SDC was reproduced in SH-model calculations (see Cross 1996 and references therein) and in numerical solutions of the Boussinesq equations (see Pesch 1996 and references therein) (see Sect. 3). From these investigations it is clear that SDC is an attractor that competes with ISR and that mean-flow effects due to roll curvature are important at not too large σ. In another set of experiments, Assenheimer & Steinberg (1993) found that SDC evolved into a state of target chaos when the Prandtl number is raised (see Sect. 7). Assenheimer & Steinberg (1996b) also found a state of coexisting up-and-down hexagons, which was later explained theoretically by Clever & Busse (1996). During the last five years, experiments also studied the effect of rotation around a vertical axis (see Hu et al 1998 and references therein), of inclination (Daniels et al 1999), and of modulation of the vertical acceleration (Rogers et al 1998) (see Sect. 9). Another interesting topic, not discussed in this review, is thermal convection in planetary and stellar interiors, which is characterized by a finite angle between the vectors of rotation and gravity. This situation can be modeled in laboratory experiments through the use

[5]Work describing the experiments at $\sigma = 115$ was presented at the workshop Characterization of Spiral Detect Chaos at Los Alamos Nat. Lab., January 4–5 1999.

of centrifugal buoyancy (Busse et al 1998). Time-dependent complex states have been described and also new types of stationary patterns like the interesting hexa-rolls (Auer et al 1995).

The following sections discuss the above-mentioned developments in detail.

3. THEORETICAL ANALYSIS

In this section we sketch the common theoretical methods for the description of pattern-forming systems in order to emphasize the universal and common features among patterns in different systems. We exclusively consider large-aspect-ratio systems ($\Gamma \gg 1$), in which the horizontal dimensions of the fluid layer in the (x, y)-plane are assumed to be considerably larger than the cell height *d*. In typical experiments, shadowgraph visualization shows only the vertically averaged index-of-refraction variations.[6] This is analogous to theoretical treatments, where the interesting aspects of the patterns are reflected in suitable ''projections'' of the three-dimensional hydrodynamic description onto the two-dimensional horizontal plane. As discussed later in this section, such a dimensional reduction is reliable even for the complex spatial-temporal patterns presented in this review because the vertical spatial variations remain quite smooth.

Rayleigh-Bénard convection is described by the well-known nondimensionalized Boussinesq equations (see e.g. Busse 1978)

$$\sigma^{-1}\left(\frac{\partial \mathbf{u}}{\partial t} + \mathbf{u} \cdot \nabla \mathbf{u}\right) = -\nabla \pi + \nabla^2 \mathbf{u} + \hat{e}_z \Theta \qquad (1)$$

$$\frac{\partial \Theta}{\partial t} + \mathbf{u} \cdot \nabla \Theta = \nabla^2 \Theta + R\hat{\mathbf{e}}_z \cdot \mathbf{u}, \qquad (2)$$

where $\hat{\mathbf{e}}_z$ is the unit vector in the *z* direction (opposite to the direction of gravity) and π is the pressure. The velocity field $\mathbf{u}$ and the deviation Θ of the temperature from the diffusive linear temperature profile vanish at the horizontal boundaries of the cell.[7] Incompressibility ($\nabla.\mathbf{u} = 0$) is assumed. As already discussed in Section 1, the system is governed by two dimensionless quantities, namely the Rayleigh number *R* and the Prandtl number σ. Equations 1 and 2 show the sensitivity to σ. For $\sigma \gg 1$, the left-hand side of Equation 1 can be neglected, thereby eliminating one of the nonlinearities. For $\sigma \approx 1$, both nonlinearities in Equations 1 and 2 are important.

[6]To be precise, the shadowgraph signal is sensitive to the second derivative of the index of refraction with respect to the horizontal coordinates (de Bruyn et al 1996, Berry & Bodenschatz 1999).

[7]Alternatively, in the theoretical models free-slip boundaries have been used. At small σ one then finds patterns of spatio-temporal chaos immediately above onset (Busse et al 1992, Xi & Gunton 1995).

Equations 1 and 2 must be generalized for more complicated experimental situations, in which some of the underlying symmetries are broken. For instance, in the case of rotation about a vertical axis the Coriolis force $2\Omega\hat{\mathbf{e}}_z \times \mathbf{u}$ must be included in Equation 1 (see e.g. Küppers & Lortz 1969). In principle, the centrifugal force should also be included; however, in experiments the rotation rate Ω is typically kept so small that the centrifugal force is insignificant (see also Sect. 8). Convection becomes anisotropic when the layer is inclined, i.e., when the normal to the layer has a finite angle with gravity. In this case a shear flow already exists in the base state (see also Sect. 9.2).

In the most commonly used Boussinesq description, the material parameters within the layer are approximated by their vertical average (except for the density, which is responsible for the buoyancy force driving the convection). For experiments with large temperature gradients, vertical variations of the material parameters are significant and have to be included in the theoretical description (see e.g. Busse 1967). This leads to a transcritical bifurcation at threshold and to hexagonal patterns instead of rolls (see also Sect. 6.5). This situation is generally referred to as non-Boussinesq convection. In yet another variation, the influence of temporal (see Sect. 9.3) and spatial modulations (Schmitz & Zimmermann 1996) on RBC was considered.

3.1 Ideal Straight Rolls and Their Stability

The theoretical methods for analyzing pattern-forming instabilities are quite extensively discussed in the literature (see e.g. Cross & Hohenberg 1993, Newell et al 1993, and Pesch & Kramer 1995). One expects, in good agreement with certain carefully controlled experiments, that for large-aspect-ratio systems the simplifying idealization of an infinitely extended system is justified. This naturally leads to a convenient description of patterns in terms of Fourier modes in a two-dimensional (2d) wavevector ($\mathbf{q}$) space. For an ideal straight-roll (ISR) pattern with wavelength, only one pair of Fourier modes is excited; ideal square patterns require two pairs of modes, and ideal hexagons, three.[8] These ideal patterns can be approximated experimentally in necessarily finite containers only under certain exceptional, well-controlled conditions. For certain initial conditions, or when the influence of lateral boundaries is strong, experiments often produce disordered patterns that require a wave packet of many modes in their theoretical description.

The first step in the theoretical analysis is the standard linear stability analysis of the basic (primary) state. The problem diagonalizes in Fourier space with respect to the horizontal coordinates $\mathbf{x} = (x, y)$ according to the ansatz $\mathbf{V}(\mathbf{x}, z, t) = e^{i\mathbf{q}\cdot\mathbf{x}}\mathbf{U}(\mathbf{q}, z)e^{\lambda(\mathbf{q})t}$. The symbolic vector $\mathbf{V}$ stands for the field variables Θ, $\mathbf{u}$ in Equations 1 and 2. For fixed $\mathbf{q}$ one arrives at an eigenvalue problem with a discrete set of eigenvalues $\lambda_i(\mathbf{q}, R)$ with the corresponding eigenvectors $\mathbf{U}_i(\mathbf{q}, z)$, where the λ_i, $i = 1,2 \ldots$ are ordered with respect to decreasing magnitudes of the real

[8]This is only true to linear order—in general higher harmonics are also excited.

part. When, for increasing R, the growth rate, i.e. $\mathcal{R}e(\lambda_1(\mathbf{q}, R))$ crosses zero at $R = R_0(\mathbf{q})$ (neutral curve) and becomes positive, the instability occurs. Minimization of $R_0(\mathbf{q})$ yields the critical wavevector $\mathbf{q}_c$ and the threshold $R_c = R_0(\mathbf{q}_c)$. ISR solutions of wavevector $\mathbf{q}$ exist for $R > R_0(\mathbf{q}) \geq R_c$. The bifurcation to ISR will be either stationary, i.e. when $\mathcal{I}m(\lambda_1(\mathbf{q}_c, R_c)) = 0$, or oscillatory (Hopf), i.e. when $\mathcal{I}m(\lambda_1(\mathbf{q}_c, R_c)) \neq 0$ as for instance at low σ in RBC with rotation (see Sect. 9.1). The $\mathbf{q}$-dependence of λ_i [and correspondingly of $R_0(\mathbf{q})$] reflects the spatial symmetries of the system. In rotationally invariant systems like RBC, the eigenvalues λ_i can depend only on $|\mathbf{q}|$, whereas, for example, in axially anisotropic systems like the inclined layer (or nematic liquid crystals), the angle $\phi_\mathbf{q}$ of $\mathbf{q}$ with respect to the direction of anisotropy is also important: One observes, besides normal rolls ($\phi_\mathbf{q} = 0$), situations with broken chiral symmetry ($\phi_\mathbf{q} \neq 0$).

For our purpose, a reformulation of the nonlinear partial differential equations, Equations 1 and 2, is very convenient (Pesch 1996). The solutions $(\mathbf{u}, \Theta) \equiv \mathbf{V}$ are expanded in terms of the eigenvectors $U_i(\mathbf{q}, z)$ of the linear problem as

$$\mathbf{V}(\mathbf{x}, z, t) = \sum_{i,q} A_i(\mathbf{q}, t) U_i(\mathbf{q}, z) \exp(i\mathbf{q}\mathbf{x}). \tag{3}$$

Projection on the U_i leads to a coupled system of ODEs for the expansion coefficients A_i:

$$\partial_t A_i(\mathbf{q}, t) = \lambda_i(\mathbf{q}) A_i(\mathbf{q}, t) + N_i(A_j, A_k). \tag{4}$$

Note that the different $\mathbf{q}$-vectors are coupled by the projections N_i of the quadratic nonlinearities in Equations 1 and 2. In practice, the equations are then suitably truncated ($i \leq N_{cut}$) and solved on a discrete mesh of wavevectors $\mathbf{q}$. In addition, it is convenient to capture the z-dependence of the U_i by an expansion in suitable basis functions that fulfill the vertical boundary conditions (''Galerkin method,'' Clever & Busse 1974).

The evaluation of periodic nonlinear stationary solutions $\mathbf{V}_{stat}$ of Equation 4 amounts to the solution of a nonlinear set of algebraic equations; $\mathbf{V}_{stat}$ contains a basic mode with wavevector $\mathbf{q}_0$ together with its higher harmonics. As before, the stability of the stationary solutions is determined by an eigenvalue problem, which arises from the linearization of Equation 4 around $\mathbf{V}_{stat}$. In general, one has to consider long-wavelength (modulational) and short-wavelength instabilities. Perturbations with wavevectors $\mathbf{q} = n\mathbf{q}_0 + \mathbf{s}$, where $n = (0, \pm 1, \pm 2 \ldots)$, are considered, and the stability is determined by searching the growth rates λ_{nonlin} $(\mathbf{q}, \mathbf{s}, R)$ for the largest real part. The corresponding eigenvector is dominated by a mode with wavevector $n_{max}\mathbf{q}$. In most cases there exists a region in $(R, \mathbf{q}, \lambda)$ − space for which the periodic solutions are stable, i.e. where $\lambda_{nonlin} < 0$.

The boundaries of the stability region (Busse balloon) are determined by various destabilization mechanisms (Busse 1989). Of particular importance are the destabilizing long-wavelength modulations ($|\mathbf{s}| \ll |\mathbf{q}|$, $\mathcal{I}m(\lambda) = 0$) of the ISR-pattern. One speaks of Eckhaus (ECK) ($n_{max} = 1$ and $\mathbf{s} \parallel \mathbf{q}$, modulation of the roll distance), zig-zag (ZZ) ($n_{max} = 1$ and $\mathbf{s} \perp \mathbf{q}$, undulations along the roll axis),

or in the general case of skewed varicose (SV) instabilities ($n_{max} = 1$). For $\sigma \approx 1$, SV-instabilities delineate the boundary of the Busse balloon on the large-q side. For $\sigma \lesssim 1$, yet another instability, the ''oscillatory instability,'' limits the Busse balloon from above. This instability has $\mathcal{I}m(\lambda) \neq 0$, $\mathbf{s} \perp \mathbf{q}$, and $n_{max} = 1$. In addition, short-wavelength mechanisms can come into play. In this case the pattern is destabilized by disturbances with wavevectors $|\mathbf{s}| \approx |\mathbf{q}|$ but at a finite angle with respect to $\mathbf{q}$. For $\sigma \approx 1$, the cross-roll (CR) instability with $\mathbf{s} \perp \mathbf{q}$ ($n_{max} = 0$, $\mathcal{I}m(\lambda) = 0$) limits the Busse balloon at small wavenumbers. These instabilities are discussed in more detail for $\sigma \approx 1$ in Section 5. Experiment shows (see Egolf et al 1998 and references therein), that to a good approximation, the idealized Busse balloon is also applicable locally to patches of ISR in an otherwise disordered pattern.

The Küppers-Lortz instability (Küppers & Lortz 1969) occurs in RBC cells rotated around a vertical axis. Above a certain rotation frequency $\Omega_c(\sigma)$, periodic roll patterns are unstable, even at threshold. At large σ, one finds, for instance, $\angle(\mathbf{q}, \mathbf{s}) \approx 60^\circ$ with $|\mathbf{s}| \approx q_c$ ($n_{\max} = 0$).

3.2 Order Parameter Equations

Slightly above threshold and when $\mathbf{q}$ is near $\mathbf{q}_c$, the amplitude A_1 ($\equiv A$) can be treated as the main dynamical variable, because only $\mathcal{R}e(\lambda_1(\mathbf{q}))$ is positive. By a systematic expansion up to cubic order in A, which is assumed to be small near onset, one arrives at an order parameter equation (OPE) in Fourier space:

$$\frac{\partial}{\partial t} A(\mathbf{q}, t) = \lambda_1(\mathbf{q})A(\mathbf{q}, t) + \int d\mathbf{q}_1\, a_2(\mathbf{q}, \mathbf{q}_1)A(\mathbf{q}_1, t)A(\mathbf{q} - \mathbf{q}_1, t) + \int d\mathbf{q}_1 d\mathbf{q}_2\, a_3(\mathbf{q}, \mathbf{q}_1, \mathbf{q}_2)A(\mathbf{q}_1, t)A(\mathbf{q}_2, t)A(\mathbf{q} - \mathbf{q}_1 - \mathbf{q}_2, t). \quad (5)$$

The reduced dynamical description of patterns in terms of one amplitude $A(\mathbf{q})$ (weakly nonlinear analysis) serves as the unifying description of many different pattern-forming phenomena. Systems differ mostly with respect to the explicit expressions for λ and the kernels a_2, a_3. The order-parameter formulation, Equation 5, is nowadays standard (Haken 1978, Cross & Hohenberg 1993, Newell et al 1993). In particular, it has been shown that the OPE (5) can capture the Busse balloon even far away from threshold. Thus the OPE is particularly useful in describing systems for which a fully nonlinear analysis is too demanding (Pesch & Kramer 1995).

In RBC under Boussinesq conditions, where only the temperature variations of the density across the cell are kept, the a_2 term in Equation 5 is zero. In this case, one obtains a supercritical (forward) bifurcation; i.e. above threshold, the amplitude $A(\mathbf{q}_c)$ grows continuously $\sim \sqrt{(R - R_c)}/R_c$ (Schlüter et al 1965). Temperature variations of the material parameters, such as the viscosity or the thermal diffusivity, are typically small and can be treated perturbatively in terms of a small parameter $\mathcal{P}$ (Busse 1967) (see also Cross & Hohenberg 1993, Sect.

VIII.F,3). For $\mathcal{P} \neq 0$, the quadratic term ($a_2 \propto \mathcal{P}$) in Equation 5 is nonvanishing and the symmetry $A \rightarrow -A$ is broken. This reflects the broken inversion symmetry $z \rightarrow -z$, $\Theta \rightarrow -\Theta$, $u_z \rightarrow -u_z$ due to additional terms in Equations 1 and 2. The onset of convection becomes transcritical toward a hexagonal pattern, which can exist even below R_c because the quadratic term is activated due to a resonant coupling $\mathbf{q}_1 + \mathbf{q}_2 + \mathbf{q}_3 = 0$ of the corresponding wavevectors (see Sect. 6.5).

Also important is that Equation 5 can be taken as the general basis for a ''derivation'' of the reduced model equations for pattern-forming systems. Let us briefly sketch the derivation of the Swift-Hohenberg (SH) equations for $a_2 = 0$ (Swift & Hohenberg 1977). They can be obtained by transforming Equation 5 to the 2d-position space for the amplitude $\psi(x) = \int d\mathbf{q}\ exp(i\mathbf{qx})A(\mathbf{q})$. If the arguments of the kernel $a_3(\mathbf{q}, \mathbf{q}_1, \mathbf{q}_2)$ are suitably fixed at $|\mathbf{q}_c|$, the cubic nonlinearity in Equation 5 becomes proportional to ψ^3. Keeping additional terms from an expansion about $\mathbf{q}_c$ leads to further cubic terms with gradients of ψ. However, the expansion of the kernel is not smooth, and certain nonanalytic contributions (the so-called mean-flow terms) have to be treated separately in terms of a further amplitude B (Manneville 1983, Cross & Hohenberg 1993, Decker & Pesch 1994). One arrives at

$$\begin{aligned} \partial_t \psi &= \left(\varepsilon - \frac{\xi^2}{4q_c^2}(\Delta + q_c^2)^2 - \psi^2\right)\psi - \frac{1}{q_c}\mathbf{U}\nabla\psi, \\ \mathbf{U} &= (\partial_y B, -\partial_x B), \\ \left(c_1 - \frac{c_2}{q_c^2}\nabla^2\right)\nabla^2 B &= \frac{\sigma^{-1}}{q_c^2}(\nabla(\nabla^2\Psi) \times \nabla\Psi) \cdot \hat{e}_z. \end{aligned} \tag{6}$$

In Equation 6, $\varepsilon = (R - R_c)/R_c$ serves as the convenient measure of the distance from threshold. The coherence-length amplitude ξ and c_1, c_2 are constants. In some cases it is useful to further reduce the SH-equations by eliminating the fast spatial variations $\propto q_c^{-1}$. One arrives at so-called Ginzburg-Landau equations, such as the well-known Newell-Whitehead-Segel equation (Newell & Whitehead 1969, Segel 1969), which describe modulated patterns about a wavevector of a fixed direction. In the case $B = 0$ (appropriate at large Prandtl-number), the dynamics of Equation 6 are governed by a Lyapunov functional $\mathcal{F}$ according to $\partial\psi/\partial t = -\delta\mathcal{F}/\delta\psi$, and the time evolution is toward a fixed point. However, for finite B the system is not potential, thus opening the possibility for complex spatio-temporal behavior. Consequently, a description of patterns based on Equations 6 or their slight generalizations has become popular in analytical investigations as well as in many numerical studies (see Cross & Hohenberg 1993). Based on Equations 6, researchers have successfully investigated the dynamics of defects and grain boundaries (see Cross & Hohenberg 1993), the stability of planforms and transitions between them [e.g. from hexagons to rolls (Xi et al 1992)], and the influence of noise (see Sect. 4). In particular, important insight into the mechanism of spiral-defect chaos (SDC) (Xi et al 1993, Bestehorn et al

1992) and the Küppers-Lortz instability (Tu & Cross 1992a) has been achieved on the basis of the SH-formulation. One should note, however, that due to missing higher-order derivative terms, the Busse balloon is in general not described systematically (Decker et al 1994).

3.3 Phase-Diffusion Equations

Even far above onset, the structure of periodic patterns far away from defects and grain boundaries can be captured by nonlinear phase-diffusion equations. These equations describe slow variations of the orientation and spacing of the convection rolls (see Newell et al 1993 and references therein). Let a family of stationary, periodic, and reflection-symmetric solutions be denoted by $\mathbf{V}(\underset{\sim}{\mathbf{q}}, \mathbf{x}) = u_{\mathbf{q}}(\mathbf{q} \cdot \mathbf{x})$ with $u_{\mathbf{q}}(\phi + 2\pi) = u_{\mathbf{q}}(\phi)$, and let us write the actual state as $\mathbf{V}(\mathbf{x}, \mathbf{t}) = \mathbf{u}_{\mathbf{q}}[\phi(\mathbf{x}, \mathbf{t})] +$ corrections. Thus $\phi(\mathbf{x}, t)$ is the phase of a nearly periodic pattern, and $\nabla \phi(\mathbf{x}, t) = \mathbf{q}(\mathbf{x}, t)$ plays the role of the local wavevector,[9] which we assume to vary slowly in space and time. In a seminal paper, Pomeau & Manneville (1979) showed that the phase dynamics can be described by a diffusion equation. They also found that at the long-wavelength instability boundaries of the Busse balloon, certain diffusion constants changed sign.

Subsequently, a rotationally invariant form of the phase equation, which also included the mean flow $\mathbf{U}$, the Cross-Newell equation, was derived (see Newell et al 1993 and references therein). In its simplest form, the equation reads

$$\tau(q) \frac{\partial}{\partial t} \varphi + \mathbf{U}\mathbf{q} = \nabla \cdot (B(q)\mathbf{q}) \tag{7}$$

$$\mathrm{curl}_z \mathbf{U} = -\gamma\sigma^{-1}\mathbf{e}_z \cdot \nabla \times [\mathbf{q}\nabla \cdot (\mathbf{q}A^2)]. \tag{8}$$

Phase equations are very valuable in the analysis of nonideal periodic patterns. This applies, for instance, to the dynamics of dislocations in an ISR pattern. Here dislocations climb with a velocity $v = \alpha(q - q_d(\varepsilon))$ where α is almost constant and q is the wavenumber of the pattern (Tesauro & Cross 1986). Consequently, a dislocation is stationary for a roll pattern with background wavenumber $q = q_d(\varepsilon)$. Also using this approach, Newell et al (1991) determined a wavenumber $q_f(\varepsilon)$, $q_f(0) = q_c$, which is selected by concentric patterns. Those authors demonstrated as well that at small σ, concentric patterns become unstable at a certain quite-small value of ε due to the coupling to the mean flow. It has been suggested by Cross & Tu (1995) and confirmed by Plapp et al (1998) that the competition of the two selected wavenumbers q_f and q_d determines the dynamics of the giant spirals, as discussed in Section 6.3.

The possible defect structures in natural convection patterns, such as dislocations or grain boundaries, correspond to singularities in a two-dimensional (wave)

[9]In a real field the wavevector (q_x, q_y) is equivalent to $-q_x, -q_y$; i.e. $\mathbf{q}(\mathbf{x})$ is actually a director field.

vector field and are well classified in differential geometry. Recently this insight has considerably improved the understanding of the solution manifold of the phase-diffusion equations (Newell et al 1996, Bowman et al 1998, Ercolani et al 1999). Although the underlying basic hydrodynamic description of convection patterns is nonpotential, the phase equations often derive from a Lyapunov functional (Newell et al 1996). Whether such a potential could provide some general selection principle according to which natural patterns approach stationary configurations remains an open question.

3.4 Numerical Simulations

The (large) system of ODEs in Equation 4 has become very useful for the generation of numerical solutions of the Boussinesq equations (Decker et al 1994, Pesch 1996). In contrast to the standard discretization schemes, the use of Equation 4 permits a description of the dynamics in terms of the most important active modes [$\mathcal{R}e(\lambda)$ not too small]. Passive modes can be adiabatically eliminated. In the numerical implementation, the most time-consuming manipulations can be based on the fast Fourier transformations (FFT). The speed of this pseudospectral method permits the simulation of the large-aspect-ratio systems used in experiments. In the time-stepping scheme, the linear operator is treated fully implicitly, whereas an explicit Adams-Bashforth scheme is used for the nonlinear part. A time step as large as $0.02t_v$ yields stable performance. One must keep in mind that diffusive changes of the patterns take place on much longer timescales ($\Gamma^2 t_v$). However, simultaneously one must resolve processes on timescales of order t_v, such as the nucleation or annihilation of defects or the fast core rotation of spirals. The code can also be used to approximate nonperiodic boundaries by the use of suitable spatial ramps in the Rayleigh number. An example is given in Figure 1. The simulation was started from random initial conditions and shows the pattern after transients had died out. Apparently it is not difficult to reproduce the common experimental situation where the rolls meet the boundaries perpendicularly.[10] We note that the dislocations and grain boundaries in the outer part of the annulus are required to keep the local wavenumber inside the Busse balloon.[11]

Further examples of simulations are shown in the sections below (see also Pesch 1996). Another advantage of the direct simulations is the ability to use an experimental shadowgraph picture as an initial condition and then reconstruct the entire 3-D convective structure corresponding to the experiment (see Section 7).

[10]This is not to imply, however, that this simple spatial variation of the control parameter is in any sense equivalent to the physical lateral boundary conditions relevant to real experiments.

[11]This work was presented at the workshop *Spatiotemporal Characterization of Spiral Defect Chaos* at Los Alamos National Laboratory, January 4–5, 1999. Sensoy & Greenside (1999) investigated similar structures within the SH-equations.

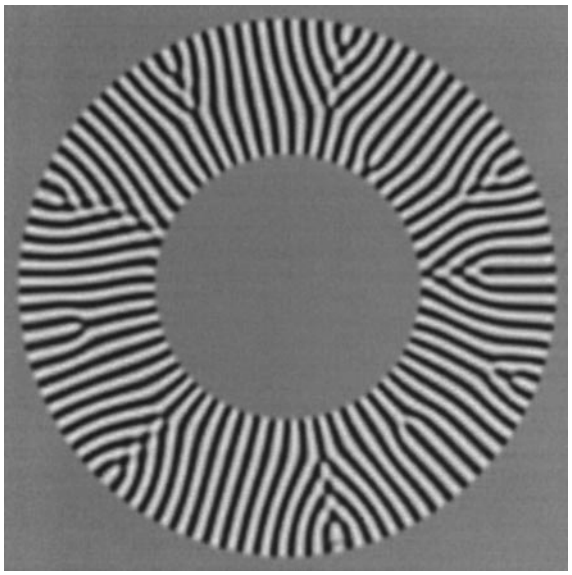

Figure 1 Radial roll structure for an annulus for $\sigma = 1.0$ at $\varepsilon = 0.4$. (IV Melnikov and W Pesch, unpublished).

4. FLUCTUATIONS

As described in Section 3, the study of convection patterns is usually based on a stability analysis of the deterministic hydrodynamic equations. Such a theory gives a sharp threshold at $R = R_c$, with $\mathbf{u}$ and Θ equal to zero below it (see Equations 1 and 2). For $R > R_c$, or equivalently $\varepsilon > 0$, convection rolls with wavenumber q_c are predicted to initially grow exponentially in time and thereby to destabilize the motionless state. One has to keep in mind, however, that the ''thermal noise'' of the microscopic degrees of freedom has been averaged away in this treatment. This noise drives fluctuations of the macroscopic velocity and temperature fields about their mean values even below the bifurcation. For a constant noise intensity and in the absence of nonlinear saturation, the amplitudes of these fluctuations diverge as the bifurcation point is approached. For this reason, the deterministic approach breaks down in the close vicinity of onset ($\varepsilon \approx 0$). This is analogous to second-order phase transitions in equilibrium thermodynamics, where fluctuations become large close to the critical temperature.

This problem received considerable theoretical attention about three decades ago (for a review, see Cross & Hohenberg 1993). The analysis was based on the stochastic Navier-Stokes equation given by Landau & Lifshitz (1959) and on stochastic Ginzburg-Landau and Swift-Hohenberg equations. Time-dependent fluctuating convective flows with zero mean but finite mean-square amplitudes $\langle A^2 \rangle$ were predicted for $\varepsilon < 0$. At $\varepsilon = 0$, $\langle A^2 \rangle$ diverges in proportion to $(-\varepsilon)^{-1/2}$ until nonlinear saturation sets in. However, estimates of the noise strength suggest that the fluctuations should remain unobservably small at exper-

imentally accessible values of ε because the thermal energy k_BT (k_B is the Bolzmann constant) that drives them is many orders of magnitude smaller than the typical kinetic energy of a macroscopic convecting fluid element (see Swift et al 1991, Hohenberg & Swift 1992). Nonetheless, it has now become possible to observe the fluctuating convection patterns below the bifurcation directly and to make quantitative measurements of their root-mean-square (rms) amplitudes.

The first system for which this became possible was electroconvection in a nematic liquid crystal (Rehberg et al 1991). Even though that system is ''macroscopic,'' it is particularly susceptible to noise because the physical dimensions are only of order 10 μm and because the orientational elastic constants (which determine the macroscopic energy to which k_BT has to be compared) are exceptionally small. More recently, fluctuations were observed also for RBC by Bodenschatz et al (1992a), and quantitative measurements of their amplitudes were made by Wu et al (1995).[12] These measurements were made possible by maximizing the sensitivity of the shadowgraph method (de Bruyn et al 1996) and by careful digital image analysis. The left part of Figure 2 shows a processed image of a layer of CO_2 of thickness 0.47 mm at a pressure of 29 bar and at a mean temperature of 32.0°C. The sample was at $\varepsilon = -3 \times 10^{-4}$, very close to but just below the bifurcation point. The fluctuating pattern is barely detectable by eye. The right half of the figure shows the average of the structure factors (squares

[12]Measurements on binary-mixture convection by Schöpf & Rehberg (1994) and by Quentin & Rehberg (1995) involved pseudo-one-dimensional sample geometries for which theoretical predictions are more difficult to obtain due to the influence of the sidewalls.

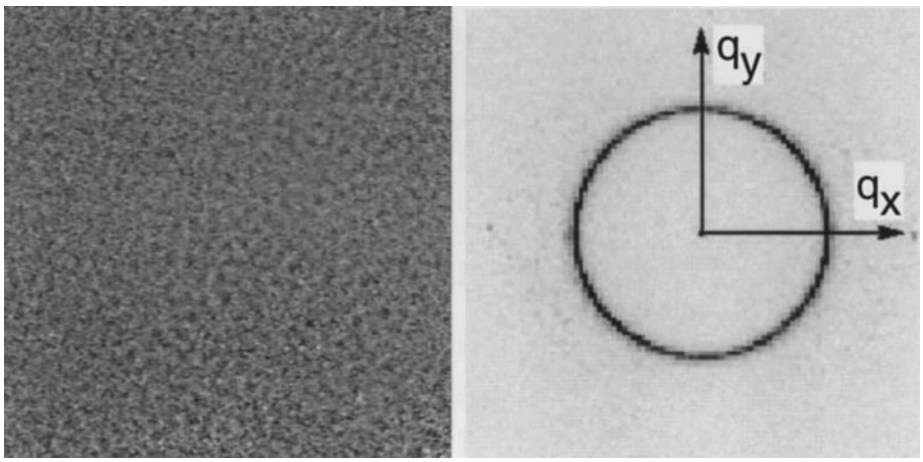

Figure 2 (*Left*) Shadowgraph snapshot of fluctuations below the onset of convection ($\varepsilon = -3 \times 10^{-4}$). (*Right*) The average of the square of the modulus of the Fourier transform of 64 images like that on the left. After Wu et al (1995).

of the moduli of the Fourier transforms) of 64 such images, clearly demonstrating that the fluctuations have a characteristic wavenumber q that was found to be in quantative agreement with the critical wavenumber $q_c = 3.117$ for RBC. The ring in Fourier space is azimuthally uniform, reflecting the continuous rotational symmetry of the RBC system.

The power contained within the ring in Fourier space can be converted quantitatively to the mean-square amplitude of the temperature field (Wu et al 1995, de Bruyn et al 1996). Results for the temporal and spatial average $\delta T^2(\varepsilon)$ of the square of the deviations of the temperature from its local time average (pure conduction) as a function of ε at two different sample pressures are shown in Figure 3. The data can be described quite accurately by the powerlaw $\delta T^2 \propto \varepsilon^{-1/2}$, as predicted by theory.

The amplitudes of the fluctuating modes below but close to the onset of RBC were calculated quantitatively from the stochastic hydrodynamic equations (Landau & Lifshitz 1959) by van Beijeren & Cohen (1988), using realistic (no-slip) boundary conditions at the top and bottom of the cell. For the mean-square temperature fluctuations, their results give (Hohenberg & Swift 1992, Wu et al 1995)

$$\delta T^2(\varepsilon) = \tilde{c}^2 \left(\frac{\Delta T_c}{R_c}\right)^2 \frac{F}{4\sqrt{-\varepsilon}}, \tag{9}$$

with $\tilde{c} = 3q_c\sqrt{R_c} = 385.28$, and

$$F = \frac{k_B T}{\rho d \nu^2} \times \frac{2\sigma q_c}{\xi_o \tau_o R_c}, \tag{10}$$

with $\xi_0 = 0.385$ and $\tau_0 = 0.0796$. Using the fluid properties of the experimental samples, one obtains the straight lines in Figure 3. The agreement between theory and experiment is very good. This agreement lends strong support to the validity of Landau's stochastic hydrodynamic equations (Landau & Lifshitz 1959).

Sufficiently close to the bifurcation, the fluctuations should induce deviations from the usual mean-field behavior implied by Equation 9 (Hohenberg & Swift

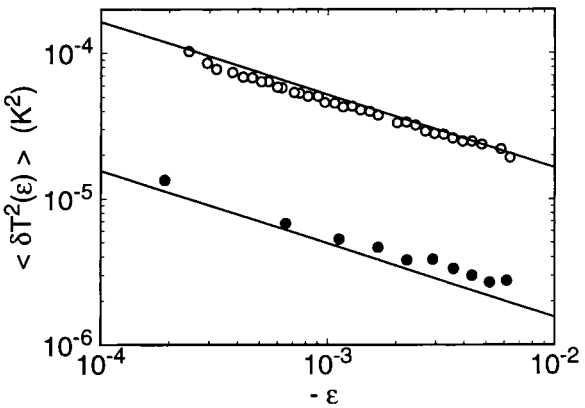

Figure 3 Mean-square amplitudes of the temperature fluctuations below the onset of convection of a layer of CO_2 of thickness 0.47 mm and a mean temperature of 32°C. The solid (open) circles are for a sample pressure of 42.3(29.0) bar. The two lines are the theoretical predictions. Note that there are no adjustable parameters. After Wu et al (1995).

1992). In the case of Rayleigh-Bénard convection, this deviation is predicted to take the form of a hysteretic bifurcation (Hohenberg & Swift 1992, Brazovskii 1975). However, this should become observable only in the range $|\varepsilon| \lesssim 10^{-5}$ or so, which is not expected to become experimentally accessible in the near future.

5. IDEAL STRAIGHT ROLLS

Above but close to onset, the predictions of the linear and weakly nonlinear theory (Schlüter et al 1965) were reproduced quantitatively in a number of experiments (see Cross & Hohenberg 1993 and references therein). A particularly detailed study was carried out by Hu et al (1993). For cases where the fluid properties are known sufficiently well, measurements yielded values of R_c within a few percent of the theoretical value, $R_c = 1708$ (de Bruyn et al 1996). Experiments with quasi-Boussinesq fluids (see Sect. 3) yielded a supercritical bifurcation at R_c. Above onset, almost-defect-free roll patterns with wavenumbers close to the theoretical value $q_c = 3.117$ were found. Examples are shown in Figures 4a and b for a circular and a square cell, respectively. Beyond R_c the amplitude of the shadowgraph signal (Figure 8 of Hu et al 1993), proportional to the amplitude of the temperature field Θ, grows as $\sqrt{\varepsilon}$ as is evident, for instance, from the open circles in Figure 12 below in Section 6.2. The convective heat transport, usually expressed as the Nusselt number N (the ratio of the effective conductivity of the fluid to the conductivity in the absence of convection), can be written as $N = S_1\varepsilon$ for small positive ε and shows no hysteresis at the bifurcation (Figure 4 of Hu et al 1993). However, S_1 usually is somewhat smaller than the prediction (Schlüter et al 1965) for the laterally infinite system. The reason for this may be

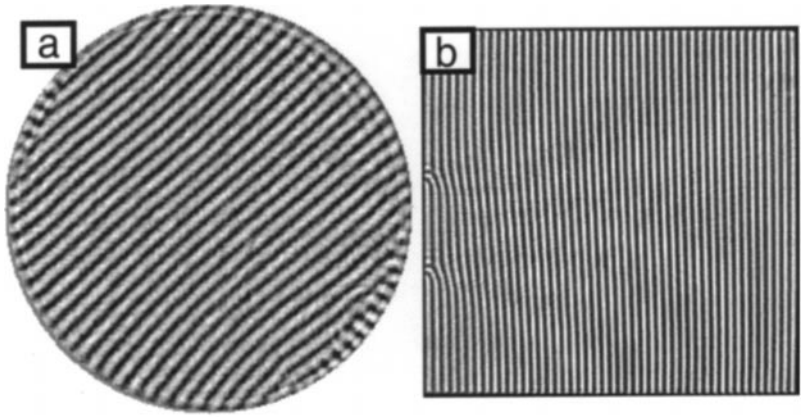

Figure 4 Straight parallel rolls for circular and square sidewalls. (a) From Liu & Ahlers (1996) at $\varepsilon = 0.07$ with $\Gamma = 30$ and $\sigma = 0.69$. (b) After Cakmur et al (1997a) at $\varepsilon = 0.3$ with $\Gamma = 50$ and $\sigma = 1.03$.

that the flow near the walls, as well as near any defects that may be present, is suppressed.

At values of ε larger than about 0.1 the rolls in circular cells develop strong curvature and defects appear in the patterns. These interesting boundary-induced phenomena are discussed in Section 6.1. Due to their geometry, rectangular cells are better suited for the study of parallel straight rolls over a wide ε-range. Patterns can be created that come close to the theoretical idealization of ISR, and they persist even at large ε. In the remainder of this section, we review investigations of the Busse balloon and its limiting instabilities for ISR in cells with square geometry.

For $\sigma \simeq 1$, Figures 5a, c, and e demonstrate that stable ISR patterns can be observed experimentally over a wide range of ε (Cakmur et al 1997a, Plapp 1997). Even above the OSC-instability boundary (Figure 5e) the pattern was ISR-like. However, ISR formed only when a perfect parallel-roll pattern was initially prepared by special procedures (described below). The generic attractor starting from random initial conditions is a spatio-temporal chaotic state called spiral-defect chaos (SDC) (Morris et al 1993), which is discussed in detail in Section 7. In Figure 5, images of SDC are compared with ISR at the same ε-values.

Ideal straight rolls were initialized in a square cell of $\Gamma = 50$ by a special protocol.[13] It involved inclining the cell to induce a large-scale flow that aligned the rolls (Cakmur et al 1997a, Plapp 1997, Jeanjean 1997). After appropriate equilibration procedures, the rolls could then be used to explore the Busse balloon. The stability boundaries were determined by suitable quasistatic changes of ε as indicated by the arrows in Figure 6. When the SV-boundary at the high wavenumber was crossed (circles), the SV-instability occurred and nucleated one or two defect pairs by the well-known ''roll pinching'' (Croquette 1989a). As shown in Figure 7, the defects traveled along the roll axis to the boundaries, destroying one or two roll pairs and thus changing the wavenumber back into the stable regime (triangles). This way, Cakmur et al (1997a) were able to follow the SV instability-boundary until they crossed the oscillatory instability-boundary (OSC). As shown in Figure 6, good agreement between the theoretical predictions for the laterally infinite system and the experiment was found.

Above the oscillatory instability line (OSC), a triangular traveling-wave pattern is superimposed onto the rolls (Busse 1972, Croquette & Williams 1989a,b). This can be seen already in Figure 5e, and an example is shown for left-traveling waves in Figure 8A. Fourier-demodulation techniques are well suited for a detailed investigation of such patterns (Rasenat et al 1990, de Bruyn et al 1996). Whereas Figure 8B shows the power spectrum, Figures 8C and 8D show the real part of the Fourier back-transform of the areas encircled by the black and gray lines, respectively. The spatial disorder of the traveling waves is most evident in the demodulated pattern shown in Figure 8D. The oscillatory instability is con-

[13]Only large wavenumbers close to the skewed-varicose stability-boundary were stable; otherwise, cross-roll disturbances grew at the boundaries, leading to SDC.

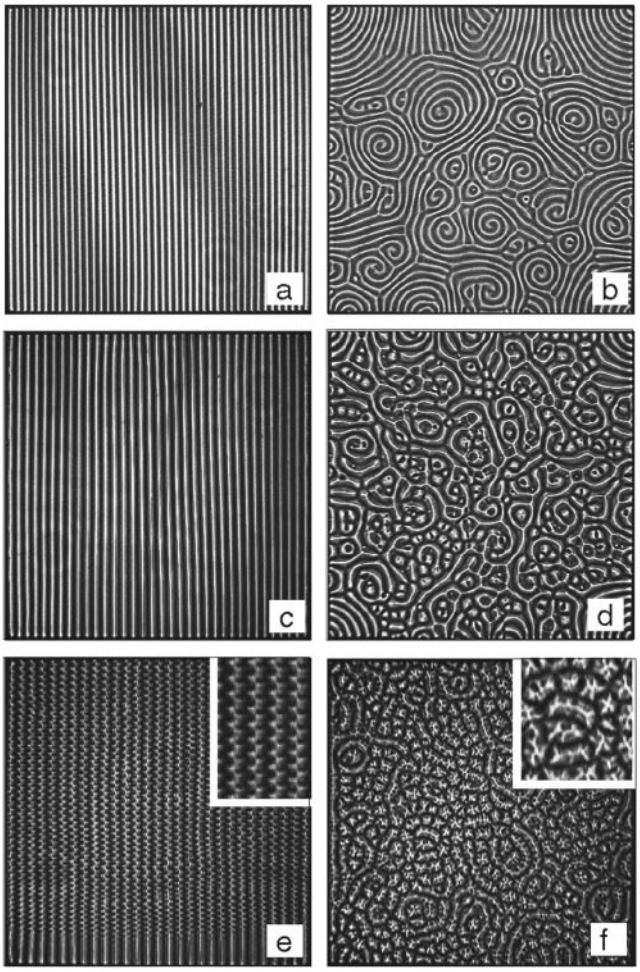

Figure 5 (a) ISR and (b) SDC at $\varepsilon = 0.92$; (c) ISR at $\varepsilon = 2.99$ and (d) SDC at $\varepsilon = 3.0$; (e) oscillatory ISR and (f) oscillatory SDC at $\varepsilon = 5.08$. For this experiment $\Gamma = 50$ and $\sigma = 1.03$. For each pair of pictures only the initial conditions were different. The insets show a magnified view of the oscillating rolls. Whereas in (e) the oscillations travel from bottom to top, in (f) the oscillations are very disordered. Often rotating spoke pattern are found, as seen in the insert of (f). From Cakmur et al (1997a).

vective (Croquette & Williams 1989b, Babcock et al 1994). Indeed, as shown in Figure 8D, the amplitude of the left-traveling waves is observed to increase downstream. Consequently, it is not surprising that the measured onset of the oscillatory instability for $\sigma = 1.03$ was found to be slightly larger than the theoretical one: Growing fluctuations have not enough time to reach visible amplitudes before they are absorbed at the lateral walls.

When ε was decreased quasistatically starting from the oscillatory regime, the ISR-pattern had a tendency to increase its wavenumber by contracting and nucleating cross rolls at the boundaries parallel to the rolls (Cakmur et al 1997a). Spiral-defect chaos then nucleated in the grain boundaries, and the ISR-state was destroyed (see Sect. 7). It was still possible, however, to measure the CR-

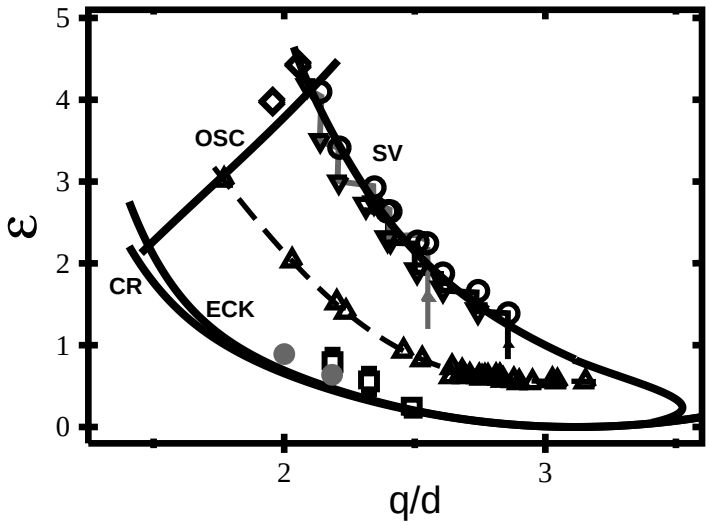

Figure 6 The stability boundaries of ISR for $\sigma = 1.03$ with experimental data. The theoretical curves are denoted SV (skewed varicose), CR (cross roll), ECK (Eckhaus), and OSC (oscillatory). The arrows indicate the path taken while increasing ε. Open circles, before SV-instability; upside-down triangles, after SV-instability; diamonds, onset of OSC-instability; squares, localized CR-instability for decreasing ε; solid circles, numerically determined boundary for localized CR-instability; triangles, wavenumber of spiral defect chaos as measured at the maximum of the azimuthally averaged power spectrum. From Plapp (1997).

instability-boundary by decreasing ε sufficiently rapidly so as to avoid pattern relaxation in the bulk. Surprisingly, three different nonlinear evolutions of the CR-instability were found. As shown in Figure 9A for $\varepsilon = 0.80 \pm 0.15$, a cross-roll defect nucleated at one of the sidewalls and propagated in a direction that increased the wavenumber in the wake. For $\varepsilon = 0.57 \pm 0.15$ the cross-roll defect left behind a disordered totem-pole-like pattern while moving through the system (Figure 9B). For $\varepsilon = 0.25 \pm 0.10$ the CR-instability occurred in the bulk (Figure 9C).

These local CR-instabilities were also found in numerical simulations when, for fixed ε, an ISR-pattern was initialized with two oppositely charged dislocations and a wavenumber close to the CR-boundary. The results of the simulations are as shown by the solid circles in Figure 6. In the simulations, the totem-pole pattern leads to the nucleation of SDC.

Whereas the bulk instability is similar to the one observed for larger Prandtl number fluids (Busse & Whitehead 1971), the other two are localized CR-instabilities. Localized CR-instabilities were first observed by Croquette (1989a); however, due to the small aspect ratio used in the experiment it was not possible

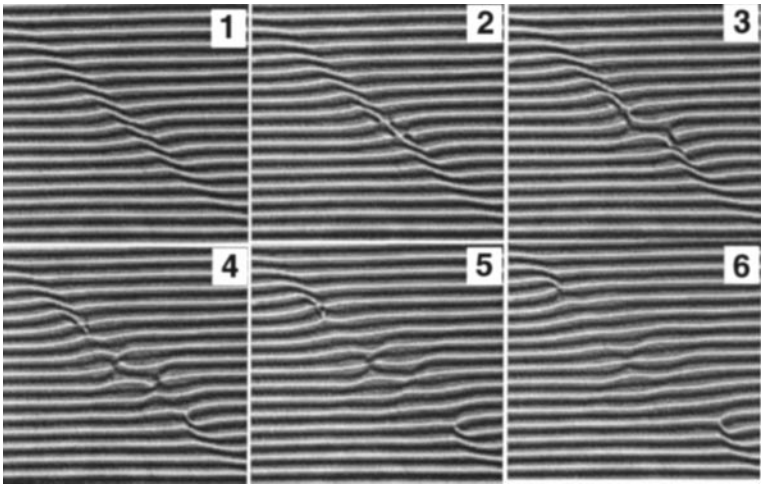

Figure 7 Time evolution of the skewed-varicose instability at $\varepsilon = 2.26$, $\sigma = 1.07$ [about 7.5 minutes ($183t_v$) after ε was increased from 2.23]. Pictures are spaced $0.54t_v$ apart. From Plapp (1997).

to study the full dynamics. The localized CR-instability has also been called a bridging instability (Newell & Passot 1992, Assenheimer & Steinberg 1994) and has been associated with a different nonlinear effect.

6. CIRCULAR CELLS

6.1 PanAm Patterns

As discussed above, close to onset, pseudo-ISRs are stable in circular as well as in rectangular geometries. However, for circular cells there is a tendency to form short cross rolls near that part of the sidewall where the rolls would otherwise be parallel to the wall (see Figure 4a). The cross-roll patches, separated by grain boundaries from the bulk, are a manifestation of an often-observed tendency for rolls to terminate with their axes perpendicular to the sidewalls. This orientation at the boundaries is also typically observed in numerical simulations without forcing lateral boundary conditions (see e.g. Figure 1). Loosely speaking, this configuration minimizes the friction experienced by the rolls at the walls. With increasing ε, this effect becomes more pronounced.[14] In circular convection cells it leads to enhanced roll curvature in the pattern interior. As the curvature increases, the domain walls shrink and form focus singularities at the wall (wall

[14]For recent references see Croquette (1989b), Hu et al (1993, 1994, 1995a), Pocheau & Daviaud (1997)

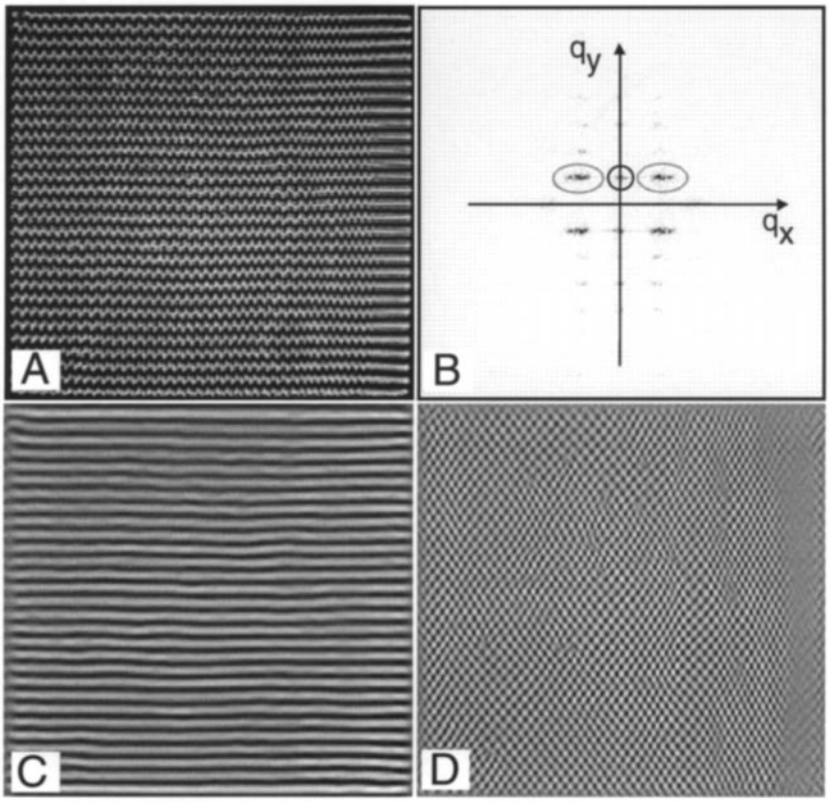

Figure 8 (A) Left traveling oscillations; (B) power spectrum of (A) with marked demodulation areas; (C) undistorted roll structure obtained by back-transform of the black-encircled area in (B); and (D) disordered checkerboard structure obtained by back-transform of the gray-encircled area in (B). For this example, $\varepsilon = 5.1$ and $\sigma = 1.02$. After Cakmur et al (1997a).

foci). In relatively small-aspect-ratio systems, typically two wall foci form, and then for obvious reasons the resulting structures often are referred to as PanAm patterns. For larger Γ, however, three or more wall foci can form as ε increases, and more complicated structures arise. An example of a PanAm pattern is given by the smallest sample shown in Figure 10B. More complicated textures are shown in Figure 10A. While this situation is generic for quasi-static increase of ε, transient sidewall forcing can also select target patterns (see Section 6.2) that (in the presence of some static sidewall forcing) are stable in the same ε range as the curved rolls with wall foci. This is illustrated by the larger samples in Figure 10B.

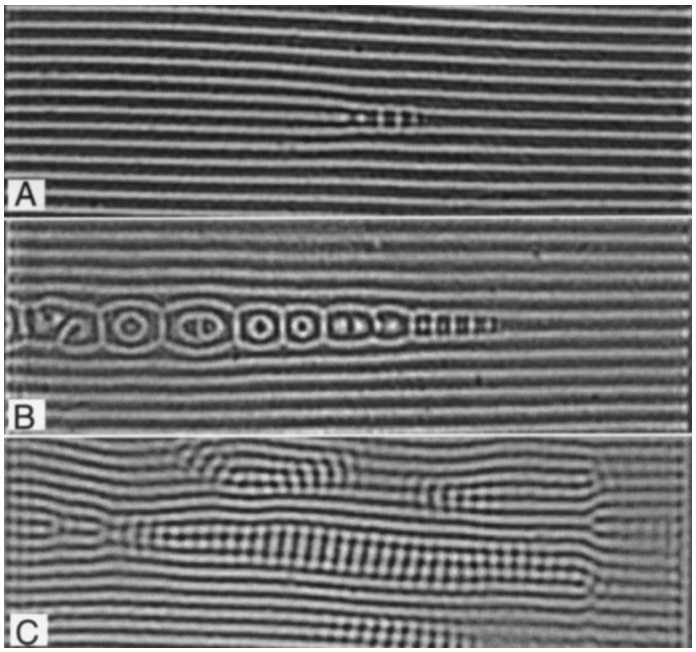

Figure 9 Cross-roll instabilities for $\sigma = 1.1$: (A) CR defect propagates from left to right, thus increasing the pattern wavenumber ($\varepsilon = 0.80 \pm 0.15$); (B) CR defect propagates from right to left, leaving behind a totem pole pattern ($\varepsilon = 0.57 \pm 0.15$); (C) CR-instability in the sample interior ($\varepsilon = 0.25 \pm 0.10$). From Plapp (1997).

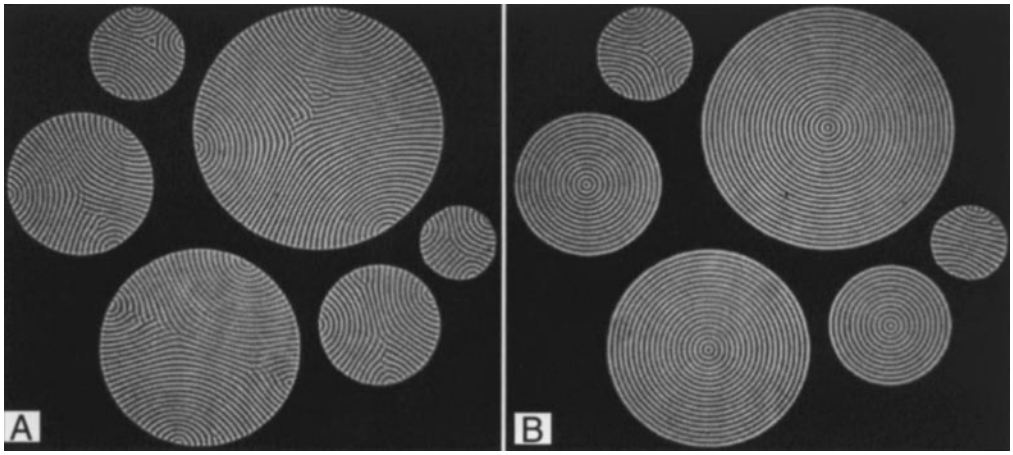

Figure 10 An example of (A) PanAm ($\varepsilon = 0.34$, $\sigma = 1.39$) and (B) target patterns ($\varepsilon = 0.38$, $\sigma = 1.40$) in the same convection cells with $\Gamma = (48.4, 38.8, 28.4, 23.8, 19.1, 14.9)$ for different experimental paths. From Plapp (1997).

The competition between curvature and sidewall obliqueness was examined theoretically by Cross (1982). A functional of the wavevector field was derived that had contributions from wavenumber variations, from roll curvature, from sidewall obliqueness, and from defects. The minimization of this functional drives the selection of the pattern. Semiquantitatively, these predictions were confirmed by experiments with $\sigma \gg 1$ (Heutmaker et al 1985, Heutmaker & Gollub 1986, 1987). However, for $\sigma \simeq 1$, mean-flow effects are important. Indeed, it was shown experimentally by Daviaud & Pocheau (1989) that suppression of the mean flow dramatically reduces the roll curvature. When large-scale flows have a strong influence on the pattern, the applicability of a model with a potential seems in question even for relatively small ε-values.

The stability of ISR is described by the Busse balloon (see Sects. 3 and 5). The stable states are limited at the low-wavenumber side by the ECK- and the CR-instabilities and at the high-wavenumber side by the SV-instability. An important, as yet largely unanswered, question is which of the continuum of stable states will be selected by the physical system. There is no known extremum principle. Instead it appears that preferred wavenumbers are chosen by a given set of boundary conditions, defects, and/or histories. For example, for a circular cell of aspect ratio $\Gamma \lesssim 60$ the domain walls separating the cross rolls from the main rolls permit a continuous wavenumber adjustment in the cell interior. It was found experimentally for circular cells (Hu et al 1993; J Liu, KMS Bajaj, G Ahlers, unpublished) that this leads to the selection of a unique wavenumber, as shown by the plusses and open circles in Figure 11. When ε reaches a value of about 0.1, the selected wavenumber is close to the SV-instability. Indeed, the roll curvature that prevails at this point (wall foci developed) leads to a significant wavenumber distribution, with the largest q in the sample interior. These largest wavenumbers cross the SV-instability at $\varepsilon \simeq 0.11$. Then defect nucleation begins in the cell interior, as noted by Croquette (1989b). Although the elimination of a roll pair by the defect creation and migration moves the system back into the

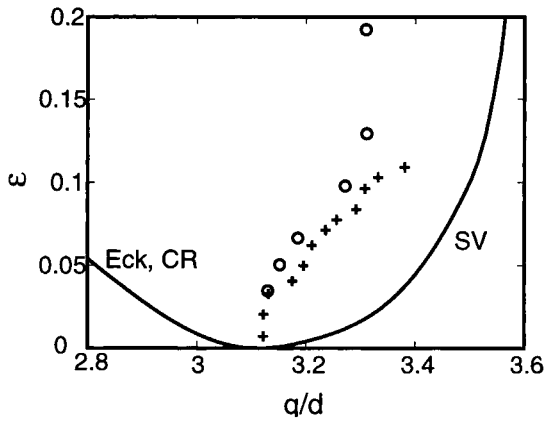

Figure 11 The stability boundaries of ISR for $\sigma = 1.0$. The data points are the measured wavenumbers selected by the domain walls characteristic of straight-roll patterns in circular containers. The plusses are for $\Gamma = 41$ (Hu et al 1993) and the open circles are for $\Gamma = 29$ (J Liu et al, unpublished).

stable interior of the Busse balloon, the wall foci emit new rolls, and a time-dependent state persists (Croquette 1989b; Hu et al 1994, 1995a). This is discussed further in Section 6.4.

6.2 Targets

Even in very carefully constructed experimental cells, the existence of sidewalls can introduce horizontal thermal gradients near them. This can have a surprisingly strong impact on the pattern-formation processes (see e.g. Cross & Hohenberg 1993, Sect. VIII.D1, and de Bruyn et al 1996).[15] The gradients have the tendency to drive flow fields that have the symmetry of the walls. Static (time independent) forcing occurs, for instance, when the conductivity of the walls is significantly different from that of the fluid and the conductivity of the top or bottom plate is finite, albeit large. In some experiments, static forcing was induced deliberately by embedding a heater in the sidewall (see, for instance, Croquette 1989a, Morris et al 1996). Sidewall forcing can also be dynamic due to a mismatch of the thermal diffusivity between sidewall and fluid. In that case, a change in, for instance, the bottom-plate temperature will cause vertical temperature profiles that relax at different rates in the wall and in the fluid, again leading to (in this case transient) horizontal gradients near the wall.

In circular cells, sidewall forcing (transient or static) can lead to concentric patterns, also known as targets, like those in Figure 10B. Such patterns have been investigated in numerous experiments.[16] They are found to be stable for small ε until, with increasing ε, an instability known as the focus instability (Newell et al 1990) occurs at their center.

An interesting aspect of concentric patterns in their stable range (below the focus instability) is an anomalous variation of the amplitude A of their umbilici, i.e. target centers, which was noted qualitatively by Croquette et al (1986a). This is illustrated by the solid circles in Figure 12, which represent more recent quantitative measurements (Hu et al 1993) of A^2 as a function of ε on logarithmic scales. The data can be fit by a line with a slope of ½, indicating that $A \propto \varepsilon^{1/4}$. This can be compared with the ε-dependence of the roll amplitude well away from the center of the pattern, which is shown as open circles and which is consistent with $A \propto \varepsilon^{1/2}$ as predicted on the basis of the Landau equation for a supercritical bifurcation. The unusual behavior of the umbilicus amplitude occurs because the Landau equation is not applicable (Brown & Stewartson 1978, Ahlers

[15]The origin and effect of static and dynamic sidewall forcing has been investigated by numerous authors, both theoretically and experimentally. Among them are Ahlers et al (1981), Cross et al (1983), Ahlers et al (1984), Steinberg et al (1985), Bodenschatz et al (1991, 1992a), Hu et al (1993), de Bruyn et al (1996), Plapp & Bodenschatz (1996), Plapp et al (1998).

[16]Among them are Koschmieder (1974), Koschmieder & Pallas (1974), Croquette et al (1983), Bodenschatz et al (1991, 1992a), Hu et al (1993), Plapp & Bodenschatz (1996), Plapp et al (1998).

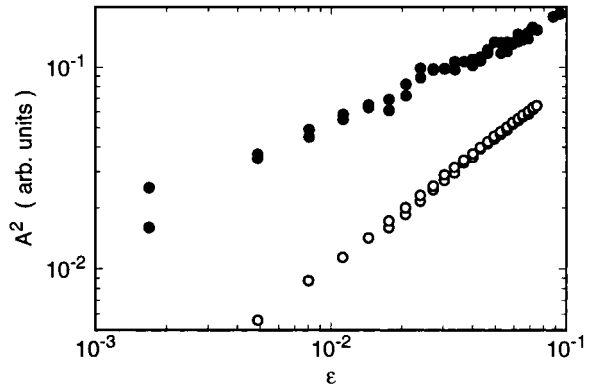

Figure 12 The amplitude of the umbilicus (solid circles), and of the rolls away from the center (open circles), in a circular cell with $\Gamma = 43$ as a function of ε on logarithmic scales. After Hu et al (1993).

et al 1981) at the pattern center, as was explained by Pomeau et al (1985), who predicted the exponent value ¼ in the limit of a large-aspect-ratio cell.

The events that occur as ε is increased beyond the focus instability depend on the strength of the sidewall forcing, the wavenumber, the aspect ratio, and the Prandtl number. They have not yet been predicted by theory. One set of events observed in experiments is that the umbilicus drifts away from the center and toward the wall, thus destroying the concentric pattern (Hu et al 1993). Another involves the periodic emission of outward-traveling concentric rolls (Hu et al 1993). Yet another observed scenario is that the umbilicus moves slightly off center, and then re-stabilizes at a smaller pattern wavenumber by destroying one concentric roll pair near it (Croquette et al 1983, Steinberg et al 1985). A further mechanism involves an off-center displacement of the umbilicus, which is followed by radial oscillations of the umbilicus position (Plapp 1997).

When the focus instability leads to a change in the number of concentric convection rolls and the sidewall forcing is sufficiently strong, the concentric nature of the pattern can be maintained over a large ε range and the umbilicus provides a wavenumber-selection mechanism.[17] The selected wavenumber depends significantly on the Prandtl number and can be larger (small σ) or smaller (large σ) than q_c. It was calculated by several authors (Manneville & Piquemal 1983, Cross 1983, Buell & Catton 1986a), and there is generally good agreement with the measurements.

[17]Experiments were performed, for instance, by Koschmieder (1974), Croquette et al (1983), Croquette & Pocheau (1984), Steinberg et al (1985), Croquette et al (1986a), Plapp (1997), and Plapp et al (1998).

6.3 Giant Spirals

Multi-armed, giant, rotating spirals were observed in a number of experiments with $\sigma \simeq 1$.[18] They were discovered by Bodenschatz et al (1991), and studied in detail by Plapp and coworkers (Plapp & Bodenschatz 1996, Plapp 1997, Plapp et al 1998), who investigated their formation, dynamics, selection, and stability. Multi-armed spirals can be obtained by appropriate jumps in ε or by increasing ε slowly. Some static sidewall forcing seems required to prevent the center of the large structure from drifting toward the sidewall. One example of spiral creation is illustrated in Figure 13. In this case, the umbilicus of an initial target moved off center after ε was increased quasistatically. Compression of the rolls in the

[18]Bodenschatz et al (1991, 1992b); Assenheimer (1994); Plapp & Bodenschatz (1996); Plapp (1997); Plapp et al (1998)

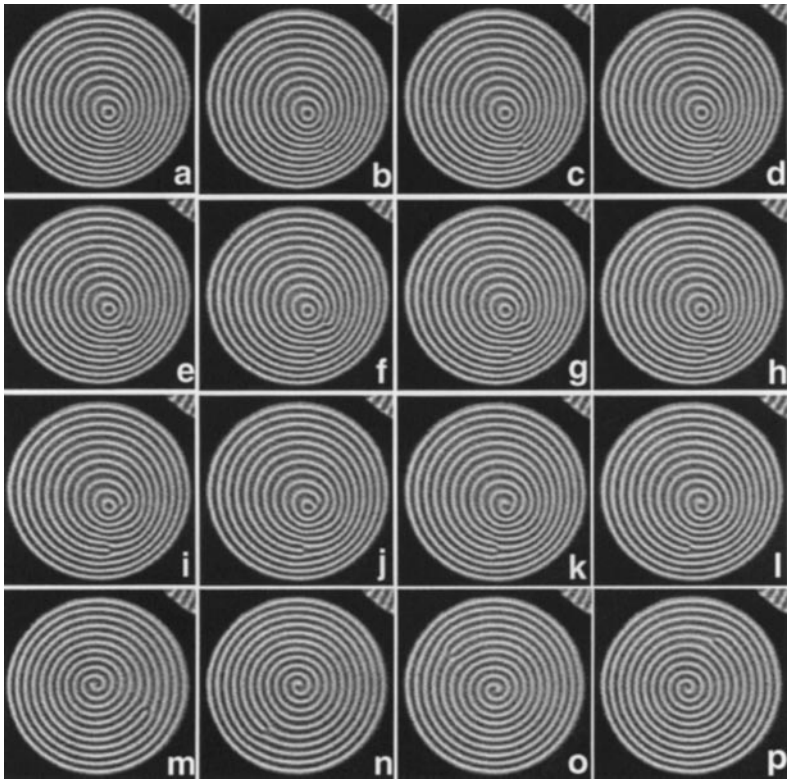

Figure 13 (a) to (l): Birth of a one-armed clockwise-rotating spiral for $\Gamma = 43$ and $\sigma = 1.38$ after ε was increased from 0.58 to 0.60. Pictures (a) to (h) are spaced $0.5t_v$ apart, and (h) to (l) are at intervals of $1.5t_v$. (m) to (p): A rotating, single-armed spiral. The pictures are spaced $82t_v$, or a 1/4 period, apart. From Plapp (1997).

lower right part of the pattern increased the local q beyond the SV-instability and caused a dislocation pair to be formed. One of the dislocations moved to the center of the target while the other remained at a finite radius from it, thus creating a one-armed spiral.

N-armed spirals rotate slowly by emitting radially traveling waves that are annihilated by *N* dislocations that rotate synchronously with the spiral heads (Bodenschatz et al 1991, 1992b). Beyond the dislocations the spiral arms are surrounded by a target pattern. The core of an *N*-armed spiral consists of *N* bound dislocations of equal topological charge (Plapp et al 1998). By time-averaging a giant spiral over one rotation period, it is possible to recover the underlying target pattern (Plapp et al 1998). This is shown for the example of a three-armed spiral in Figure 14. Also shown is the fast core rotation that can be observed for multi-armed spirals (Plapp & Bodenschatz 1996, Assenheimer 1994).

With increasing ε, giant spirals can adjust their wavenumber by changing the position of the core with respect to the revolving dislocation (Plapp 1997). The spiral either winds up or unwinds to adjust its wavenumber, as illustrated in Figure 15. Once the wavenumber is adjusted, the spiral's tip at the core is locked in

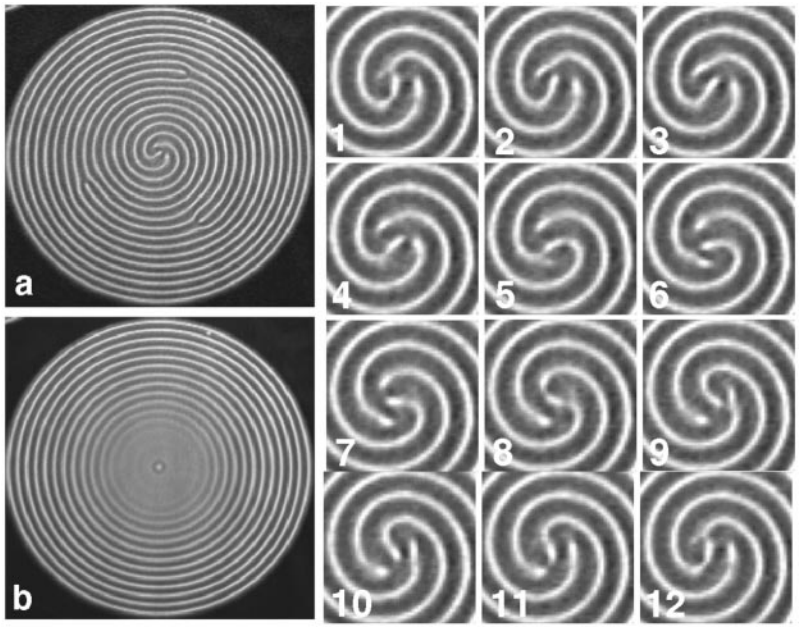

Figure 14 (a): Snapshot of a three-armed spiral for $\Gamma = 38.8$, $\varepsilon = 0.79$, and $\sigma = 1.37$. (b): Average of images like that in (a), covering one period of rotation. (1) to (12) show the fast core rotation over one period. Here frames are spaced $0.44t_v$ apart. From Plapp & Bodenschatz (1996) and Plapp (1997).

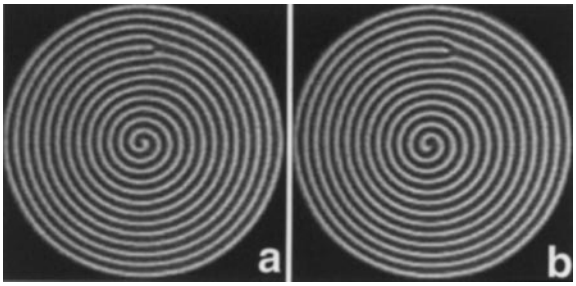

Figure 15 Wavenumber adjustment of a one-armed spiral for $\Gamma = 28.4$ and $\sigma = 1.38$. (a) $\varepsilon = 0.55$ and (b) $\varepsilon = 0.72$. The spiral adjusts its wavenumber by unwinding. Note the position of the outer defect in relation to the core. From Plapp (1997).

relation to the outer defect. In fact spirals are found to decrease their wavenumbers continuously with increasing ε, as shown in Figure 17.

As ε is increased further, the spiral structures become unstable (Plapp 1997, Plapp et al 1998). Typically the cores move off center and cause a local increase of q beyond the SV instability. The pattern develops many dislocations. Depending on parameters, the structure evolves into a many-armed spiral, a texture with wall foci, or spiral-defect chaos. Interestingly, as shown in Figure 16, bistability between rotating spirals, and the spatio-temporal chaotic planforms of spiral-defect chaos and PanAm-like patterns were observed.

The rigid rotation of a stable giant spiral requires that the radial waves that propagate from the center are annihilated at a radius $r = r_d$ by the circular motion of the outer defect. Thus for $r > r_d$, a concentric stationary roll pattern results. Arguments based on the phase-diffusion equation (see Sect. 3.3) can be used to quantitatively describe the large-scale rotation of the spirals. It was proposed (Cross & Tu 1995, Cross 1996, Li et al 1996) that the rotation of giant spirals requires the reconciliation of two competing wavelength-selection mechanisms acting far away from the spiral's core, namely wavelength selection by defect climb and target wavelength-selection by radially traveling waves. Meanflow effects are important in selecting the velocity of a dislocation in ISR, as was pointed out first by Siggia & Zippelius (1981a). Later Tesauro & Cross (1986) predicted that the motion of a dislocation at sufficiently high ε should be captured by

$$v_d = \beta(\varepsilon)(q - q_d(\varepsilon)), \tag{11}$$

where q_d is the wavenumber for which a dislocation does not move and q is the background wavenumber (defined in Plapp et al 1998). It was argued (Cross & Tu 1995, Cross 1996, Li et al 1996) that the relation (Equation 11) should apply as well to the dynamics of the outer defects of giant spirals, i.e., $\omega_d = v_d(r)/r$ for $q = q(r)$. Plapp et al (1998) verified this relationship in both experiments and simulations. They found that for $\sigma = 1.4$, the wavenumber $q_d(\varepsilon)$ decreased with increasing ε. This is shown for the example of a cell of $\Gamma = 38.8$ in Figure 17.

Away from the core of the spiral, the wavefronts deviate only slightly from circular, and their wavenumber-selection properties are thus well approximated

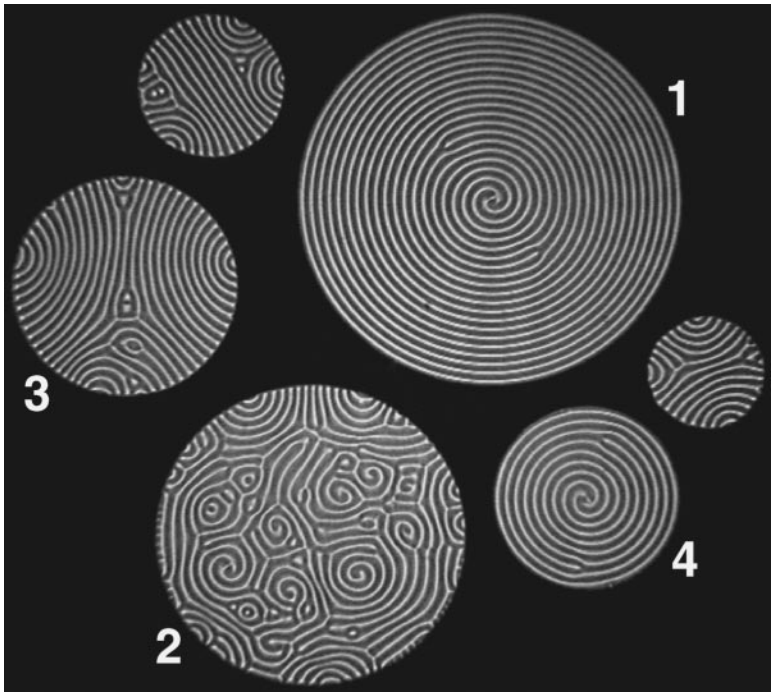

Figure 16 Two-armed spiral patterns in cell *1* and *4*. Spiral defect chaos in cell *2*. Textures with wall foci in cell *3* and the unmarked cells. For these images, $\varepsilon = 0.98$ and $\sigma = 1.4$. From Plapp et al (1998).

by those of targets. Targets select a specific wavenumber $q_t(\varepsilon)$ (Newell et al 1990) (see also Sect. 6.2). If the prevailing q differs from q_t, spirals will thus attempt to adjust their wavenumber by emitting circular waves of frequency $\omega_t(\varepsilon)$. From the nonlinear Cross-Newell phase-diffusion equation (Newell et al 1990), one finds

$$\omega_t = \alpha(q_t(\varepsilon) - q)/r, \tag{12}$$

where $\alpha = 2D_\parallel(q_t)$, $D_\parallel(q)$ is the parallel diffusion constant, and r is the distance from the center of the target. The numerical value of the parameter α can be calculated from the growth rate $\sigma(K)$ at q_t of the Eckhaus instability as $\alpha = (-2\sigma(K^2)/K^2)|_{K\to 0}$, where K is the wavenumber of the disturbance (Plapp et al 1998).

Plapp et al (1998) measured q_t from the target patterns they observed for small ε and found quantitative agreement with the theoretical predictions by Buell & Catton (1986b). By extrapolating $q_t(\varepsilon)$ to larger ε, and by measuring the spiral-selected wavenumber $q(\varepsilon)$, they were able to determine $\alpha(\varepsilon)$. Again, they found

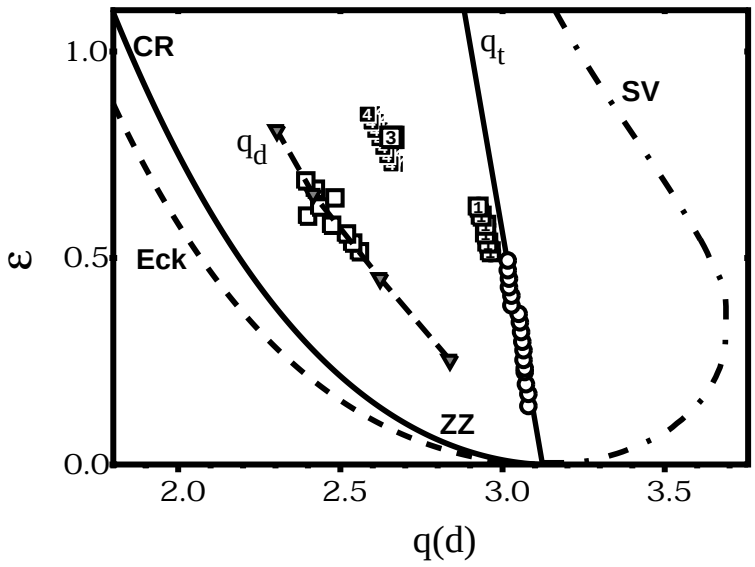

Figure 17 Wavenumbers selected by targets, spirals, and dislocations for a circular cell of $\Gamma = 38.8$ for $\sigma = 1.4$. The region marked q_d gives the experimentally (squares) and theoretically (triangles and dashed line) determined dislocation-selected wavenumbers. The open circles show the target-selected wavenumber q_t and the solid line is the extrapolation to larger ε. The square symbols marked 1, 3, and 4 represent the selected wavenumbers of one-, three-, and four-armed spirals. Also shown is the Busse balloon. After Plapp (1997).

good agreement with the numerically determined value obtained from the growth rate of the Eckhaus instability.

In the theoretical calculations it is implicitly assumed that the coupling by mean flow between the spiral's core and the orbiting dislocations does not play an important role, at least not for the determination of the rotation frequency. In Figure 18, a snapshot of the central region of a right-handed spiral is shown. Note that the induced mean flow is indeed confined to the core region. Surprisingly, the mean flow is in a direction that, in principle, has the tendency to unwind the spiral locally by advection. It seems clear that the coupling of the tips of multi-armed spirals by mean flow is responsible for the fast dynamics at their core.

In summary, the rotation of on-center, giant spirals can be understood in terms of two competing wavelength-selection mechanisms. As shown in Figure 17, the revolving defects attempt to select a small wavenumber, whereas the target-like curvature of the rolls attempts to select a larger wavenumber. Thus the rotating *N*-armed spirals select an intermediate wavenumber where both selection mechanisms are in balance. It has to be noted, however, that the more complex situa-

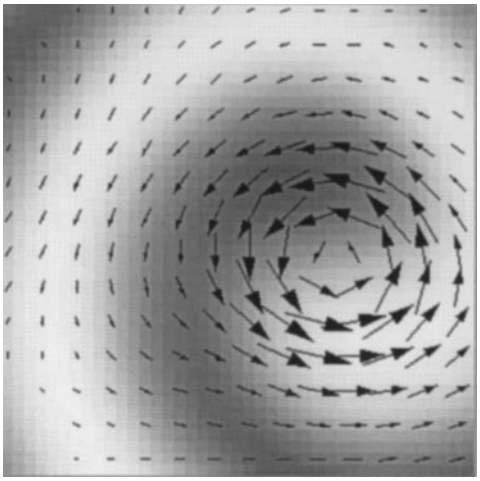

Figure 18 The core region of a right-handed, one-armed spiral from numerical simulations at $\sigma = 1$. The arrows indicate the strength and direction of the mean flow.

tions, such as the dynamics of off-center spirals, the core rotation, and the spiral instability, are not understood and remain a challenge.

6.4 Textures

Here we discuss in more detail typical sidewall-mediated phenomena that occur in circular cells and lead to increasing disorder and to persistent dynamics as ε is increased. For $\varepsilon \lesssim 0.1$, we saw in Section 6 and Figure 11 that the selection process due to cross rolls yields mean wavenumbers that, with increasing ε, approach the SV-instability. In addition, roll curvature increases and the obliqueness of the roll axes relative to the sidewalls decreases with increasing ε. This process leads to a broadening wavenumber distribution throughout the cell, with the largest wavenumbers typically in the center of the sample. This is illustrated by images (*a*) and (*b*) in Figure 19 and described quantitatively by the results shown in Figure 20 that were obtained from real-space image-analysis by Hu et al (1995a). Figure 20a gives results for the average obliqueness $\beta \equiv \langle |\mathbf{n}\cdot\mathbf{s}| \rangle$ ($\mathbf{n}$ is the normalized roll wavevector near the wall and $\mathbf{s}$ is the sidewall normal vector), where the average is taken along the sidewall and over many statistically independent images. One sees that β decreases with increasing ε in the range $\varepsilon \lesssim 0.17$ (for larger ε it remains essentially constant). The average roll curvature $\gamma \equiv \langle |\nabla \cdot \mathbf{n}| \rangle$, taken over the cell interior and over many statistically independent images, increases over the range $\varepsilon \lesssim 0.13$ and then remains essentially constant until the onset of SDC, near $\varepsilon = 0.6$, causes it to rise dramatically.

As noted by Croquette (1989b), the compression of the rolls in the interior, which accompanies the enhanced roll curvature, causes the wavenumber in the cell center to exceed the SV-instability when $\varepsilon \simeq 0.11$ and leads to the formation of dislocation pairs. This can be seen in Figure 19b. These defects then travel

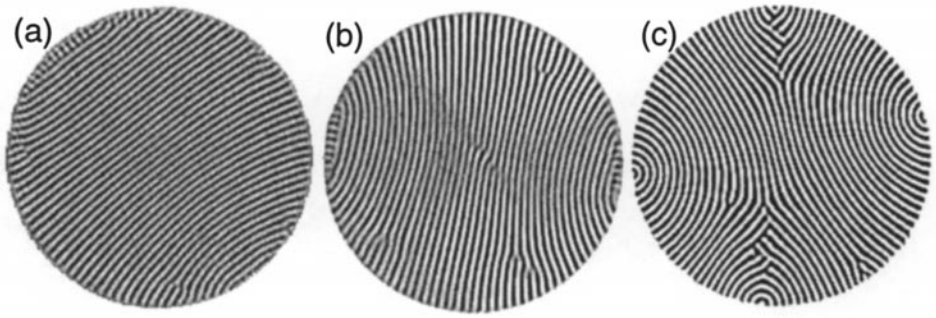

Figure 19 Patterns in circular cells for $\sigma \simeq 1.0$. (a): $\varepsilon = 0.09$, $\Gamma = 40$. (b): $\varepsilon = 0.12$, $\Gamma = 41$. (c): $\varepsilon = 0.34$, $\Gamma = 41$. From Hu et al (1993) and Hu et al (1995a).

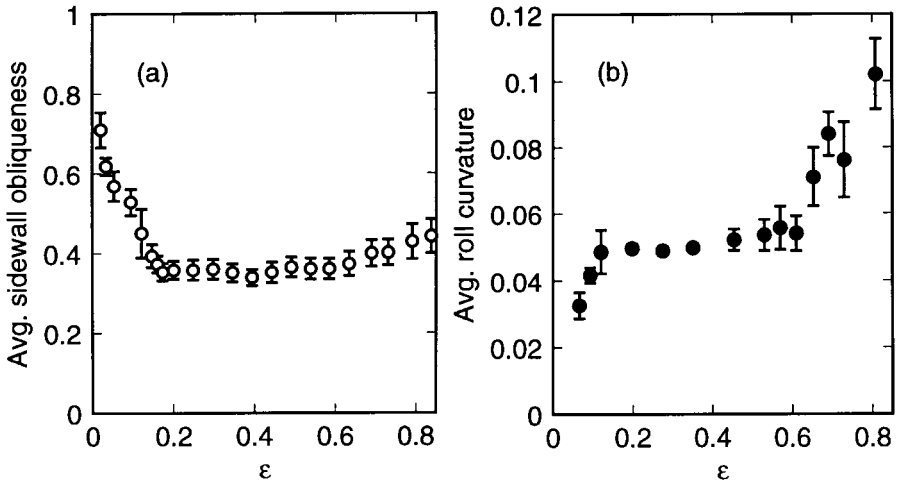

Figure 20 (a) Sidewall obliqueness and (b) average roll curvature in a circular cell with $\Gamma = 40$ and $\sigma = 1.0$. The vertical bars give the standard deviations of the distributions used to calculate the average values. From Hu et al (1995a).

toward the cell wall by a combination of climb and glide in a direction relative to the roll axes that is determined by the direction of the SV perturbation with the maximum growth rate (Hu et al 1997). The result of this process is a reduction of q to a value less than q_{SV} and thus of a re-stabilization of the pattern. However, the domain walls emit new rolls, which gradually re-compress the ones in the center and thus lead to a persistent time dependence. This case is an example of the creation of a time-dependent state via the selection of an unstable state. A similar situation prevails for Taylor-vortex flow (TVF), where an Eckhaus-unstable state can be selected for a certain family of spatial ramps in the control

parameter (Riecke & Paap 1987, Ning et al 1990, Wiener et al 1997). The TVF case was examined in detail theoretically (Riecke & Paap 1987). The selected wavenumber, the value of ε for the onset of time dependence, and the frequency of the events beyond onset were calculated, and there is good agreement between experiment (Ning et al 1990) and theory. In the RBC case we do not know of predictions for the selection involving the domain walls, and the problem involving curved rolls is two-dimensional and thus more complicated than the TVF case. Above the onset of time dependence, the experiments showed that the process can be periodic or chaotic, apparently depending sensitively on ε, Γ, and σ.

As ε increases further, the domain walls shrink in length. Near $\varepsilon = 0.13$ they typically have contracted to point singularities known as wall foci (Hu et al 1994, 1995a). Examples can be seen in Figures 19c and 10A. Meanwhile, the roll curvature has saturated at a value that is independent of ε over the range $0.13 \lesssim \varepsilon \lesssim 0.6$ (see Figure 20b). Like the domain walls, the wall foci emit rolls and thus keep the dynamics of the pattern sustained. The frequency of roll emission increases strongly with increasing ε (Hu et al 1995a). Other defect structures besides the SV-generated dislocations occur as well in this ε-range, as can be seen in Figure 19c. The most dominant are oscillating domain-wall structures in the cell interior where rolls meet at an angle (Hu et al 1995a). Examples are visible near the top and bottom of Figure 19c. The role of these various structures in the dynamics of the pattern is not understood in detail.

The evolution with ε of the mean wavenumber[19] $\langle q \rangle$ is shown as crosses in Figure 21 for a sample with $\Gamma = 40$. As we saw in Section 5, $\langle q \rangle$ first moves to

[19] $\langle q \rangle$ was determined by calculating the first moment of the structure function $S(q)$ (the azimuthal average of the square of the modulus of the Fourier transform of the images; see Morris et al 1996).

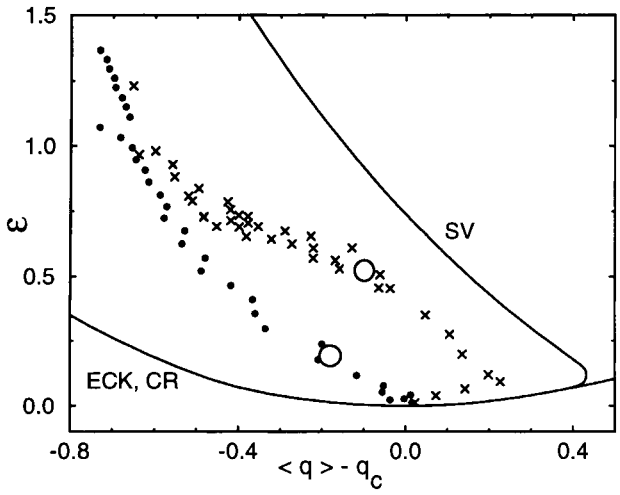

Figure 21 Selected mean wavenumbers as a function of ε. The solid circles are from Morris et al (1996) for $\Gamma = 78$ and $\sigma = 0.95$. The crosses are from Hu et al (1995a) for $\Gamma = 40$ and $\sigma = 0.98$. The large open circles are the onset at ε_s of SDC. After Hu et al (1995a).

larger values as ε increases. When SV events are first encountered near $\varepsilon \simeq 0.11$, $\langle q \rangle$ turns around and evolves along a line that is parallel to the SV boundary. Throughout this ε-range, the wavenumber in the cell center is very close to q_{SV}, and repetitive SV events are taking place. Near $\varepsilon = 0.6$, where SDC first emerges, $\langle q \rangle$ moves further away from the SV boundary and into the Busse-balloon interior.

Interestingly, the behavior of $\langle q \rangle$ is quite different for very large Γ. This is illustrated by the data taken by Morris et al (1996), which are for $\Gamma = 78$ and which are given in Figure 21 by the solid circles. In this case the system never approaches the SV-instability. Apparently, in very large systems different types of defects appear in the pattern even at quite small ε and lead to a selection mechanism that differs from the domain-wall mechanism. The different path in the $\varepsilon - q$ plane leads to the onset of SDC at the much smaller value $\varepsilon_s \simeq 0.2$.

6.5 Hexagons

Experiments in RBC are usually designed to yield small temperature differences, so that the temperature dependence of material properties may be neglected and the Oberbeck-Boussinesq approximation (see Sect. 3) may be used in the corresponding theory. In that case the bifurcation is supercritical and leads to ISR, as discussed in Sections 3 and 5. However, in experiments with larger temperature differences non-Oberbeck-Boussinesq (NOB) effects are important. They have been discussed theoretically by several authors and most systematically by Busse (1967), who introduced the parameter

$$\mathcal{P} = \sum_{i=0}^{4} \gamma_i \mathcal{P}_i. \tag{13a}$$

to describe them quantitatively. Here $\gamma_0 = -\Delta\rho/\bar{\rho}$, $\gamma_1 = \Delta(\alpha\rho)/(2\bar{\alpha}\bar{\rho})$, $\gamma_2 = \Delta\nu/\bar{\nu}$, $\gamma_3 = \Delta\lambda/\bar{\lambda}$, and $\gamma_4 = \Delta C_P/\bar{C}_P$. The quantities $\Delta\rho$, etc., are the differences in the values of the property at the bottom (hot) and top (cold) end of the cell, and $\bar{\rho}$, etc., denote their values at the mean temperature 0.5 $(T_b + T_t)$ in the static case. The coefficients $\mathcal{P}_i$ were first calculated in the limit $\sigma \to \infty$ by Busse (1967). A new calculation (Tschammer 1997) yielded the full expressions[20]

$$\mathcal{P}_0 = 2.676 - 0.361/\sigma, \tag{13b}$$

$$\mathcal{P}_1 = -6.631 - 0.772/\sigma,$$

$$\mathcal{P}_2 = 2.765,$$

$$\mathcal{P}_3 = 9.540,$$

[20]The value of $\mathcal{P}_3$ differs significantly from the original calculation by Busse (1967).

$$\mathcal{P}_4 = -6.225 + 0.386/\sigma.$$

In NOB convection, the initial bifurcation is transcritical, and the nonlinear state that forms beyond it consists of hexagonal cells. Consistent with the vertical variation of the fluid properties, hexagons break the mirror symmetry at the horizontal midplane of the sample because upflow and downflow at their centers are not equivalent. For positive $\mathcal{P}$ (gases), hexagons have downflow in their centers, whereas for negative $\mathcal{P}$ (liquids), that flow is upward (Graham 1933, Busse 1967). To a good approximation, the hexagonal patterns near onset can be described by three coupled real Ginzburg-Landau equations, which have a potential. Thus many aspects of pattern formation in this system can be understood in variational terms.

NOB convection was investigated in small-aspect-ratio systems, and interesting results for the roll-to-hexagon transition were obtained (Ciliberto et al 1988, Perez-Garcia et al 1990, Pampaloni et al 1992). Penta-hepta defects in the hexagonal pattern were investigated both experimentally (Ciliberto et al 1990, 1991) and theoretically (Pismen & Nepomnyashchy 1993; Rabinovich & Tsimring 1994; Tsimring 1995, 1996). RBC with compressed gases made possible larger-aspect-ratio experiments with much higher resolution in ε than could be done before (Bodenschatz et al 1991, 1992a,b, 1993). Bodenschatz et al (1991) were able to resolve the theoretically predicted hysteresis associated with the transcritical bifurcation from conduction to hexagons (Busse 1967). This is shown in Figure 22. As ε was increased quasistatically, first only fluctuations (see Section 4) occurred (Figure 22A). Then hexagons were nucleated and expanded to fill part of the cell (Figure 22B, C). This first value of ΔT at which the pattern formed was taken as ΔT_c, corresponding to $\varepsilon = 0$ at that spatial location. The true value of ΔT_c for the deterministic system should actually be slightly larger, because for a transcritical bifurcation, the fluctuations in the experiment would be expected to cause an earlier transition. The limited size of the patch in Figure 22C can be attributed to very small variations of the cell thickness, which cause a slight spatial variation of ε. Clearly visible in Figure 22 are the fronts that separate regions with and without convection. In the steady state, the fronts are located at those spatial positions where the local ε-value is equal to ε_T where the potentials of the convecting and the conducting states are equal. When ε was decreased quasistically, the hexagons shrank to a smaller patch (Figure 22D, E) and disappeared when ε reached ε_T at their location (Figure 22*F*). For the GL equations, one can show that $\varepsilon_T = \frac{8}{9}\,\varepsilon_a$. Thus the measurement $\varepsilon_T = -(2.0 \pm 0.1) \times 10^{-3}$ corresponds to $\varepsilon_a = -(2.3 \pm 0.1) \times 10^{-3}$. This value may actually be slightly too small because of the influence of the fluctuations on the measured ΔT_c. The size of the hysteresis loop $-\varepsilon_a$ of the deterministic transcritical bifurcation is given by the theory of Busse (1967) and Equation 13a as $\varepsilon_a = -2.2 \times 10^{-3}$, in excellent agreement with the experimental value.[21]

[21]The calculation of the theoretical values of ε_a, ε_T, and ε_T' by Bodenschatz et al (1991)

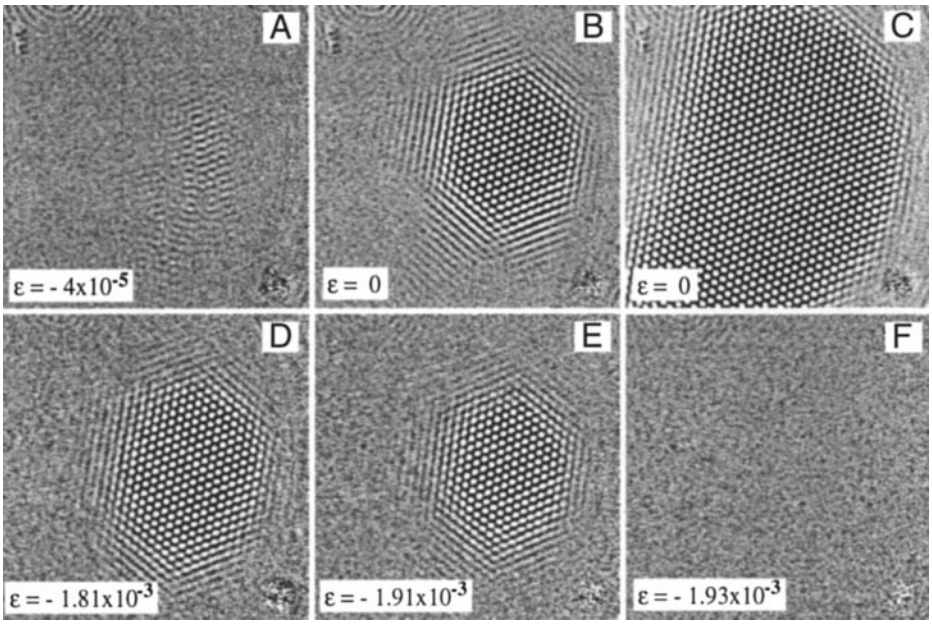

Figure 22 Transcritical bifurcation to hexagons ($\Gamma = 86$, $\sigma = 1$). (A): Fluctuating pattern below the onset of convection. (B): Nucleation of hexagons, (C): The same ε as (B) but after transients have died out. (D)–(F): ε is quasistatically decreased. The circular pattern in the *upper left* hand of the figures is caused by a dust particle. The spot at the *lower right* was caused by reduced reflectivity of the bottom-plate. Neither inhomogeneity seemed to influence the experimental observations. After Bodenschatz et al (1991).

For $\varepsilon \gtrsim 0.02$, perfect hexagonal patterns like the one shown in Figure 23A were found in the experiment by Bodenschatz et al (1991). Remarkably, even when ε was increased by a jump, initial grain boundaries and defects annihilated, and a well-ordered pattern was reached after about $15t_h$. With further quasistatic increase of ε, rolls nucleated at the sidewalls above a certain ε-value. After a long transient, a pattern consisting of a single N-armed, rotating, giant spiral was formed. Discrete steps in ε of different sizes from the hexagon to the roll regime were used to produce spirals with $0 < N \leq 13$ (Bodenschatz et al 1992a). The initial evolution of the nucleation of rolls is shown in Figures 23B, C, and D. When ε was quasistatically decreased from the n-armed spiral state, spirals like

(also in de Bruyn et al (1996)) needs to be reconsidered. The equation of state for CO_2 is now better known (de Bruyn et al 1996), and the new values of $\mathcal{P}_i$ (Equation 13b) should be used. One obtains $\mathcal{P} = 4.0$ for this experiment, which yields $\varepsilon_a = -2.2 \times 10^{-3}$ and $\varepsilon_T' = 0.13$, in excellent agreement with the experimental results. Note also typographical errors in [18] of Bodenschatz et al (1991): It should read $Z = ab/D -$ sign (a) $[a^2b^2/D^2 + a^2/2D]^{1/2}$ and the pressure should read 23.1 bar instead of 21.8 bar.

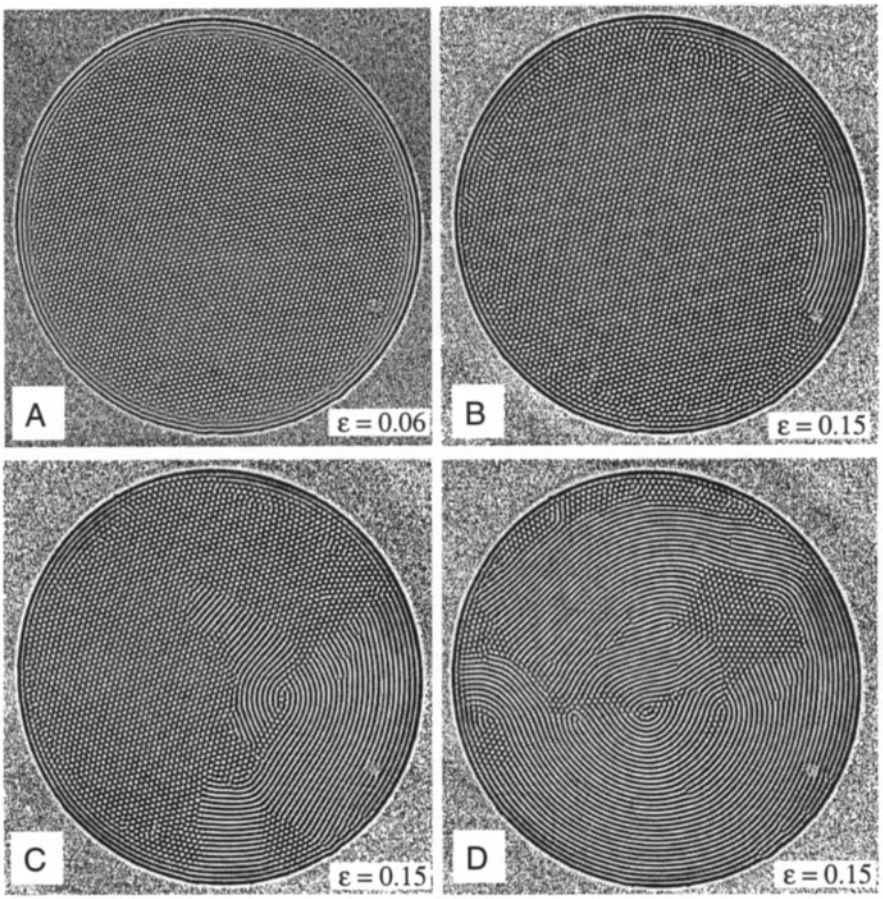

Figure 23 (A) A defect-free hexagonal pattern. (B–D) Rolls nucleate at the sidewalls and propagate into the pattern. (B), (C), and (D) are spaced $1500t_v$ apart. After Bodenschatz et al (1991, 1992a).

the one shown in Figure 24B and C decreased the number of their arms in steps of one until a target pattern (Figure 24A) was formed. With further decrease in ε, hexagons nucleated at the sidewalls as shown in Figure 24D. After a transient, a perfectly ordered hexagonal pattern was formed once again. As was the case near ε_T, the transitions between hexagons and rolls could also be understood in terms of the potential of the relevant Ginzburg-Landau equations. This transition occurred near $\varepsilon_{T'}$ where rolls and hexagons had the same potential.

Another interesting topic is the structure and dynamics of penta-hepta defects in hexagonal patterns, where instead of two neighboring hexagonal lattice cells, a pair of pentagonal and heptagonal cells is observed.

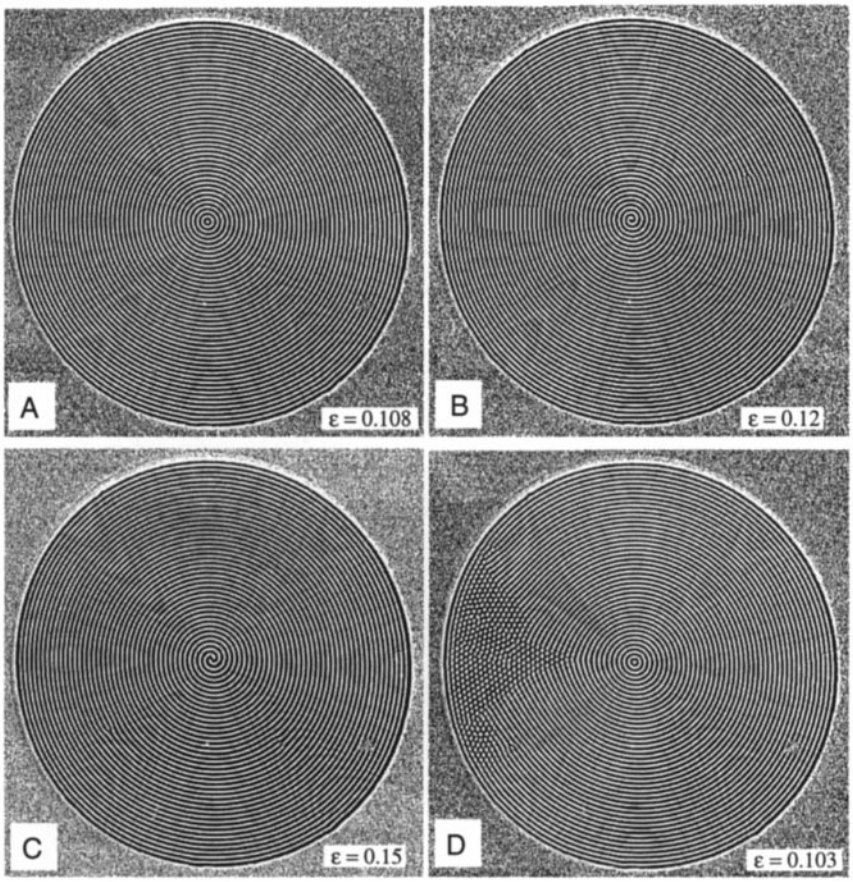

Figure 24 Target (A), one-armed spiral (B), and two-armed spiral (C). (D): Pattern during the transient from rolls to hexagons $2000t_v$ after ε was decreased from the stable target (A) at $\varepsilon = 0.108$ to $\varepsilon = 0.103$. After Bodenschatz et al (1991, 1992a).

Ciliberto et al (1990, 1991) showed that such a defect requires that two of the three superimposed roll amplitudes vanish at the defect position (as in a dislocation), while the third one remains finite. An example of a moving penta-hepta defect is shown in Figure 25A. Also shown in Figure 25C and D is the Fourier demodulation into the three sets of rolls that make up the hexagonal pattern of Figure 25A at two different times separated by $70.6t_v$. In this example the penta-hepta defect moved with a combination of glide and climb of the dislocations in the two roll patterns, while the third roll pattern remained dislocation free. The dynamics of penta-hepta defects has been investigated theoretically (Pismen & Nepomnyashchy 1993; Rabinovich & Tsimring 1994; Tsimring 1995, 1996). Based on the three coupled Ginzburg-Landau equations (Busse 1967), Tsimring

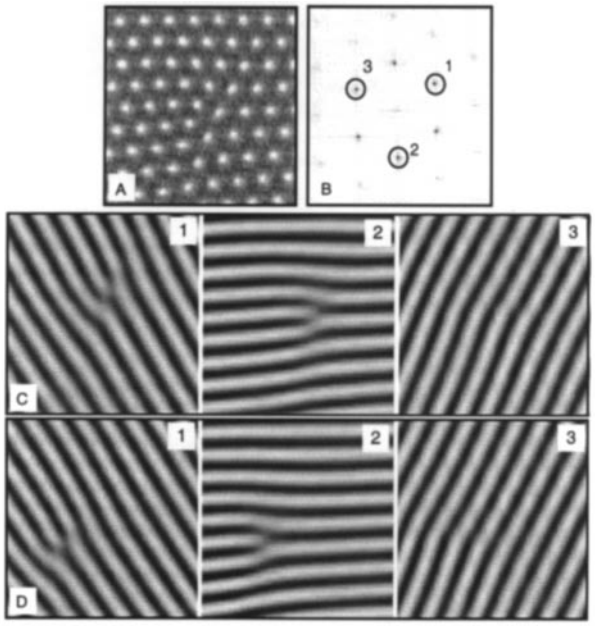

Figure 25 (A) Penta-hepta defect in a hexagonal pattern for $\varepsilon = 0.12$. (B) Modulus of the Fourier transform of this pattern. (C) The three sets of rolls obtained by Fourier back-transformation of the encircled areas in (B). (D) The sets of rolls $70.6t_v$ later than (C). After de Bruyn et al (1996).

(1995, 1996) calculated the mobility of an isolated penta-hepta defect. He also considered the interaction of a pair of penta-hepta defects. Only future experiments will be able to tell whether the predictions of this theory are as successful as their analogue in the case of electroconvection of nematic liquid crystals (Kramer et al 1990). However, in analogy to the ISR case (see Section 6.3), mean flow effects may become important once ε is sufficiently large and a description based on GL-equations may break down.

Recently, in an experiment using compressed SF_6 gas, Assenheimer & Steinberg (1996) observed the coexistence of the two types of hexagons with upflow and downflow at their centers. Later Bajaj et al (1997) confirmed this observation in an experiment using acetone as a fluid. A picture of such a convection state is shown in Figure 26. Assenheimer & Steinberg (1996b) found such patterns in a cylindrical cell of aspect ratio $\Gamma = 80$ for a Boussinesq fluid with $\mathcal{P} < 0.09$ and $2.8 \leq \sigma \leq 28$ at $\varepsilon \approx 4$. They observed that the hexagonal planforms nucleated at the centers of targets and spirals when ε was increased quasistatically (Assenheimer & Steinberg 1996b, Aranson et al 1997). This is shown in a sequence of images in Figure 27.

Bajaj et al (1997) observed the patterns for a smaller circular cell of $\Gamma = 55$ for $\mathcal{P} < 0.4$, $\sigma = 4$, and $\varepsilon > 4.5$. In their experiment the hexagons nucleated near sidewall foci. Clever & Busse (1996) showed numerically that up-down hexagons constitute another stable attractor aside from rolls for the experimental values of σ.

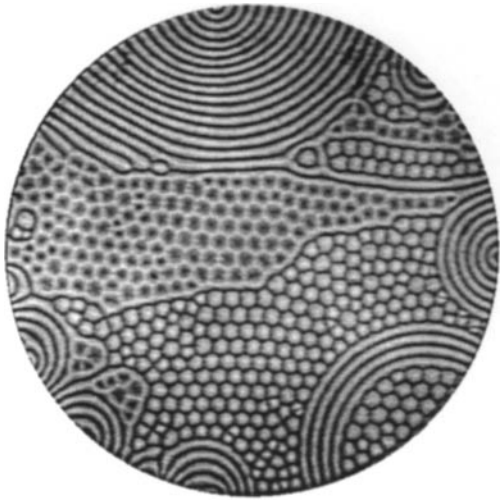

Figure 26 Coexisting up- and down-flow hexagons together with rolls for $\Gamma = 80$ and $\sigma = 4.5$. The hexagon wavelength is about 20% larger than the roll wavelength. From Assenheimer & Steinberg (1996b).

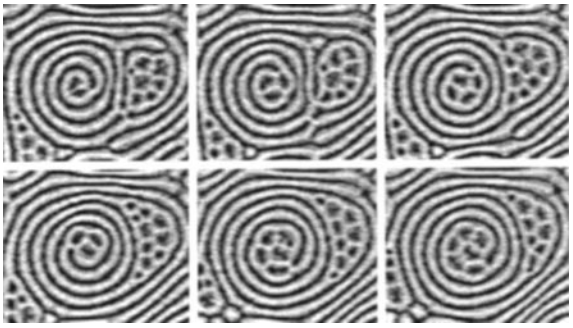

Figure 27 Experimental hexagon nucleation at a spiral core for $\sigma = 4.5$ and $\varepsilon = 3.19$. The pictures are spaced $3.6t_v$, $3.6t_v$, $22.7t_v$, $18.0t_v$, and $10.7t_v$ apart. From Assenheimer & Steinberg (1996b).

7. SPIRAL-DEFECT CHAOS

For $\sigma \approx 1$, Morris et al (1993) discovered a spatio-temporally chaotic state in a circular large-aspect-ratio cell with $\Gamma = 78$ while increasing ε above 0.26. This novel state is now referred to as spiral-defect chaos (SDC). A snapshot is shown in Figure 28. SDC is characterized by complex spatio-temporal dynamics involving rotating spirals, targets, dislocations, disclinations, and grain boundaries. The spirals can be right-handed or left-handed, and single-armed or multi-armed, and thus have common features with the giant spirals discussed in Sect. 6.3. This new state is a nice example for the little-understood phenomenon of spatio-temporal chaos (see, for instance, Gollub 1994).

Much recent experimental (see, for instance, Ahlers 1998 and references therein) and theoretical (see, for instance, Cross 1996 and references therein) work has provided convincing evidence that SDC is an intrinsic state of RBC for fluids

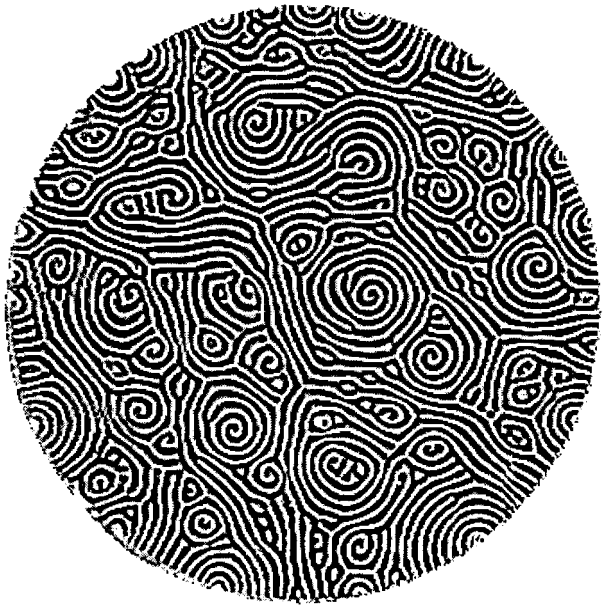

Figure 28 A snapshot of spiral-defect chaos (SDC) in a circular cell of $\Gamma = 78$ at $\varepsilon = 0.72$ and $\sigma = 0.96$. From Morris et al (1993).

with $\sigma \approx 1$. In distinction to the features of the textured patterns discussed in Section 6.4, SDC is not caused or substantially influenced by the sidewalls. It occurs with rectangular (Morris et al 1996) as well as with circular (Morris et al 1993) sidewalls, provided the aspect ratio is not too small. SDC was found numerically in solutions of a generalized Swift-Hohenberg equation (Xi et al 1993) and of the Boussinesq equations (Decker et al 1994, Pesch 1996) (see Section 3).

In their simulations, Decker et al (1994) were able to use an experimental shadowgraph picture from Morris et al (1993) as initial conditions (see Section 3) and to reproduce the experimentally observed dynamics over at least a modest time interval. This is illustrated in Figure 29. The numerical dynamics resemble the experiment quite closely. The small differences may be easily explained by the difference in boundary conditions and the sensitivity of (''chaotic'') SDC to small differences in initial conditions. The code can thus be used to generate reliably the full three-dimensional temperature and velocity fields, which are not accessible with the experimental shadowgraph technique. Of particular interest is the opportunity to determine the mean-flow field (or vertical vorticity), which is important for the dynamics of SDC (Xi et al 1993, Decker et al 1994, Cross 1996) but difficult to determine experimentally, by using the experimental image as the initial condition for a relatively brief numerical integration. Figure 30 shows the strength of the vertical vorticity overlaid onto the convection pattern. The vertical vorticity is clearly localized at high-curvature regions, i.e. at spiral cores, grain boundaries, and dislocations. Apart from numerical simulations, we know of only

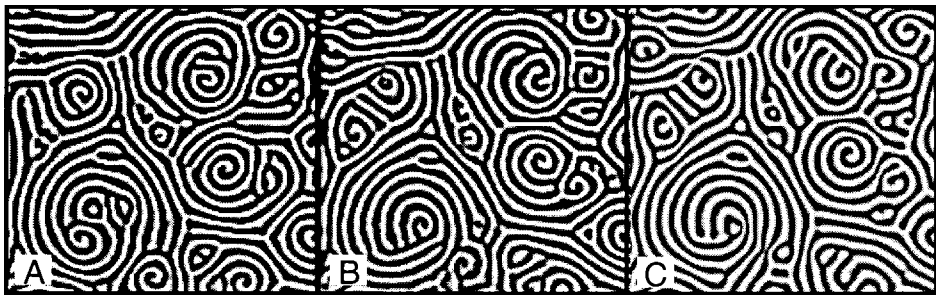

Figure 29 (A) Initial shadowgraph picture of SDC for $\varepsilon = 0.7$ and $\sigma = 1$. (B) Shadowgraph picture, (C) Numerically simulated midplane temperature-field after $20t_v$ (only the central section of the sample is shown). After Decker (1995).

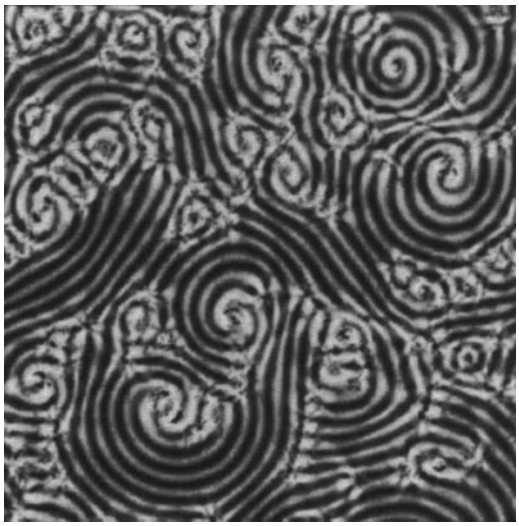

Figure 30 Vertical vorticity field overlaid on top of the convection pattern for $\varepsilon = 0.75$ and $\sigma = 1.1$. Regions of high vorticity appear bright. From simulations by IV Melnikov and W Pesch, unpublished.

one direct experimental visualization of the mean flow. This was done for an off-center target pattern by Croquette et al (1986b) by using a photochromic technique in an experiment with water.

In experiments using compressed SF_6 gas, Assenheimer & Steinberg (1993, 1994) found a transition from SDC to target chaos when σ was increased above approximately 4 by tuning the temperature and pressure near the critical point of the gas. This is consistent with the notion that for larger Prandtl numbers, mean flow effects are weaker. Such transitions have been confirmed in numerical studies (Decker 1995, Cross 1996) but are not understood in detail.

7.1 Onset

The onset value ε_s of SDC decreases as Γ increases. This is shown in Figure 31a. The influence of cell geometry on ε_s appears to be weak. For example, for $\sigma \approx 1$ Hu et al (1995c) and Cakmur et al (1997a) found nearly the same value ε_s for a circular and a square cell with the same $\Gamma \simeq 50$. There seem to be two regimes with different ε_s. For $\Gamma \lesssim 50$ the onset occurs near $\varepsilon_s \simeq 0.6$, whereas for $\Gamma \gtrsim 70$ SDC is found already for $\varepsilon \gtrsim 0.2$. As can be seen in the figure, the transition from one regime to the other occurs over the relatively small Γ-range from 50 to 70. There is no indication that ε_s approaches zero as Γ becomes large, as had been suggested by Li et al (1998). The SDC onset also has an interesting dependence on σ. Using mixtures of gases, it was possible to reach σ-values as small as 0.17 (Liu & Ahlers 1996). Results for two values of Γ are shown in Figure 31b. The data suggest that ε_s remains finite with a value close to 0.1 as σ vanishes.

7.2 Spatio-temporal Evolution of SDC

For circular cells of $\Gamma = 40$ and 78, the mean wavenumbers $\langle q \rangle$ obtained by Fourier analysis of images are shown in Figure 21. Since, at small ε, large- and small-aspect-ratio systems are subject to different wavenumber-selection mechanisms (see Sect. 6.4), the SDC onset is also different. The results suggest that

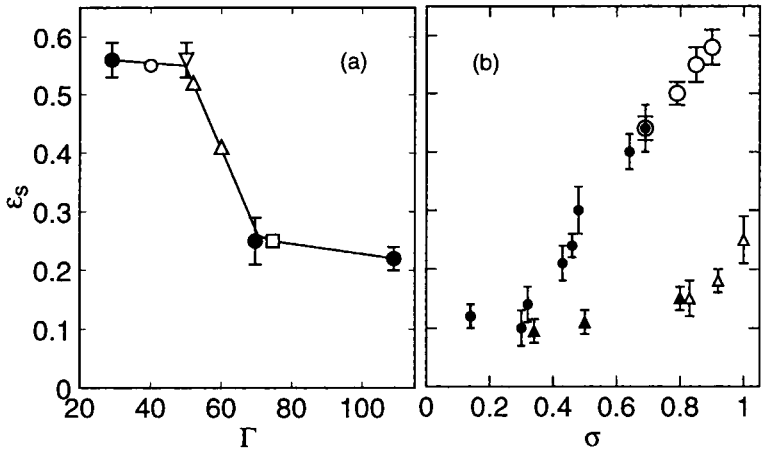

Figure 31 The onset ε_s of SDC as a function of aspect ratio Γ and Prandtl number σ for circular cells (except where noted). (a): $\sigma \simeq 1$; Solid circles: $\Gamma = 29$, 70, and 109 (from J Liu, KMS Bajaj, and G Ahlers, unpublished); open circle: $\Gamma = 40$ (from Ecke & Hu 1997); triangle: $\Gamma = 52$ and 60 (from Hu et al 1995c); square: $\Gamma = 75$ (from Morris et al 1996); upside-down triangle: $\gamma = 50$ for a square cell (from Cakmur et al 1997a). The solid line is a guide to the eye. (b): $\Gamma = 30$ (triangles) and $\Gamma = 70$ (circles). The open circles are for pure gases, and the solid circles are for gas mixtures. After Liu & Ahlers (1996).

there is a separatrix (roughly a straight line through the two large circles in Figure 21) below and to the right of which SDC does not occur. As SDC evolves above that line, it provides its own selection mechanism. Thus the data sets in Figure 21 for the two aspect ratios approach each other, and for $\varepsilon \gtrsim 0.6$ select the same $\langle q \rangle$ in fully developed SDC. The shape of the convection cell is apparently of minor importance because (at least for $\varepsilon \lesssim 1$) almost the same $\langle q \rangle$ is selected in equal-aspect-ratio cells with circular (Hu et al 1995c) and square (Cakmur et al 1997a) geometry.

Time series of shadowgraph images of SDC were analyzed by constructing the three-dimensional structure-factor $S(\mathbf{k}, \omega)$ of the shadowgraph intensity (Morris et al 1996). These data were used to characterize the ε-dependence of the translational correlation length and the correlation time of the chaotic state (Hu et al 1995c, Morris et al 1996). Both were found to decrease approximately as a power law in ε, but a theoretical explanation of this behavior remains to be developed.

An interesting aspect of SDC is the statistics of its time dependence. The number of spirals present at any instance fluctuates. Figure 32 gives the experimentally determined probability $\rho(m)$ of finding m spirals in a given snapshot of the pattern (Ecke et al 1995). It is fit well by a Poisson distribution (solid line). It should be noted that there are no adjustable parameters, since the Poisson distribution is determined completely by the average number of spirals $\langle m \rangle$, which in turn is determined separately from the same set of images. The agreement between the data and the Poisson distribution function is quite good, implying that the birth and death of a particular spiral is not significantly dependent on the presence of the others, i.e. that the spirals to a good approximation may be regarded as ''noninteracting excitations'' of the system (see Landau & Lifshitz 1958).

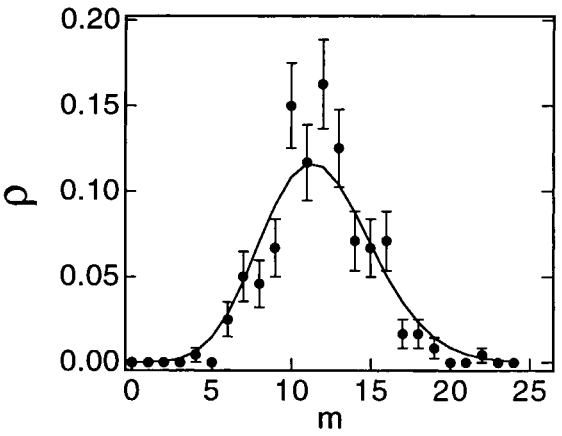

Figure 32 The probability $\rho(m)$ of finding m spirals in a given image for $\varepsilon = 0.96$. The solid line is a Poisson distribution. After Ecke et al (1995).

7.2.1 Coexistence with ideal straight rolls We saw already in Section 5 that SDC is found in a parameter region where (besides targets and giant spirals) ideal straight rolls (ISR) are stable as well. The Busse balloon, giving the stability range of ISR, was shown in Figure 6. That figure included also the wavenumbers corresponding to the maxima of the azimuthal averages of the moduli of the Fourier transforms of SDC images, and these were located deep in the interior of the balloon. Similar data for the mean wavenumber of SDC are found in Figure 21. Images that compare SDC and ISR in the same cells and at the same σ and ε are shown in Figure 5. Additional confirmation of the bistability comes from integrations of the Boussinesq equations with periodic boundary conditions, which always yield SDC from random initial conditions but give stable ISR when ISR-like initial conditions are used (Decker et al 1994). In the experiments, SDC is the generically selected state above ε_s when ε is quasistatically increased from onset (see Liu & Ahlers 1996 and references therein). One concludes that the boundary-induced disorder (foci, dislocations, and grain boundaries) that evolves as ε is increased places the system into the SDC attractor basin before ε_s is reached. Special initial conditions are needed to reach the competing attractors, as discussed in Section 5.

Several quantities have been used to characterize the onset of SDC at ε_s. For circular cells, Hu et al (1995a,c) demonstrated that the global curvature of the patterns (see Figure 20b) suddenly increased at ε_s. Another method consisted of counting the number m of spirals present in many images of a given finite sample and determining where their averages $\langle m \rangle$ vanish as a function of ε (Ecke et al 1995, Liu & Ahlers 1996, Ecke & Hu 1997). The question was addressed also for square cells (Cakmur et al 1997a, Egolf et al 1998). When ε_s was approached from above, the spatio-temporal evolution of SDC was dominated by progressively larger regions of ISR and larger spirals. This was quantified by Egolf et al (1998). Figure 33 shows the experimentally observed, rapid growth of the orientational correlation length ξ_0. Egolf et al (1998) showed that the transition between ISR and SDC occurred as ξ_0 approached the system size in their experiment. They also found ξ_0 to be proportional to a characteristic length ξ_s, which

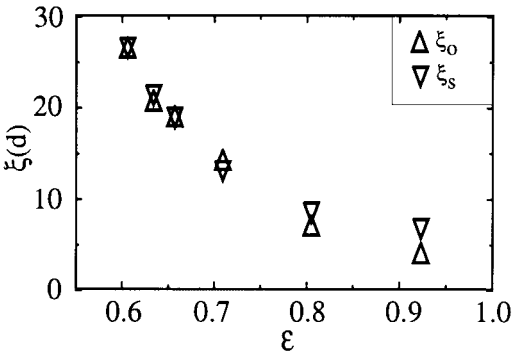

Figure 33 Orientational correlation lengths ξ_0 compared to ξ_s (see text) for $\Gamma = 50$, $\sigma = 1.03$. From Egolf et al (1998).

is a measure of the density n_d of targets and spirals. One finds $\xi_0 \approx \xi_s = \sqrt{n_d^{-1}}/3.5$ (see Figure 33). In addition, the pattern appeared to fluctuate intermittently between a disordered state and almost perfect ISR. This is illustrated in Figure 34. Cakmur et al (1997a) quantified this behavior by using the spectral pattern entropy[22] $S(t) = -\Sigma_{\vec{k}}\, p(\vec{k},t)\, \ln\, p(\vec{k},t)$ (Neufeld & Friedrich 1994, Xi & Gunton 1995), where $p(\vec{k}, t)$ is the spectral distribution function that describes

[22]J Liu, KMS Bajaj, and G Ahlers (unpublished) recently found similar behavior for a circular cell of $\Lambda = 109$. That work was presented at the workshop *Spatiotemporal Characterization of Spiral Defect Chaos* at Los Alamos National Laboratory, January 4–5, 1999.

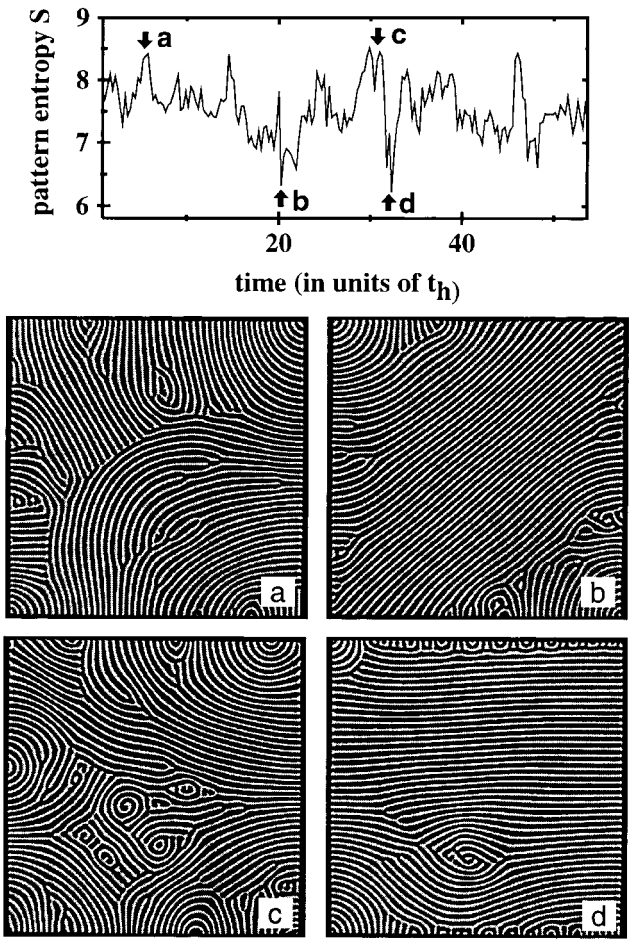

Figure 34 Time evolution of the pattern entropy S and the pattern for $\varepsilon = 0.554$: (a) $14.52t_h$, (b) $20.27t_h$, (c) $30.95t_h$, (d) $32.32t_h$. From Cakmur et al (1997b).

the normalized power in mode $\vec{k}$ at time t. $S(t)$ measures the disorder in the pattern. For example, if the pattern is ideal, i.e. when only a pair of conjugate modes is excited, $S = \ln 2$, and otherwise, $S > \ln 2$.[23] In Figure 34, the time evolution of the pattern entropy is shown for $\varepsilon = 0.554$. The degree of spatial order of the patterns as judged by eye shows a clear correlation with the value of the pattern entropy. Cakmur et al (1997a) observed that the well-ordered patterns during the evolution were typically aligned either diagonal or perpendicular to one of the sidewalls of the square cell; it appeared that the pattern was probing the system's symmetries. In Figure 35A, the temporal average of the pattern entropy $\langle S \rangle_t$ as a function of ε is shown. As the transition to ISR is approached from above, $\langle S \rangle_t$ shows a sharp decrease. Figure 35B shows the standard deviation $\sigma(S)$ over the same range of ε.[24] As ε_s is approached, $\sigma(S)$ displays a sharp increase. It is also possible to measure $\sigma(S)$ below $\varepsilon(S)$ in the fluctuating region of SDC before a strong fluctuation leads to ISR. This is also shown in Figure 35B. For $\varepsilon \gg \varepsilon_s$ the standard deviation $\sigma(S)$ approaches a small value, suggesting that the system consists of many independent, fluctuating subsystems. The behavior shown in Figure 35 appears to be similar to a second-order equilibrium phase transition in a finite-size system, where $\langle S \rangle_t$ would correspond to the internal energy and $\sigma(S)$ to the specific heat. On the other hand, the well-established bistability of SDC and ISR has similarities with a first-order equilibrium phase transition. It is not yet clear whether the comparison to equilibrium phase transitions is justified or even helpful. Other approaches to understanding SDC as a competition between

[23]If only half of the modes in Fourier space are taken, an ideal pattern would have $S = 0$.

[24]The quantity $\sigma(S)$ given by Cakmur et al (1997a) is the standard deviation of S from its mean value, rather than the variance, as stated by the authors.

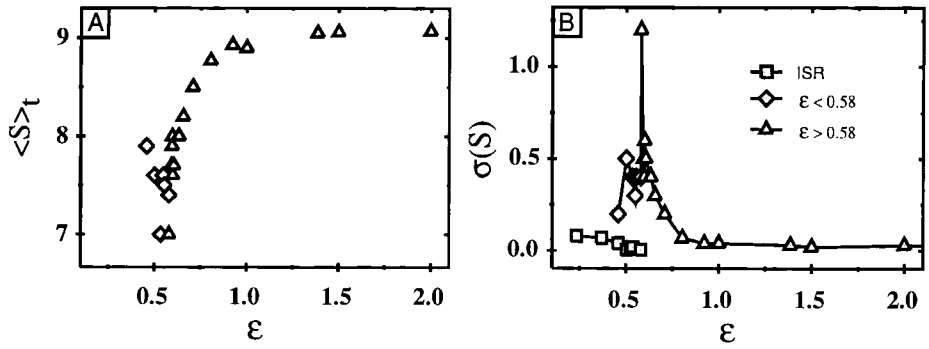

Figure 35 (A) The time-averaged pattern entropy $\langle S \rangle_t$ and (B) the standard deviation $\sigma(S)$ as a function of ε. After Cakmur et al (1997a).

two attractors might be in terms of blowout bifurcations (Ashwin 1998). However, an extension of this theory to spatio-temporal chaotic systems has not been developed.

In another experiment, the spatio-temporal dynamics of SDC were analyzed by a Karhunen-Lóeve decomposition (Zoldi et al 1998). This analysis suggests that the spatio-temporal chaotic properties of SDC are extensive. This is consistent with the ε-independence of $\sigma(S)$ for sufficiently large values of ε (Figure 35B).

When initializing an almost perfect ISR state, Cakmur et al (1997a) observed that SDC can propagate into ISR. This was investigated in more detail for a rectangular cell of aspect ratio 100×50 by Jeanjean (1997) where an ISR state was initialized with the same method as that used by Cakmur et al (1997a). For a fixed value of ε, when the experiment was started with a perfect stripe pattern, SDC nucleated after long times in only one corner of the convection cell. Jeanjean (1997) attributed this to a slight geometrical inhomogeneity. Then SDC grew at the sidewalls by compressing the ISR. After an initial transient, where ISR adjusted their wavenumber toward the SV-instability boundary, SDC started propagating into the ISR state with a flat front. An example of the evolution of SDC propagating into ISR is shown in Figure 36. Local chaotic fluctuations com-

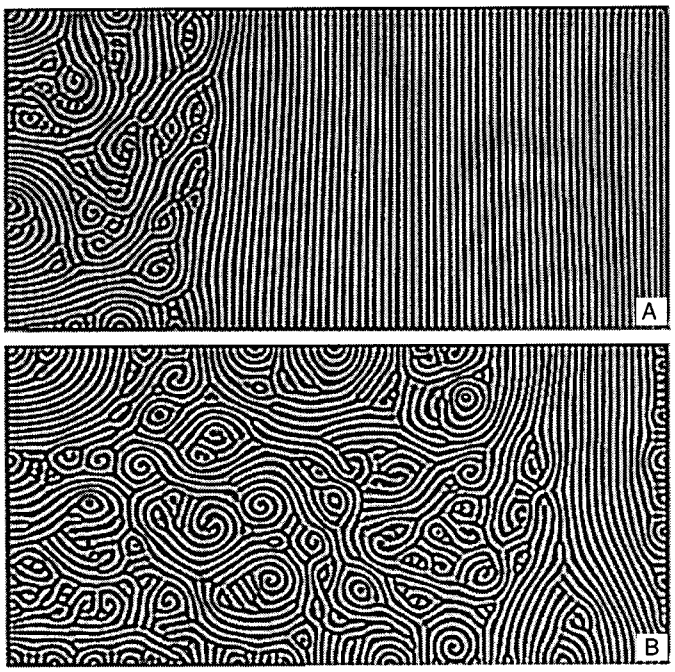

Figure 36 SDC propagates into ISR with a flat front for $\varepsilon = 0.71$. The figures are spaced $\Delta t = 5902 t_v$ apart. In (B), the front is sufficiently close to the opposite sidewall to trigger nucleation of defects. From Jeanjean (1997).

pressed the rolls at the boundary between SDC/ISR, hereby increasing the local wavenumber above the SV-instability boundary. An SV-instability occurred, and as described in Section 5, a dislocation pair nucleated, which then moved toward other dislocations or the boundaries so as to decrease the number of roll pairs. This process continued as SDC gradually replaced the straight rolls. It was found that the front propagated with constant velocity, whose magnitude increased with increasing ε, as shown in Figure 37. Below ε_s, Jeanjean (1997) found a drifting pattern that appeared to be dominated by wall foci. It was suggested that the front speed may be limited by the spatio-temporal dynamics that lead to SV-instabilities (IV Melnikov, DA Egolf, E Bodenschatz, unpublished). However, the understanding of this very interesting property of RBC remains a challenge.

One of the characteristic features of SDC is that its average wavenumbers as determined by Fourier transforms (Morris et al 1993) or by local measurements in physical space (Egolf et al 1998, Bowman & Newell 1998) are in the middle of the stability region for ISR. A small tail of the local wavenumber distribution is above the SV-instability boundary, while only an unnoticeable amount is below the CR-instability boundary (Egolf et al 1998). An example of the wavenumber distribution is shown in Figure 38, which also compares the local wavenumber with the azimuthally averaged power spectrum. Patches with CR-unstable wavenumbers persist only for short periods of time due to the the fast growth rate of the CR-instability and consequently contribute only little to the time-averaged wavenumber distribution. Regions with large q contribute significantly, as the SV-instability is a slow growing instability. It is apparent that the stability boundaries for ISR (Busse balloon) apply locally in a disordered SDC patterns (Egolf et al 1998).

8. ROTATION ABOUT A VERTICAL AXIS

Rotation inhibits the onset of convection and increases the critical wavenumber of the pattern at onset (Chandrasekhar 1961). Figure 39 shows experimental and

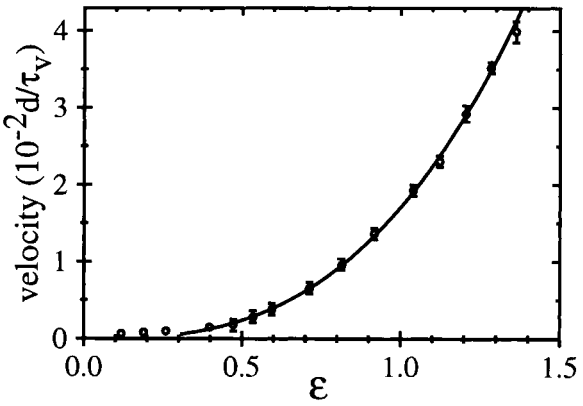

Figure 37 Front propagation velocity v versus ε. The solid line is the fit $v = 1.51(\varepsilon + 0.04)^{2.97}$. From Jeanjean (1997).

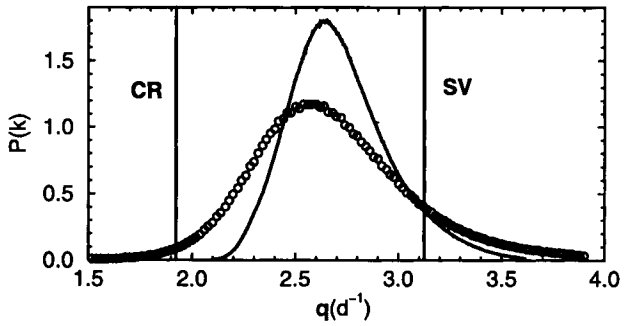

Figure 38 Probability densities of the local wavenumber $|\mathbf{q}(\vec{x})|$ (solid line) and the power spectral density (circles) for $\varepsilon = 0.805$ computed from the central $63d \times 62d$ region of 300 images each separated by $240\tau_v$). Vertical lines denote the lower (cross-roll) and upper (skewed-varicose) stability boundaries. After Egolf et al (1998).

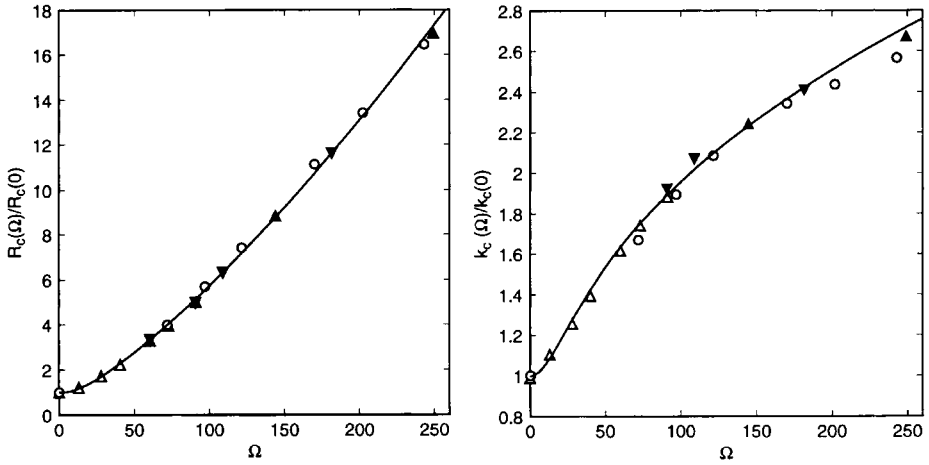

Figure 39 The critical Rayleigh numbers $R_c(\Omega)/R_c(0)$ (*left*) and critical wavenumbers $k_c(\Omega)/k_c(0)$ (*right*) as a function of Ω for water ($\sigma = 5.4$, *open circles*) and argon at 20 bar ($\sigma = 0.68$, *open triangles*), 30 bar ($\sigma = 0.69$ *inverted solid triangles*), and 40 bar ($\sigma = 0.695$, *solid triangles*). The results agree with calculations for a laterally infinite system (*solid lines*). After Bajaj et al (1998).

theoretical results for $R_c(\Omega)$ and $q_c(\Omega)$. We see that, at the linear level, there is excellent agreement between experiment and theory. Both $R_c(\Omega)$ and $q_c(\Omega)$ are predicted to be independent of σ.

As we saw in Section 5, RBC sufficiently close to onset ($\varepsilon \lesssim 0.1$) is relatively simple and, in the absence of boundary forcing, consists of time-independent straight rolls. The system becomes much more complex and interesting even near onset, when it is rotated about a vertical axis $\hat{\mathbf{e}}_z$ with an angular velocity $\Omega \equiv (d^2/\nu)\tilde{\Omega}\hat{z}$ ($\tilde{\Omega}$ is the rotation rate in radian per second and $\hat{z}$ is the unit vector in

the vertical direction). In that case, the Coriolis force proportional to $\Omega\ \hat{\mathbf{e}}_z \times \vec{\mathbf{u}}$ acts on the convecting fluid (here $\vec{\mathbf{u}}$ is the fluid velocity field in the rotating frame) and renders the system nonvariational. Thus time-dependent states can occur arbitrarily close to onset. Over a wide parameter range, the bifurcation remains supercritical for $\Omega > 0$, i.e. the flow amplitudes still grow continuously from zero and the usual weakly nonlinear theories, for instance in the form of Ginzburg-Landau (GL) or SH-equations, should remain applicable. Thus one may expect interesting new effects to occur in a theoretically tractable parameter range.

8.1 Small Rotation Rates

In the range $\Omega \lesssim 10$, a number of interesting, albeit somewhat complicated and as yet incompletely understood, phenomena occur. Although at onset the pattern seems to consist of time-independent rolls, for small ε these rolls become curved and assume an S-shape. As ε increases slightly, formation of defects adjacent to the sidewall, gliding (Millan-Rodriguez et al 1995) and climbing of defects through the cell interior, and the motion of walls between domains of different roll orientation become prevalent. A significant fraction of these dynamics seems to be induced by the sidewalls. We do not discuss these interesting phenomena in detail, but instead refer the reader to the papers by Hu et al (1997, 1998) for recent results and for references to earlier literature.

One noteworthy aspect of moderate rotation rates and somewhat larger $\varepsilon \gtrsim 0.5$ is the influence of the rotation on SDC (Ecke et al 1995). It turns out that for $\Omega = 0$ the average number of right-handed (r) and left-handed (l) spirals is equal. With rotation, this chiral symmetry is broken. A useful order parameter to describe this phenomenon is $M = (m_l - m_r)/(m_l + m_r)$, where m_l and m_r are the average number of left-handed and right-handed spirals, respectively. The parameter M can vary from -1 to 1 and vanishes for $\Omega = 0$. Results for M are shown in Figure 40. It turns out that $M(\Omega)$ can be described well by a hyperbolic tangent

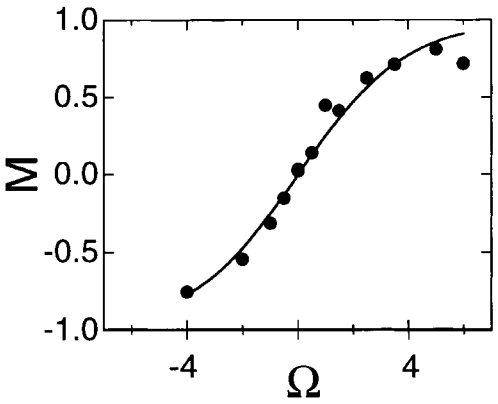

Figure 40 The difference $M = (m_l - m_r)/(m_l + m_r)$ between the average number of left-handed (m_l) and right-handed (m_r) spirals, normalized by the total number ($m_l + m_r$), as a function of the rotation frequency Ω. The solid line is the function $M = tanh(\Omega/\Omega_0)$ with Ω_0 adjusted to fit the data. After Ecke et al (1995).

or by a Langevin function, as shown by the solid line in the figure. This is reminiscent of the magnetization $M(H)$ of a dilute paramagnet as a function of the applied magnetic field H.

8.2 Domain (or Küppers-Lortz) Chaos

For $\Omega > \Omega_c$, the primary bifurcation leads immediately to a state of spatio-temporal chaos in the form of rolls that are unstable (Küppers & Lortz 1969, Küppers 1970, Clever & Busse 1979, Niemela & Donnelly 1986). Ω_c depends on the Prandtl number σ, and it has a value near 14 for the σ-values near unity, which are characteristic of compressed gases. The instability is to plane-wave perturbations, which are advanced relative to the rolls at an angle Θ_{KL} in the direction of Ω. This phenomenon is known as the Küppers-Lortz instability. A snapshot of the resulting nonlinear state of convection is shown in Figure 41 (Hu et al 1995b). The pattern consists of domains of rolls that incessantly replace each other, primarily by irregular domain-wall motion (see e.g. Hu et al 1998 and references therein). The spatial and temporal behavior suggests the term ''domain chaos'' for this state. For $\sigma \gtrsim 0.33$, the primary bifurcation is expected to be supercritical both below and above Ω_c.

Figure 41 An example of the Küppers-Lortz unstable rolls for $\Omega = 15.4$ and CO_2 at a pressure of 32 bar with $\sigma = 1.0$ and $\varepsilon = 0.05$. After Hu et al (1995b).

The opportunity to study STC at onset has led to renewed recent theoretical and experimental interest[25] in the KL-state. For $\sigma \gtrsim 1$ and $\Omega \lesssim 20$, it was demonstrated experimentally with high resolution (Hu et al 1997) that the bifurcation is indeed supercritical and that it leads to continuous domain switching through a mechanism of domain-wall propagation even at small ε (Bodenschatz et al 1992a; Hu et al 1995b, 1997, 1998) This qualitative feature has been reproduced by Tu & Cross (1992b) in numerical solutions of appropriate coupled GL-equations, as well as by Neufeld et al (1993) and Cross et al (1994) through numerical integration of a generalized SH-equation.

Of interest are the time and length scales of the KL-instability near onset. The GL-model assumes implicitly a characteristic time dependence that varies as ε^{-1} and a correlation length that varies as $\varepsilon^{-1/2}$. Measurements of a correlation length given by the inverse width of the square of the modulus of the Fourier transform as well as domain-switching frequencies as revealed in Fourier space yielded the data in Figure 42 (Hu et al 1995b, 1997). These results seem to be inconsistent with GL-equations, because they suggest that the time in the experiment scales approximately as $\varepsilon^{-1/2}$ and that the two-point correlation length scales approxi-

[25]de Bruyn et al (1996), Hu et al (1995b), Zhong et al (1991), Zhong & Ecke (1992), Tu & Cross (1992b), Fantz et al (1992), Neufeld et al (1993), Cross et al (1994), and Ponty et al (1997)

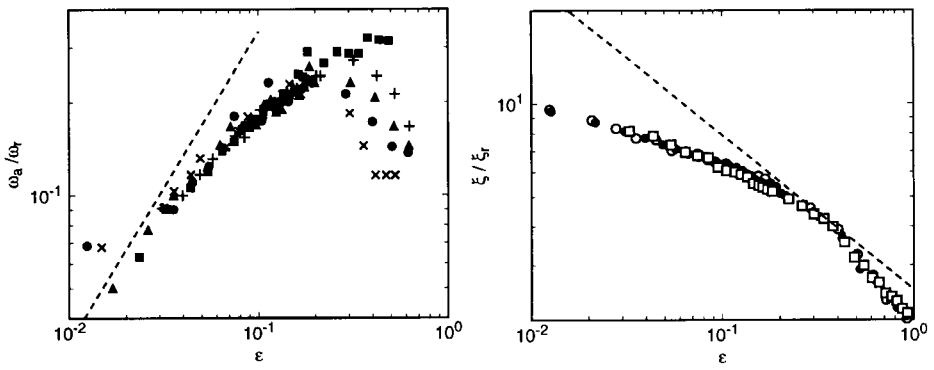

Figure 42 The characteristic domain-switching frequencies ω_a (*left*) and lengths ξ (*right*) of the KL-state. The data were divided by Ω-dependent constants ω_r and ξ_r so as to collapse them onto single curves. The dashed lines are shown for reference and have the slopes 1 for ω_a and $-1/2$ for ξ, which correspond to the theoretically expected exponents of the time and length scales near onset. The data sets cover approximately the range $14 < \Omega < 20$. See Hu et al (1998) for details.

mately as $\varepsilon^{-1/4}$.[26] These results also differ from numerical results based on a generalized SH-equation (Cross et al 1994), although the range of ε in the numerical work is rather limited. The disagreement between experiment and theory is a major problem in our understanding of STC. It is interesting to note that, very recently, Laveder et al (1999) were able to generate numerical solutions of a stochastic SH-model that yield an ε dependence of ξ quite similar to that of the experimental results in Figure 42. However, quite large noise intensities were required in the model, far in excess of any noise source in the experiment. A more likely candidate for an explanation was suggested by Hu et al (1998). As noted by Hu et al (1997) at relatively small Ω, the sidewalls generate defects that travel into the sample interior. Since the defects travel at a constant speed rather than diffusively, they possibly can influence the system interior even when Γ is quite large, as in the experiment. It is conjectured that the defects break up the KL-domains and thus alter the characteristic length- and timescales. It remains to test this hypothesis experimentally as well as by numerical integrations of the Boussinesq or SH-equations with realistic lateral boundary conditions.

8.3 Squares near Onset

Motivated by the unexpected scaling of length and time with ε for the KL-state at $\Omega \lesssim 20$, new investigations were undertaken recently in which the range of Ω was significantly extended to larger values. Contrary to theoretical predictions (Clever & Busse 1979, Clune & Knobloch 1993), it was found (Bajaj et al 1998) that, for $\Omega \gtrsim 70$, the nature of the pattern near onset changed qualitatively although the bifurcation remained supercritical. Square patterns like the one shown in Figure 43 were stable, instead of typical KL-patterns like the one in Figure 41. The squares occurred both when argon with $\sigma = 0.69$ was used (Figure 43a) and when the fluid was water with $\sigma \simeq 5$ (Figure 43b). Subsequently they were found also in numerical integrations of the Boussinesq equations (Figure 43c). Over significant ε-ranges, defects appeared in the square lattice, and for some parameters the lattice was really destroyed; but local fourfold coordination persisted for $\varepsilon \lesssim 0.13$ over the range $70 \lesssim \Omega \lesssim 250$. For larger ε the pattern was more nearly reminiscent of the KL-state. The occurrence of squares at onset in this system is completely unexpected and not predicted by theory; according to the theory (Clever & Busse 1979, Clune & Knobloch 1993), the KL-instability should continue to be found near onset also at these higher values of Ω. Thus we are faced with a major disagreement with theoretical predictions in a parameter range where one might have expected the theory to be reliable. Additional exper-

[26]It was shown by Hu et al (1998) that the data for ξ and ω_a can be fit reasonably well with a powerlaw and the expected theoretical leading exponents if large correction terms are allowed in the analysis; but even then there are significant systematic deviations at small ε, particularly for ξ.

iments and simulations in the range $0 \lesssim \Omega \lesssim 400$ and $0.7 \lesssim \sigma \lesssim 5$ clearly should be carried out.

A further interesting aspect of the square patterns is that the lattice rotates slowly relative to the rotating frame of the apparatus. This was found in the experiments with argon and water as well as in the simulation. Figure 44 gives the angular rotation rate ω (scaled by d^2/ν) of the lattice for the water experiment. The data are consistent with $\omega(\varepsilon)$ vanishing as ε goes to zero. Thus the bifurcation to squares is not a Hopf bifurcation. Presumably, as the aspect ratio of the cell diverges, the slope of $\omega(\varepsilon)$ vanishes because an infinitely extended lattice cannot rotate. Alternatively, of course, the lattice might become unstable as Γ becomes large. It will be interesting to study the Γ dependence of ω experimentally.

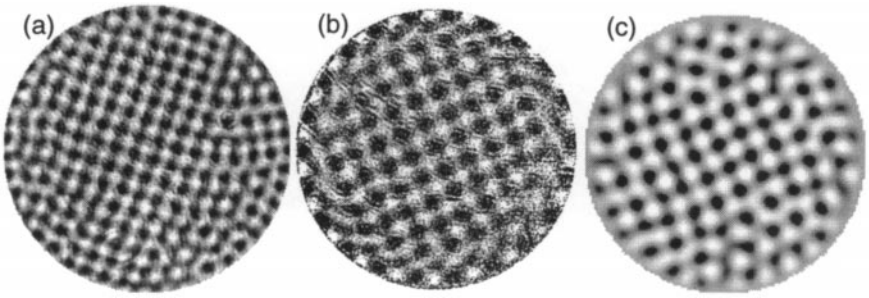

Figure 43 Examples of square patterns near onset. (a) Argon gas with $\sigma = 0.69$ for $\varepsilon = 0.04$ and $\Omega = 145$. (b) Water with $\sigma = 5.4$ for $\varepsilon = 0.09$ and $\Omega = 170$. (c) Numerical integration of the Boussinesq equations (see Section 3.4) for $\sigma = 5.3$, $\varepsilon = 0.06$, and $\Omega = 60$. (a) and (b): Bajaj et al (1998). (c): O Brausch, W Pesch, unpublished.

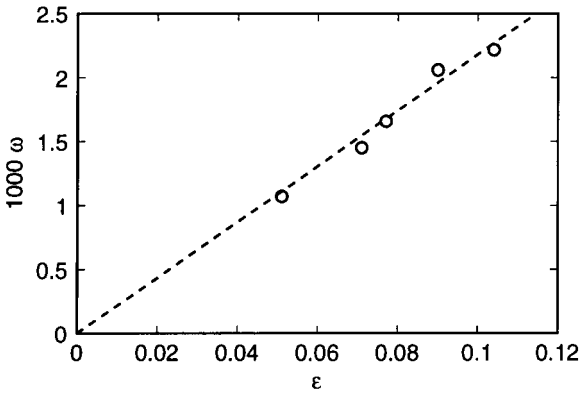

Figure 44 The rotation rate of the square patterns formed with water ($\sigma = 5.4$, $\Omega = 170$) as a function of ε. After Bajaj et al (1998).

9. CONCLUSION AND OUTLOOK

Convection in gases has opened up new vistas and brought a number of advantages for the study of pattern formation. First, the timescales of pattern evolution are typically two orders of magnitude faster than, for instance, those for water. Second, flow visualization by the shadowgraph method has very high sensitivity for these thin layers (see de Bruyn et al 1996). Third, the small thickness has brought us large-aspect-ratio cells that make it possible to study phenomena such as SDC, which do not occur in smaller systems. Fourth, these thin layers are more susceptible to the influence of thermal noise than is the case for classical liquids, thus enabling the quantitative study of noise-induced fluctuations. Fifth, the conductivity of gases usually is very small, and thus it is relatively easy to satisfy the condition (assumed in much of the theoretical work) that the conductivities of the top and bottom plates are much larger than that of the fluid. And finally, the gas mixtures have afforded access to Prandtl numbers as small as 0.16 without inhibiting flow visualization. Because of these unique aspects, there are a number of additional, as yet unexploited, opportunities provided by gas convection, and in this section we mention briefly a few particularly interesting problems that are accessible to experiment.

9.1 RBC with Rotation at Small σ

The rotating RBC system becomes particularly interesting for $\sigma < 1$. Prandtl numbers as small as 0.16 can be reached in mixtures of gases if one component has a molecular weight that is much larger than that of the other (Liu & Ahlers 1997). This is illustrated in Figure 45, which gives $\sigma(x)$ as a function of the mole fraction x of the heavier component for four mixtures. An important question in

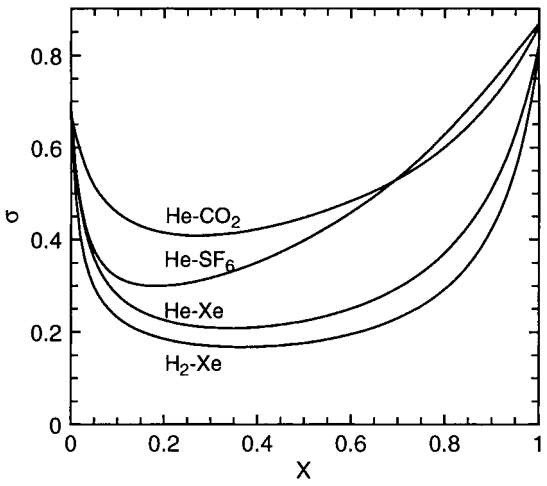

Figure 45 The Prandtl number σ as a function of the mole fraction x of the heavy component for four gas mixtures at a pressure of 22 bar and at 25°C. After Liu & Ahlers (1997).

this relation is whether the mixtures will behave similarly to pure fluids with the same σ. To a good approximation this is expected to be the case, because the Lewis numbers (the ratios of the mass diffusivities to the thermal diffusivities) are of order one. This means that heat diffusion and mass diffusion occur on similar timescales. In that case, the effect of the concentration gradient will be primarily to contribute to the buoyancy force in synchrony with the thermally induced density gradient, and thus for $\Psi > 0$ (Ψ is the separation ratio of the mixture), the critical Rayleigh number will be reduced. Scaling bifurcation lines by $R_c(\Psi)$ will mostly account for the mixture effect. To some extent this was shown already by experiment (Liu & Ahlers 1996, 1997). Recent additional measurements (KMS Bajaj, W Pesch, and G Ahlers, unpublished) demonstrated that the bifurcation line $R_c(\Psi, \Omega)/R_c(\Psi, 0)$ and critical wavenumber $q_c(\Psi, \Omega)/q_c(\Psi, 0)$ are within experimental resolution independent of Ψ. In addition, linear stability analyses for these mixtures (KMS Bajaj, W Pesch, and G Ahlers, unpublished) also showed that these ratios are only very weakly dependent on Ψ.

For $\sigma > 0.33$, the primary bifurcation at easily accessible rotation rates is predicted to be stationary and supercritical. At very large Ω and for $\sigma < 0.68$ it is predicted to be preceded by a supercritical Hopf bifurcation (Clune & Knobloch 1993). In the stationary case, one always expects KL-chaos. As discussed above in Section 8.3, experiments do not agree with this; $\Omega \gtrsim 70$ square patterns, which are clearly unrelated to the typical KL-domains, appear near onset. The range $0.16 \lesssim \sigma \lesssim 0.33$ is truly remarkable because of the richness of the bifurcation phenomena that occur there when the system is rotated. For instance, for $\sigma = 0.26$ there is a range from $\Omega \simeq 16$ to 190 over which the bifurcation is predicted to be subcritical. This is shown by the dashed section of the curve in Figure 46B. The subcritical range depends on σ. In Figure 46A it covers the area below the dashed curve. Thus, the dashed curve is a line of tricritical bifurcations.[27] It has a maximum in the $\Omega - \sigma$ plane. An analysis of the bifurcation phenomena, which occur near it in terms of Landau equations, may turn out to be interesting. One may expect path-renormalization (Fisher 1968) of the classical exponents in the vicinity of the maximum. We are not aware of equivalent phenomena in equilibrium phase transitions, although presumably they exist in as-yet-unexplored parameter ranges. The Hopf bifurcation that precedes the stationary bifurcation at relatively large Ω is predicted to be supercritical and to lead to standing waves of convection rolls (Clune & Knobloch 1993). Standing waves are relatively rare; usually a Hopf bifurcation in a spatially extended system leads to traveling waves. The bifurcation lines for $\sigma = 0.26$ are shown in Figure 46B. As can be seen

[27]Early theoretical evidence for the existence of a subcritical and tricritical bifurcation is contained in the work of Clever & Busse (1979). More recent calculations of the tricritical line by Clune & Knobloch (1993) are inconsistent with the result of Clever & Busse (1979). A new calculation (KMS Bajaj, W Pesch, G Ahlers, unpublished) of the tricritical line yielded the results shown in Figure 46, which are more detailed than, but agree with, those of Clever & Busse (1979).

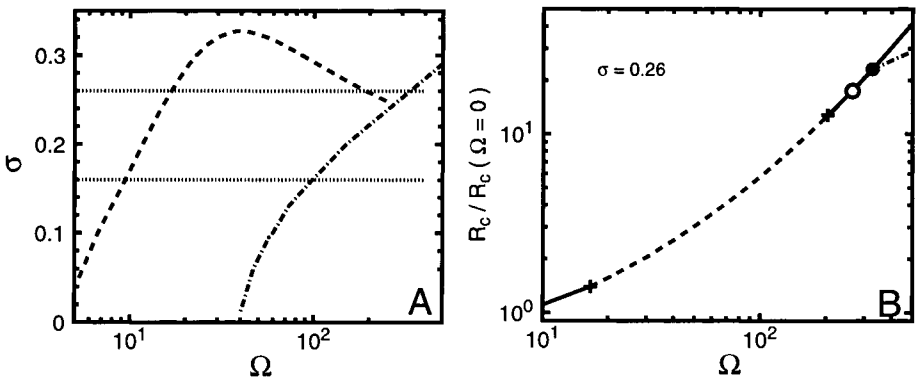

Figure 46 The theoretically predicted bifurcation diagram for RBC with rotation about a vertical axis. (A) The dashed curve gives the tricritical line. The dash-dotted line is the codimension-two line where the Hopf bifurcation meets the stationary bifurcation, e.g. the solid circle in B. For $\sigma = 0.24$ the codimension-two line intersects the tricritical line, leading to the codimension-three point shown by the open circle in B. The upper dotted line in A corresponds to the path represented in B. The lower dotted line in A represents the lowest σ-value accessible to experiment using gas mixtures. (B) Bifurcation lines for $\sigma = 0.26$. The dashed line shows the range over which the stationary bifurcation is subcritical. The two plusses are the tricritical points. The dash-dotted line at large Ω shows the Hopf bifurcation. (From KMS Bajaj, W Pesch, G Ahlers, unpublished.)

there, the Hopf bifurcation terminates at small Ω at a codimension-two point on the stationary bifurcation, which, depending on σ, can be super- or subcritical. The line of codimension-two points is shown in Figure 46A as a dash-dotted line. One sees that the tricritical line and the codimension-two line meet at a codimension-three point, located at $\Omega \simeq 270$ and $\sigma \simeq 0.24$. We note that this is well within the parameter range accessible to experiments with gas mixtures. We are not aware of any other experimentally accessible examples of codimension-three points. This particular case should be accessible to analysis by weakly nonlinear theories, and a theoretical description in terms of Ginzburg-Landau equations would be extremely interesting and could be compared with experimental measurements.

9.2 RBC with Inclination

Another interesting variation of traditional RBC is convection in a fluid layer that is inclined relative to gravity. Then, as a function of Prandtl number and inclination angle, not only buoyancy-driven but also shear-flow–driven instabilities occur. As in RBC with rotation, the system is particularly rich in the Prandtl-number range accessible in experiments with compressed gases.

A summary of the pertinent literature can be found in the papers by Busse & Clever (1992) and Kelly (1994). In contrast to usual RBC, the basic state consists

of heat conduction and a parallel shear flow with cubic velocity profile. A schematic plot is given in Figure 47. The shear flow breaks the in-plane isotropy of the usual RBC. In this sense the system is similar to convection in liquid crystals with planar alignment of the director (see, for instance, Kramer & Pesch 1995). For angles smaller than 90° the fluid is heated from below, and both buoyancy and shear are destabilizing, whereas for angles above 90° the fluid layer is heated from above, where buoyancy is stabilizing and shear is destabilizing.

Linear stability analysis of the basic state is discussed in the papers by Fujimura & Kelly (1993a,b) and Chen & Pearlstein (1989). Depending on the inclination angle γ and on σ, longitudinal, oblique, transverse, and traveling transverse rolls are the possible flow structures at onset. The most common pattern for $\gamma < 90°$ and $\sigma > 0.6$ is longitudinal rolls with their axes aligned with the shear flow ($\mathbf{q} = (\alpha, 0)$). This situation is analogous to Rayleigh-Bénard convection with Poiseuille flow, for which longitudinal rolls is the preferred state (see e.g. Fujimura & Kelly 1995). The onset of longitudinal rolls is independent of σ. As shown by Kurzweg (1970) for the linearized equations and later by Clever (1973) in the nonlinear case, longitudinal rolls can be described by a suitable rescaling of any two-dimensional solution of the horizontal Rayleigh-Bénard problem. The instability of the ground state with respect to longitudinal rolls is at the critical Rayleigh number $R_c^L = R_c/\cos\gamma$ and the critical wavenumber $\alpha_c^L = \alpha_c$, where $R_c = 1708$ and $\alpha_c = 3.117$ are the critical Rayleigh and wavenumbers of horizontal RBC. The analysis of Gershuni & Zhukhovitskii (1969) showed that oblique rolls with $\mathbf{q} = (\alpha, \beta)$ always have a higher threshold compared with longitudinal rolls. The critical Rayleigh numbers of the other solutions are not so easy to obtain, and a detailed discussion is given by Fujimura & Kelly (1993a). For Prandtl numbers $0 < \sigma < 0.26$, transverse rolls with $\mathbf{q} = (0, \beta)$ (roll axes transverse to the shear flow) are realized for all angles of inclination. For $\sigma > 0.26$ and $0° < \gamma < \gamma_c$, longitudinal rolls are the linear perturbations that goes unstable first. For $0.26 < \sigma < 12.42$ and $\gamma > \gamma_c$, transverse rolls have a lower threshold. For $\sigma > 12.42$, traveling transverse rolls are realized at onset for angles close to 90°. The codimension-two point, at γ_c, where transverse rolls and longitudinal rolls bifurcate at the same threshold, can be understood in the

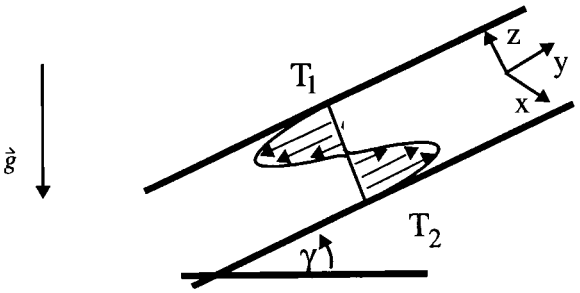

Figure 47 Sketch of the geometrical configuration and the shear-flow velocity profile.

context of a competition of the two different physical instability mechanisms: the thermal, leading to longitudinal rolls, and the hydrodynamic (shear-flow), leading to transverse rolls. With increasing σ, the codimension-two point moves quickly to angles close to 90°. Above 90° the fluid layer is heated from above and the instabilities are driven by shear flow. In Figure 48 the stability diagram of the basic state is plotted for three different Prandtl numbers. Also shown in Figure 48 is the experimentally measured onset for pressurized CO_2 gas with $\sigma = 1.06$. The theoretical predictions agree well with the experimental values. However, above γ_c, traveling transverse rolls were observed in the experiment although the theory predicts stationary transverse rolls. Perhaps this discrepancy can be attributed to NOB effects; but only further investigations will settle this issue. Meanwhile, the results of Daniels et al (1999) are the first experimental confirmation of the theoretically predicted onset values for angles from 0° to 120°.

The nonlinear regime and the possible flow structures have been studied theoretically in two- and three-dimensional simulations by Clever & Busse (1977), Busse & Clever (1992), and with semi-analytical methods by Auer (1993) and Fujimura & Kelly (1993a,b). The analysis by Fujimura & Kelly (1993a,b) focuses on the interesting region at the codimension-two point where both longitudinal and transverse rolls bifurcate at onset. They predict a bimodal state that was found recently (KE Daniels and E Bodenschatz, unpublished). Clever & Busse (1977), Busse & Clever (1992), and Auer (1993) investigated the nonlinear regime in the region where longitudinal rolls appear at threshold. One of their predictions is that for a convecting gas with $\sigma \approx 1$, longitudinal rolls should be unstable to a pattern of stationary undulations.

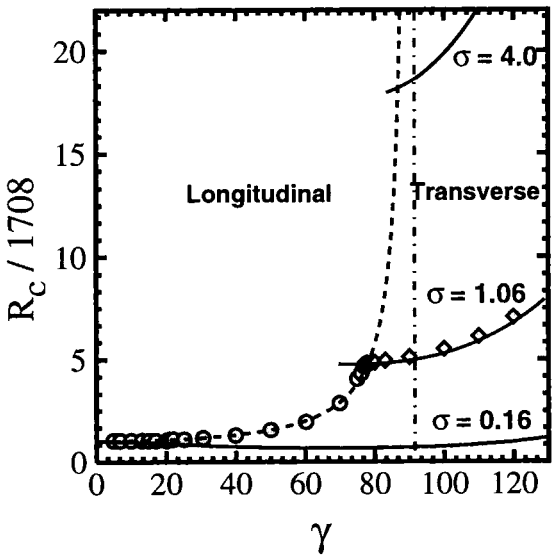

Figure 48 Stability diagram of the basic flow as a function of inclination angle γ for different Prandtl numbers for longitudinal rolls (dashed) and transverse rolls (solid). To the left of the dash-dotted line at 90°, the convection cell is heated from above, whereas to the right it is heated from below. Also shown are experimental data for $\sigma = 1.06$ in a cell with an aspect ratio of 21×42. From Daniels et al (1999).

Previous experimental investigations of convection in inclined layers are summarized by Shadid & Goldstein (1990). The experiments were performed in rectangular cells with the largest aspect ratio being 20×40. In most cases the heat flux across the layer was measured. In the experiments by Hart (1971a,b), Ruth et al (1980), and Ruth (1980), the fluid flow was visualized by introducing tracer particles into it. When the fluid was air, smoke was used; and for water, ground fish scales were employed. As a compromise to allow visualization, one of the well-conducting boundaries (metal top plate) was replaced with a transparent but poorly conducting plate [glass or PMMA (plexiglass)]. The results should be considered as only qualitative, because it is well known from convection in a horizontal layer that, in the case of asymmetric boundaries, the bifurcation diagram near onset is considerably modified (see e.g. Busse 1989). In the recent experiment by Shadid & Goldstein (1990), symmetric boundaries with low heat conduction were used. A liquid-crystal sheet on the cell bottom and a glass top-plate were used for visualization of the temperature field. As explained and observed by the authors, insulating top and bottom boundaries lead to rectangular patterns at the onset of convection. This situation is again different from that addressed in the theoretical calculations. Experiments and numerical simulations by Kirchartz & Oertel (1988) address the problem of convection in an inclined rectangular box of aspect ratio 1:4:10 and 1:2:4. They visualized the flow by optical interference techniques from the side. They showed that the flow in these very confined geometries is strongly influenced by the sidewalls. Again, close to onset the theoretical results discussed before are not applicable to this situation.

In summary, all experiments so far have been limited by the small aspect ratios of the cells, the unequal or weakly conducting cell boundaries, the methods of flow visualization, or the ε-resolution of the experiments. In the linear regime, good qualitative agreement for the onset of longitudinal and transverse rolls was found. In the nonlinear regime, the transitions to wavy rolls was confirmed qualitatively. However, the experiments gave results that can be compared only semi-quantitatively to the recent theoretical predictions by Clever & Busse (1977), Busse & Clever (1992), Auer (1993), and Fujimura & Kelly (1993a,b).

By using compressed gases as a convecting fluid, it is now possible to explore inclined RBC for a wide range of Prandtl numbers in large-aspect-ratio systems. For example, Daniels et al (1999) investigated the phase diagram for $\sigma \approx 1$ and found a variety of novel instabilities that are still under investigation. One important discovery is that the instability of longitudinal rolls is not to stationary undulations, as predicted by Clever & Busse (1977), but to spatio-temporal chaos. New numerical simulations on the basis of Section 3.4 by Daniels et al (1999) also found this spatio-temporal chaotic state. Daniels et al (1999) were also able to visualize the convective patterns when the experiment was heated from above. An example is shown for $\gamma = 120^\circ$ in Figure 49 where the flow is purely shear driven.

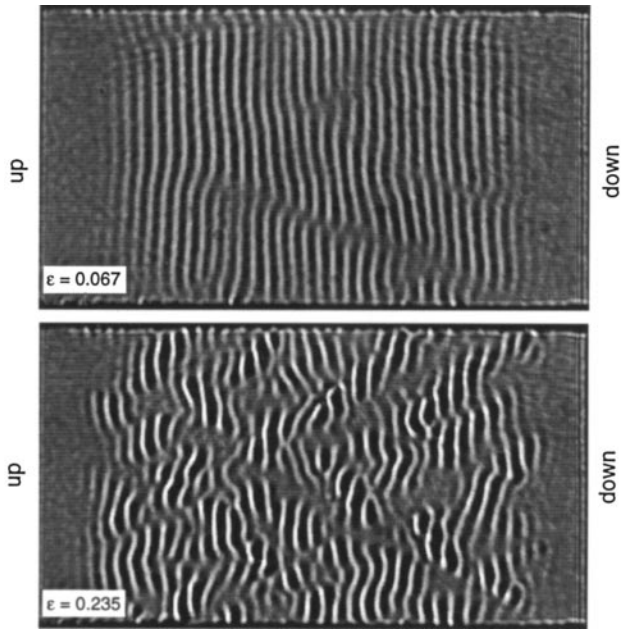

Figure 49 Snapshot of the convective pattern for $\gamma = 120°$, $\sigma = 1.06$, in a cell of aspect-ratio 21×42. The higher (lower) end of the inclined cell is marked with up (down). From KE Daniels and E Bodenschatz, unpublished.

9.3 RBC with Modulation of the Vertical Acceleration

The response of hydrodynamic systems to periodic modulation of the driving has been of considerable interest since the seminal experiments of Donnelly et al (1962). The case of modulated RBC has received much theoretical attention (Ahlers et al 1985b).[28] Either the vertical acceleration or the temperature difference can be modulated with a frequency ω. The consequences are somewhat different for two reasons. First, the acceleration affects the momentum-balance equation, whereas the temperature enters into the heat equation. Second, gravity modulation (a body force) does not change the symmetry of the conduction state, whereas temperature modulation (when applied to the top or bottom plate) induces a nonlinear conduction profile and thus leads to a transcritical bifurcation and hexagonal patterns (Meyer et al 1988, 1992). In either case, the simplest modulation would take the form $\varepsilon(t) = \varepsilon_0 + \delta sin(\omega t)$, with ω and t scaled by the vertical thermal diffusion time $\tau_v = d^2/\kappa$. Among the expected effects are a shift in the threshold, a subharmonic bifurcation over certain ranges of δ and ω, and changes in the nonlinear properties such as the Nusselt number and the patterns above onset. Experiments using thermal modulation (Meyer et al 1988, 1992) have been difficult and confined to rather restricted regions of the $\omega - \delta$ parameter space. The interesting region of large δ was difficult to reach because of the

[28]A review of early work is given by Davis (1967).

large thermal mass of the bottom plate of the convection cell. Gravity modulation seemed even less promising with conventional convection systems employing water as the fluid, because τ_v is of the order of 10^2 seconds and, with δ of any significant size and ω small enough to produce interesting effects unrealistic periodic vertical displacements.

Convection in gases has much to offer in this area. The fluid layers are much thinner, with thermal diffusion times two orders of magnitude smaller than in water (i.e. near 1). Consequently, the desired vertical displacements are realistically achievable in these systems. In addition, the Prandtl number is near one, where modulation effects are maximal. We are pleased to see that work on this interesting problem is now under way (Rogers et al 1998).

ACKNOWLEDGMENTS

EB acknowledges support from the National Science Foundation (DMR-9320124, ASC-950243, and DMR-9705410). EB and WP acknowledge support by NATO (CRG-950243). W.P. also acknowledges support from the Deutsche Forschungsgemeinschaft (Bu 589/9-1). GA acknowledges support from the US Department of Energy (DE-FG03-87ER13738) and the National Science Foundation (DMR94-19168).

LITERATURE CITED

Ahlers G. 1998. Experiments on spatio-temporal chaos. *Physica A* 249(1–4):18–26

Ahlers G, Cannell DS, Steinberg V. 1985a. Time dependence of flow patterns near the convective threshold in a cylindrical container. *Phys. Rev. Lett.* 54(13):1373–76

Ahlers G, Cross MC, Hohenberg PC, Safran S. 1981. The amplitude equation near the convective threshold: application to time-dependent heating experiments. *J. Fluid Mech.* 110:297

Ahlers G, Hohenberg PC, Lücke M. 1984. Externally modulated Rayleigh-Bénard convection: experiment and theory. *Phys. Rev. Lett.* 53(1):48–51

Ahlers G, Hohenberg PC, Lücke M. 1985b. Thermal convection under external modulation of the driving force. I. the Lorenz model. *Phys. Rev. A* 32(6):3493–518

Aranson I, Assenheimer M, Steinberg V, Tsimring LS. 1997. Large-scale flow and spiral core instability in Rayleigh-Bénard convection. *Phys. Rev. E* 55(5):R4877–80

Ashwin P. 1998. *Chaotic intermittency of patterns in symmetric systems. Tech. Rep. 98/29*, Guildford, UK: Cent. Interdiscip. Nonlinear Math. Univ. Surrey

Assenheimer M. 1994. *Rayleigh-Bénard convection in the vicinity of the thermodynamical critical point.* PhD thesis. Weizmann Inst. Sci., Rehovot, Israel

Assenheimer M, Steinberg V. 1993. Rayleigh-Bénard convection near the gas-liquid critical point. *Phys. Rev. Lett.* 70(25):3888–91

Assenheimer M, Steinberg V. 1994. Transition between spiral and target states in Rayleigh-Bénard convection. *Nature* 367(6461):345–47

Assenheimer M, Steinberg V. 1996*b*. Observation of coexisting upflow and down-flow hexagons in Boussinesq Rayleigh-Bénard convection. *Phys. Rev. Lett.* 76(5):756–59

Auer M. 1993. *Dreidimensionale Konvektionsströmungen in ebenen Schichten und im Spalt zwischen rotierenden Zylindern: schwach nichtlineare Untersuchungen in der Nähe multipler Verzweigungspunkte.* PhD thesis. Univ. Bayreuth, Germany

Auer M, Busse FH, Clever RM. 1995. Three-dimensional convection driven by centrifugal buoyancy. *J. Fluid Mech.* 301:371–82

Babcock KL, Ahlers G, Cannell DS. 1994. Noise amplification in open Taylor-Couette flow. *Phys. Rev. E* 50(5):3670–92

Bajaj KMS, Cannell DS, Ahlers G. 1997. Competition between spiral-defect chaos and rolls in Rayleigh-Bénard convection. *Phys. Rev. E* 55(5):R4869–72

Bajaj KMS, Jun L, Naberhuis B, Ahlers G. 1998. Square patterns in Rayleigh-Bénard convection with rotation about a vertical axis. *Phys. Rev. Lett.* 81(4):806–9

Berry MV, Bodenschatz E. 1999. Caustics, multiply reconstructed by Talbot interference. *J. Mod. Opt.* 46(2):349–65

Bestehorn M, Fantz M, Friedrich R, Haken H, Perez-Garcia C. 1992. Spiral patterns in thermal convection. *Z. Phys. B* 88(1):93–94

Bodenschatz E, Cannell DS, de Bruyn JR, Ecke R, Hu Y, et al. 1992a. Experiments on three systems with nonvariational aspects. *Physica D* 61(1–4):77–93

Bodenschatz E, de Bruyn JR, Ahlers G, Cannell DS. 1991. Transitions between patterns in thermal convection. *Phys. Rev. Lett.* 67(22):3078–81

Bodenschatz E, Morris SW, de Bruyn JR, Cannell DS, Ahlers G. 1993. Gallery of fluid motion. *Phys. Fluids A* 5(9):S1–11

Bodenschatz E, Morris SW, de Bruyn JR, Cannell DS, Ahlers G. et al. 1992b. Convection in gases at elevated pressures. *Proc. KIT Int. Workshop Phys. Pattern Formation in Complex Dissipative Systems*, ed. S Kai, pp. 227–37. Singapore: World Scientific

Bowman C, Ercolani N, Indik R, Newell AC, Passot T. 1998. Patterns, defects and integrability. *Physica D* 123(1–4):474–92

Bowman C, Newell AC. 1998. Natural patterns and wavelets. *Rev. Mod. Phys.* 70(1):289–301

Brazovskii SA. 1975. Phase transition of an isotropic system to an inhomogeneous state. *Zh. Eksp. Teor. Fiz.* 68(1):175–85

Brown SN, Stewartson K. 1978. On finite amplitude Bénard convection in a cylindrical container. *Proc. R. Soc. London* 360(1703):455–69

Buell JC, Catton I. 1986a. Wavenumber selection in large-amplitude axisymmetric convection. *Phys. Fluids* 29(1):23–30

Buell JC, Catton I. 1986b. Wavenumber selection in ramped Rayleigh-Bénard convection. *J. Fluid Mech.* 171:477–94

Busse FH. 1967. The stability of finite amplitude cellular convection and its relation to an extremum principle. *J. Fluid Mech.* 30:625–49

Busse FH. 1972. The oscillatory instability of convection rolls in a low Prandtl number fluid. *J. Fluid Mech.* 52:97–112

Busse FH. 1978. Non-linear properties of thermal convection. *Rep. Prog. Phys.* 41:1929–67

Busse FH. 1989. Fundamentals of thermal convection. In *Mantle Convection: Plate Tectonics and Global Dynamics*, ed. WR Peltier, pp. 23–95. Montreux: Gordon and Breach

Busse FH, Clever RM. 1992. Three-dimensional convection in an inclined layer heated from below. *J. Eng. Math.* 26(1):1–19

Busse FH, Clever RM. 1998. Mechanism of the onset of time-dependence in thermal convection. In *Time-Dependent Nonlinear Convection*, ed. PA Tyvand, pp. 1–50. Southampton, UK: Comput. Mech. Pub.

Busse FH, Hartung G, Jaletzky M, Sommermann G. 1998. Experiments on thermal convection in rotating systems motivated by planetary problems. *Dyn. Atmos. Oceans* 27(1–4):161–74

Busse FH, Kropp M, Zaks M. 1992. Spatio-temporal structures in phase-turbulent convection. *Physica D* 61(1–4):94–105

Busse FH, Whitehead JA. 1971. Instabilities of convection rolls in a high Prandtl number fluid. *J. Fluid Mech.* 47:305–20

Cakmur RV, Egolf DA, Plapp BB, Bodenschatz E. 1997a. Bistability and competition of spatiotemporal chaotic and fixed point attractors in Rayleigh-Bénard convection. *Phys. Rev. Lett.* 79(10):1853–56

Cakmur RV, Egolf DA, Plapp BB, Bodenschatz E. 1997b. Transition from spatiotemporal chaos to ideal straight rolls in Rayleigh-Bénard convection. *http://xxx.lanl.gov/abs/patt-sol/* 9702003:1–4

Chandrasekhar S. 1961. *Hydrodynamic and Hydromagnetic Stability.* Oxford, UK: Oxford Univ. Press

Chen Y, Pearlstein AJ. 1989. Stability of free-convection flows of variable-viscosity fluids in vertical and inclined slots. *J. Fluid Mech.* 198:513–41

Ciliberto S, Coullet P, Lega J, Pampaloni E, Perez-Garcia C. 1990. Defects in roll-hexagon competition. *Phys. Rev. Lett.* 65(19):2370–73

Ciliberto S, Pampaloni E, Perez-Garcia C. 1988. Competition between different symmetries in convective patterns. *Phys. Rev. Lett.* 61(10):1198–201

Ciliberto S, Pampaloni E, Perez-Garcia C. 1991. The role of defects in the transition between different symmetries in convective patterns. *J. Stat. Phys.* 64(5–6):1045–58

Clever RM. 1973. Finite amplitude longitudinal convection rolls in an inclined layer. *Trans. ASME C* 95(3):407–8

Clever RM, Busse FH. 1974. Transition to time-dependent convection. *J. Fluid Mech.* 65:625–45

Clever RM, Busse FH. 1977. Instabilities of longitudinal convection rolls in an inclined layer. *J. Fluid Mech.* 81:107–25

Clever RM, Busse FH. 1979. Nonlinear properties of convection rolls in a horizontal layer rotating about a vertical axis. *J. Fluid Mech.* 94:609–27

Clever RM, Busse FH. 1996. Hexagonal convection cells under conditions of vertical symmetry. *Phys. Rev. E* 53(3):R2037–40

Clune T, Knobloch E. 1993. Pattern selection in rotating convection with experimental boundary conditions. *Phys. Rev. E* 47(4):2536–50

Croquette V. 1989a. Convective pattern dynamics at low Prandtl number: Part I. *Contemp. Phys.* 30(2):113–33

Croquette V. 1989b. Convective pattern dynamics at low Prandtl number: Part II. *Contemp. Phys.* 30(3):153–71

Croquette V, Le Gal P, Pocheau A. 1986a. Spatial features of the transition to chaos in an extended system. *Phys. Scr.* T13:135–38

Croquette V, Le Gal P, Pocheau A, Guglielmetti R. 1986b. Large-scale flow characterization in a Rayleigh-Bénard convective pattern. *Europhys. Lett.* 1(8):393–99

Croquette V, Mory M, Schosseler F. 1983. Rayleigh-Bénard convective structures in a cylindrical container. *J. Phys.* 44(3):293–301

Croquette V, Pocheau A. 1984. Wavenumber selection in Rayleigh-Bénard convective structure. In *Cellular Structures in Instabilities*, ed. JE Wesfreid, S Zaleski, pp. 104–26. Berlin: Springer-Verlag Vol. 210 of *Lecture Notes in Physics*

Croquette V, Williams H. 1989a. Nonlinear competition between waves on convective rolls. *Phys. Rev. A* 39(5):2765–68

Croquette V, Williams H. 1989b. Nonlinear waves of the oscillatory instability on finite convective rolls. *Physica D* 37(1–3):300–14

Cross M. 1996. Theoretical modelling of spiral chaos in Rayleigh-Bénard convection. *Physica D* 97(1–3):65–80

Cross MC. 1982. Ingredients of a theory of convective textures close to onset. *Phys. Rev. A* 25(2):1065–76

Cross MC. 1983. Phase dynamics of convective rolls. *Phys. Rev. A* 27(1):490–98

Cross MC, Hohenberg PC. 1993. Pattern formation out of equilibrium. *Rev. Mod. Phys.* 65(3):851–1112

Cross MC, Hohenberg PC. 1994. Spatiotemporal chaos. *Science* 263(5153):1569–70

Cross MC, Hohenberg PC, Lücke M. 1983. Forcing of convection due to time-dependent heating near threshold. *J. Fluid Mech.* 136:269–76

Cross MC, Meiron D, Tu Y. 1994. Chaotic domains: a numerical investigation. *Chaos* 4(4):607–19

Cross MC, Tu Y. 1995. Defect dynamics for spiral chaos in Rayleigh-Bénard convection. *Phys. Rev. Lett.* 75(5):834–37

Daniels KE, Bodenschatz E, Pesch W, Brausch O. 1999. Pattern formation in inclined layer convection. *Bull. Am. Phys. Soc.* CENT99:QC28.01

Daviaud F, Pocheau A. 1989. Inhibition of phase turbulence close to onset of convection by permeable lateral boundary condition for the mean flow. *Europhys. Lett.* 9(7):675–80

Davis SH. 1967. Convection in a box: linear theory. *J. Fluid Mech.* 30:465–78

de Bruyn JR, Bodenschatz E, Morris SW, Trainoff SP, Hu Y, et al. 1996. Apparatus for the study of Rayleigh-Bénard convection in gases under pressure. *Rev. Sci. Inst.* 67(6):2043–67

Decker W. 1995. *Mathematische Methoden zur Beschreibung strukturbildender Systeme—eine kritische Analyse.* PhD thesis. Univ. Bayreuth, Germany

Decker W, Pesch W. 1994. Order parameter and amplitude equations for the Rayleigh-Bénard convection. *J. Phys.* 4(3):419–38

Decker W, Pesch W, Weber A. 1994. Spiral defect chaos in Rayleigh-Bénard convection. *Phys. Rev. Lett.* 73(5):648–51

Donnelly RJ, Reif F, Suhl H. 1962. Enhancement of hydrodynamic stability by modulation. *Phys. Rev. Lett.* 9(9):363–65

Ecke RE, Hu Y. 1997. Spiral defect chaos in Rayleigh-Bénard convection: defect population statistics. *Physica A* 239(1–3):174–88

Ecke RE, Hu Y, Mainieri R, Ahlers G. 1995. Excitation of spirals and chiral symmetry breaking in Rayleigh-Bénard convection. *Science* 269(5231):1704–7

Egolf DA, Melnikov IV, Bodenschatz E. 1998. Importance of local pattern properties in spiral defect chaos. *Phys. Rev. Lett.* 80(15):3228–31

Ercolani NM, Indik R, Newell AC, Passot T. 1999. The geometry of the phase diffusion equation. *J. Nonlinear Sci.* In press

Fantz M, Friedrich R, Bestehorn M, Haken H. 1992. Pattern formation in rotating Bénard convection. *Physica D* 61(1–4):147–54

Fisher ME. 1968. Renormalization of critical exponents by hidden variables. *Phys. Rev.* 176(1):257–72

Frisch U. 1995. *Turbulence.* Cambridge, UK: Cambridge Univ. Press

Fujimura K, Kelly RE. 1993a. Mixed mode convection in an inclined slot. *J. Fluid Mech.* 246:545–68

Fujimura K, Kelly RE. 1993b. Mixed mode convection in an inclined slot containing air. In *Bifurcation Phenomena and Chaos in Thermal Convection*, *ASME HTD*-214, pp. 73–83

Fujimura K, Kelly RE. 1995. Interaction between longitudinal convection rolls and transverse waves in unstably stratified plane Poiseuille flow. *Phys. Fluids* 7(1):68–79

Gershuni GZ, Zhukhovitskii EM. 1969. Stability of plane-parallel convective motion with respect to spatial perturbations. *Prikl. Mat. Mekh.* 33:855–60

Getling AV. 1991. Formation of spatial structures in Rayleigh-Bénard convection. *Usp. Fiz. Nauk* 161(9):1–80

Getling AV. 1998. *Rayleigh-Bénard Convection.* Singapore: World Scientific

Gollub JP. 1994. Spirals and chaos. *Nature* 367:318

Graham A. 1933. Shear patterns in an unstable layer of air. *Philos. Trans. R. Soc. A* 232(714):285–96

Greenside HS, Coughran WM Jr. 1984. Nonlinear pattern formation near the onset of Rayleigh-Bénard convection. *Phys. Rev. A* 30(1):398–428

Haken H. 1978. *Synergetics.* Berlin: Springer

Hart JE. 1971a. Stability of the flow in a differentially heated inclined box. *J. Fluid Mech.* 47:547–76

Hart JE. 1971b. Transition to a wavy vortex regime in convective flow between inclined plates. *J. Fluid Mech.* 48:265–71

Heutmaker MS, Fraenkel PN, Gollub JP. 1985. Convection patterns: time evolution of the wave-vector field. *Phys. Rev. Lett.* 54(13):1369–72

Heutmaker MS, Gollub JP. 1986. Wavenumber distributions and time dependence in Rayleigh-Bénard convection patterns. *Physica D* 23D(1–3):230–34

Heutmaker MS, Gollub JP. 1987. Wave-vector field of convective flow-patterns. *Phys. Rev. A* 35(1):242–60

Hohenberg PC, Swift JB. 1992. Effects of additive noise at the onset of Rayleigh-Bénard convection. *Phys. Rev. A* 46(8):4773–85

Hu Y, Ecke R, Ahlers G. 1993. Convection near threshold for Prandtl numbers near 1. *Phys. Rev. E* 48(6):4399–413

Hu Y, Ecke R, Ahlers G. 1995a. Convection for Prandtl numbers near 1: dynamics of textured patterns. *Phys. Rev. E* 51(4):3263–79

Hu Y, Ecke RE, Ahlers G. 1994. Behavior of focus patterns in low Prandtl number convection. *Phys. Rev. Lett.* 72(14):2191–94

Hu Y, Ecke RE, Ahlers G. 1995b. Time and length scales in rotating Rayleigh-Bénard convection. *Phys. Rev. Lett* 74(25):5040–43

Hu Y, Ecke RE, Ahlers G. 1995c. Transition to spiral-defect chaos in low Prandtl number convection. *Phys. Rev. Lett* 74(3):391–94

Hu Y, Ecke RE, Ahlers G. 1997. Convection under rotation for Prandtl numbers near 1: linear stability, wave-number selection, and pattern dynamics. *Phys. Rev. E* 55(6):6928–49

Hu Y, Pesch W, Ahlers G, Ecke RE. 1998. Convection under rotation for Prandtl numbers near 1: Küppers-Lortz instability. *Phys. Rev. E* 58(5):5821–33

Jeanjean S. 1997. Front propagation of spatio-temporal chaos in Rayleigh-Bénard convection. *Tech. Rep., Cornell Univ. Lab. At. Solid State Phys.*

Kelly RE. 1994. The onset and development of thermal convection in fully developed shear flows. *Adv. Appl. Mech.* 31:35

Kirchartz KR, Oertel H Jr. 1988. Three-dimensional thermal cellular convection in rectangular boxes. *J. Fluid Mech.* 192:249–86

Koschmieder EL. 1974. Bénard convection. In *Adv. Chem. Phys.*, ed. I Prigogine, SA Rice, 26:177–212. Chichester, UK: Wiley-Interscience

Koschmieder EL, Pallas SG. 1974. Heat transfer through a shallow, horizontal convecting fluid layer. *Int. J. Heat Mass Transfer* 17(9):991–1002

Kramer L, Bodenschatz E, Pesch W. 1990. Interaction and dynamics of defects in anisotropic pattern-forming systems. *Phys. Rev. Lett.* 64(21):2588

Kramer L, Pesch W. 1995. Convection instabilities in nematic liquid-crystals. *Annu. Rev. Fluid Mech.* 27:515–41

Küppers G. 1970. The stability of steady finite amplitude convection in a rotating fluid layer. *Phys. Lett. A* 32(1):7–8

Küppers G, Lortz D. 1969. Transition from laminar convection to thermal turbulence in a rotating fluid layer. *J. Fluid Mech.* 35:609–20

Kurzweg UH. 1970. Stability of natural convection within an inclined channel. *Trans. ASME C* 92(1):190–91

Landau LD, Lifshitz EM. 1958. *Statistical Physics.* London: Pergamon. 2nd ed.

Landau LD, Lifshitz EM. 1959. *Fluid Mechanics.* Reading, MA: Addison-Wesley. 2nd ed.

Laveder D, Passot T, Ponty Y, Sulem PL. 1999. Effect of random noise on scaling laws of finite Prandtl number rotating convection near threshold. *Phys. Rev. E* 59:

Li X, Xi HW, Gunton JD. 1998. Nature of roll to spiral-defect-chaos transition. *Phys. Rev. E* 57(2):1705–16

Li XJ, Xi HW, Gunton JD. 1996. Dynamical properties of multiarmed global spirals in

Rayleigh-Bénard convection. *Phys. Rev. E* 54(4):R3105–8

Liu J, Ahlers G. 1996. Spiral-defect chaos in Rayleigh-Bénard convection with small Prandtl numbers. *Phys. Rev. Lett.* 77(15):3126–29

Liu J, Ahlers G. 1997. Rayleigh-Bénard convection in binary-gas mixtures: thermophysical properties and the onset of convection. *Phys. Rev. E* 55(6):6950–68

Manneville P. 1983. A two-dimensional model for three-dimensional convective patterns in wide containers. *J. Phys.* 44(7):759–65

Manneville P. 1990. *Dissipative Structures and Weak Turbulence.* San Diego: Academic

Manneville P, Piquemal JM. 1983. Zigzag instability and axisymmetric rolls in Rayleigh-Bénard convection: the effects of curvature. *Phys. Rev. A* 28(3):1774–90

Meyer CW, Cannell DS, Ahlers G. 1992. Hexagonal and roll flow patterns in temporally modulated Rayleigh-Bénard convection. *Phys. Rev. A* 45(12):8583–604

Meyer CW, Cannell DS, Ahlers G, Swift JB, Hohenberg PC. 1988. Pattern competition in temporally modulated Rayleigh-Bénard convection. *Phys. Rev. Lett.* 61(8):947–50

Millan-Rodriguez J, Bestehorn M, Perez-Garcia C, Friedrich R, Neufeld M et al. 1995. Defect motion in rotating fluids. *Phys. Rev. Lett.* 74(4):530–33

Morris SW, Bodenschatz E, Cannell DS, Ahlers G. 1993. Spiral defect chaos in large aspect ratio Rayleigh-Bénard convection. *Phys. Rev. Lett.* 71(13):2026–29

Morris SW, Bodenschatz E, Cannell DS, Ahlers G. 1996. The spatio-temporal structure of spiral-defect chaos. *Physica D* 97 (1–3):164–79

Neufeld M, Friedrich R. 1994. Model equations for quasi-two-dimensional pattern forming systems. *Ann. Phys.* 19(6):721–33

Neufeld M, Friedrich R, Haken H. 1993. Order parameter equation and model equation for high Prandtl number. Rayleigh-Bénard convection in a rotating large aspect ratio system. *Z. Phys. B* 92(2):243–56

Newell AC, Passot T. 1992. Instabilities of dislocations in fluid patterns. *Phys. Rev. Lett.* 68(12):1846–49

Newell AC, Passot T, Bowman C, Ercolani N, Indib R. 1996. Defects are weak and self-dual solutions of the Cross-Newell phase diffusion equation for natural patterns. *Physica D* 97(1–3):185–205

Newell AC, Passot T, Lega J. 1993. Order parameter equations for patterns. *Annu. Rev. Fluid Mech.* 25:399–453

Newell AC, Passot T, Souli M. 1990. The phase diffusion and mean drift equations for convection at finite Rayleigh numbers in large containers. *J. Fluid Mech.* 220:187–252

Newell AC, Passot T, Souli M. 1991. Focus instability in axisymmetric Rayleigh-Bénard convection. *Eur. J. Mech. B* 10(2):151–57

Newell AC, Whitehead JA. 1969. Finite bandwidth, finite amplitude convection. *J. Fluid Mech.* 38:279–303

Niemela JJ, Donnelly RJ. 1986. Direct transition to turbulence in rotating Bénard convection. *Phys. Rev. Lett.* 57(20):2524–27

Ning L, Ahlers G, Cannell DS. 1990. Wavenumber selection and traveling vortex waves in spatially ramped Taylor-Couette flow. *Phys. Rev. Lett.* 64(11):1235–38

Pampaloni E, Perez-Garcia C, Albavetti L, Ciliberto S. 1992. Transition from hexagons to rolls in convection in fluids under non-Boussinesq conditions. *J. Fluid Mech.* 234:393–416

Perez-Garcia C, Pampaloni E, Ciliberto S. 1990. Finite-size effects in the transition from hexagons to rolls in convective systems. *Europhys. Lett.* 12(1):51–55

Pesch W. 1996. Complex spatiotemporal convection patterns. *Chaos* 6(3):348–57

Pesch W, Kramer L. 1995. General mathematical description of pattern forming instabilities. In *Pattern Formation in Liquid Crystals*, ed. A Buka, L Kramer, pp. 70–90. New York: Springer

Pismen LM, Nepomnyashchy AA. 1993. Structure of dislocations in the hexagonal pattern. *Europhys. Lett.* 24(6):461–65

Plapp BB, Bodenschatz E. 1996. Core dynamics of multi-armed spirals in Rayleigh-Bénard convection. *Phys. Scr.* T67:111–16

Plapp BB, Egolf DA, Bodenschatz E, Pesch W. 1998. Dynamics and selection of giant spirals in Rayleigh-Bénard convection. *Phys. Rev. Lett.* 81(24):5334–37

Plapp BB. 1997. *Spiral-pattern formation in Rayleigh-Bénard convection.* PhD thesis. Cornell Univ., Ithaca, New York

Pocheau A, Daviaud F. 1997. Sensitivity of convective structures to mean flow boundary conditions: a correlation between symmetry and dynamics. *Phys. Rev. E* 55(1): 353–73

Pomeau Y, Manneville P. 1979. Stability and fluctuations of a spatially periodic convective flow. *J. Phys. France Lett.* 40(23): L609–12

Pomeau Y, Zaleski S, Manneville P. 1985. Axisymmetric cellular structures revisited. *Z. Ang. Math. Phys.* 36(3):367–94

Ponty Y, Passot T, Sulem PL. 1997. Pattern dynamics in rotating convection at finite Prandtl number. *Phys. Rev. E* 56(4):4162–78

Quentin G, Rehberg I. 1995. Direct measurement of hydrodynamic fluctuations in a binary mixture. *Phys. Rev. Lett.* 74(9): 1578–81

Rabinovich MI, Tsimring LS. 1994. Dynamics of dislocations in hexagonal patterns. *Phys. Rev. E* 49(1):R35–38

Rasenat S, Steinberg V, Rehberg I. 1990. Experimental studies of defect dynamics and interaction in electrohydrodynamic convection. *Phys. Rev. A* 42(10):5998–6008

Rehberg I, Rasenat S, de la Torre Juarez M, Schöpf W, Hörner F, Ahlers G, Brand MR et al. 1991. Thermally induced hydrodynamic fluctuations below the onset of electroconvection. *Phys. Rev. Lett.* 67(5):596–99

Riecke H, Paap HG. 1987. Perfect wavenumber selection and drifting patterns in ramped Taylor vortex flow. *Phys. Rev. Lett.* 59(22):2570–73

Rogers JL, Schatz MF, Swift JB, Bougie J. 1998. Rayleigh-Bénard experiment under modulated acceleration. *Bull. Am. Phys. Soc. DFD98:BI.03*

Ruth DW. 1980. On the transition to transverse rolls in inclined infinite fluid layers—steady solutions. *Int. J. Heat Mass Transfer* 23(5):733–37

Ruth DW, Raithby GD, Hollands KGT. 1980. On the secondary instability in inclined air layers. *J. Fluid Mech.* 96:481–92

Schlüter A, Lortz D, Busse F. 1965. On the stability of steady finite amplitude convection. *J. Fluid Mech.* 23:129–44

Schmitz R, Zimmermann W. 1996. Spatially periodic modulated Rayleigh-Bénard convection. *Phys. Rev. E* 53(6):5993–6011

Schöpf W, Rehberg I. 1994. The influence of thermal noise on the onset of travelling-wave convection in binary fluid mixtures: an experimental investigation. *J. Fluid Mech.* 271:235–65

Segel LA. 1969. Distant side-walls cause slow amplitude modulation of cellular convection. *J. Fluid Mech.* 38:203–24

Sensoy BA, Greenside HS. 1999. Pattern formation and dynamics of a convecting fluid in an annular domain. *Bull. Am. Phys. Soc. CENT99:QC06.02*

Shadid JN, Goldstein RJ. 1990. Visualization of longitudinal convection roll instabilities in an inclined enclosure heated from below. *J. Fluid Mech.* 215:61–84

Siggia ED, Zippelius A. 1981a. Dynamics of defects in Rayleigh-Bénard convection. *Phys. Rev. A* 24(2):1036–49

Siggia ED, Zippelius A. 1981b. Pattern selection in Rayleigh-Bénard convection near threshold. *Phys. Rev. Lett.* 47(12):835–38

Steinberg V, Ahlers G, Cannell DS. 1985. Pattern formation and wave-number selection by Rayleigh-Bénard convection in a cylindrical container. *Phys. Scr.* T9:97–110

Swift JB, Hohenberg PC. 1977. Hydrodynamic fluctuations at the convective instability. *Phys. Rev. A* 15(1):319–28

Swift JB, Hohenberg PC, Ahlers G. 1991. Stochastic Landau equation with time-dependent drift. *Phys. Rev. A* 43(12):6572–80

Tesauro G, Cross MC. 1986. Climbing of dislocations in nonequilibrium patterns. *Phys. Rev. A* 34(2):1363–79

Tschammer A. 1997. *Nichtlineare Aspekte der Rayleigh-Bénard Konvektion in isotropen und anisotropen Fluiden.* PhD thesis. Univ. Bayreuth, Germany

Tsimring LS. 1995. Penta-hepta defect motion in hexagonal patterns. *Phys. Rev. Lett.* 74(21):4201–4

Tsimring LS. 1996. Dynamics of penta-hepta defects in hexagonal patterns. *Physica D* 89(3–4):368–80

Tu Y, Cross MC. 1992a. Chaotic domain structure in rotating convection. *Phys. Rev. Lett.* 69(17):2215–19

Tu Y, Cross MC. 1992b. Chaotic domain structure in rotating convection. *Phys. Rev. Lett.* 69(17):2515–18

van Beijeren H, Cohen EGD. 1988. The effects of thermal noise in a Rayleigh-Bénard cell near its first convective instability. *J. Stat. Phys.* 53(1–2):77–94

Wiener RJ, Snyder GL, Prange MP, Frediani D, Diaz PR, et al. 1997. Period-doubling cascade to chaotic phase dynamics in Taylor vortex flow with hourglass geometry. *Phys. Rev. E* 55(5):5489–97

Wu M, Ahlers G, Cannell DS. 1995. Thermally induced fluctuations below the onset of Rayleigh-Bénard convection. *Phys. Rev. Lett.* 75(9):1743–46

Xi HW, Gunton JD. 1995. Spatiotemporal chaos in a model of Rayleigh-Bénard convection. *Phys. Rev. E* 52(5):4963–75

Xi HW, Gunton JD, Viñals J. 1993. Spiral defect chaos in a model of Rayleigh-Bénard convection. *Phys. Rev. Lett.* 71(13):2030–33

Xi HW, Viñals J, Gunton JD. 1992. Numerical study of pattern formation following a convective instability in non-Boussinesq fluids. *Phys. Rev. A* 46(8):R4483–86

Zhong F, Ecke R. 1992. Pattern dynamics and heat transfer in rotating Rayleigh-Bénard convection. *Chaos* 2(2):163–71

Zhong F, Ecke R, Steinberg V. 1991. Rotating Rayleigh-Bénard convection: Küppers-Lortz transition. *Physica D* 51(1–3):596–607

Zoldi SM, Liu J, Bajaj KMS, Greenside HS, et al. 1998. Extensive scaling and nonuniformity of the Karhunen-Lòeve decomposition for the spiral-defect chaos state. *Phys. Rev. E* 58(6):R6903–6

Annual Review of Fluid Mechanics
Volume 32, 2000

CONTENTS